8-2010

Observing CO in Circumstellar Disks

Matthew Troutman
Clemson University, mtroutm@clemson.edu

OBSERVING CO IN CIRCUMSTELLAR DISKS

A Dissertation
Presented to
the Graduate School of
Clemson University

In Partial Fulfillment
of the Requirements for the Degree
Doctorate of Philosophy
Physics

---

by
Matthew R. Troutman
May 2010

Accepted by:
Dr. Sean D. Brittain, Committee Chair
Dr. Jeremy King
Dr. Mark D. Leising
Dr. Bradley Meyer

ABSTRACT

This dissertation includes high-resolution, near-infrared spectroscopy to study CO in circumstellar disks around Herbig Ae/Be stars. The velocity-resolved spectra was used to measure the distribution of gas in the circumstellar disk and thus determine the evolutionary state of the system. Near-infrared spectra were obtained on over 30 young circumstellar disks around Herbig Ae/Be stars to study the physical processes in the disk. The radial location of the CO emitting gas bears directly on the evolutionary state of the transition objects in the sample. This study included a detailed study of the debris disk star β Pictoris where the disk mass was estimated. The study found that CO is detected in most disks, yet there were no systems showing evidence for the grain growth scenario of planet formation.

In addition, by using high-resolution spectra of the fundamental ro-vibrational CO emission lines, one can measure the position centroid of the emission as a function of velocity to provide an independent measurement of $M^{1/2}sin(i)$ and the disk inclination. Knowing the inclination is crucial for determining the radial distribution of gas inferred by other high-resolution spectra using low spatial resolution instruments such as the Heterodyne Instrument for the Far Infrared on Herschel. Perhaps most importantly, by measuring the position centroid of the emission, one can determine where in the disk the CO emitting gas arises independent of assumptions about the disk velocity field, Keplerian or otherwise. This analysis was performed on HD 100546, where asymmetric emission is observed. The results also provide a fundamental test of our fluorescence emission model, which allows our model to infer the CO emission radii in systems that are too distant to spatially resolve the emission.

ACKNOWLEDGEMENTS

I would like to first acknowledge my advisor, Dr. Sean Brittain. Thanks in the help over the years to get here. I also wish to acknowledge the other members of my knowledgeable committee: Dr. Jeremy King, Dr. Mark Leising, and Dr. Bradley Meyer. Thanks for the comments, support, and very helpful questions along the way.

I would also like to thank the other faculty members that have helped me through graduate school. I've enjoyed the many conversations and extremely appreciate their support. Thank you also to the other students in our group: Joe Liskowksy and Brian Donehew.

This work was performed under contract with the Jet Propulsion Laboratory (JPL) funded by NASA through the Michelson Fellowship Program. JPL is managed for NASA by the California Institute of Technology.

This dissertation is primarily based on observations obtained at the Gemini Observatory, which is operated by the Association of Universities for Research in Astronomy, Inc., under a cooperative agreement with the NSF on behalf of the Gemini partnership: the National Science Foundation (United States), the Particle Physics and Astronomy Research Council (United Kingdom), the National Research Council (Canada), CONICYT (Chile), the Australian Research Council (Australia), CNPq (Brazil) and CONICET (Argentina).

The NIRSPEC data shown were obtained at the W.M. Keck Observatory, which is operated as a scientific partnership among the California Institute of Technology, the University of California and the National Aeronautics and Space Administration. The Observatory was made possible by the generous financial support of the W.M. Keck Foundation.

The dissertation is also based on observations obtained at the Infrared Telescope Facility, which is operated by the University of Hawaii under Cooperative Agreement no. NCC 5-538 with the National Aeronautics and Space Administration, Science Mission Directorate, Planetary Astronomy Program.

TABLE OF CONTENTS

Table of Contents (Continued)

Page

LIST OF TABLES

LIST OF FIGURES

List of Figures (Continued)

List of Figures (Continued)

CHAPTER 1
INTRODUCTION

To date, more than 450 exoplanets have been discovered, and the number of discovered exoplanets grows nearly every day. The planets that have been discovered exist around a wide range of stellar mass; planets have been discovered around low-mass brown dwarfs (Todorov et al., 2010) and up to high-mass A stars (Cameron et al., 2010).

Recently, a planet was discovered around the nearby A star β Pictoris (β Pic; Lagrange et al., 2009). The system also shows evidence of a disk, most prominently seen in imaging at 1.25 μm (Mouillet et al., 1997). At 12 Myr, it is representative of a young system just after the process of planet formation, in contrast to most of the discovered planets existing in much older systems.

Despite the large number of discovered planets, the physics of planet formation is not well understood. Some constraints are known, such as the disk dissipation timescale, which places an upper limit on the time a planet has to form. This is known by determining the fraction of stars that show evidence for disks at different ages. Disks are inferred from their spectral energy distribution (SED). An excess of emission at infrared wavelengths compared to the stellar continuum is attributed to emission from a disk. The disk frequency has been measured in a number of systems as a function of time. By 3 - 5 Myr the disk fraction drops to about 50%, suggesting that the inner disk being traced by the near-infrared excess is dissipated on this timescale. This is shown in Figure 1.1, presenting data from Wyatt (2008) and Hernández et al. (2007) to illustrate that excesses are extremely common for young stars ($\sim$85% at $<$1 Myr), while for older stars it is much less common ($\sim$0% at $>$10 Myr). If the inner disk material is removed by $\sim$ 10 Myr, then this places an upper limit on the planet formation timescale.

In addition to the disk fraction dissipating over $\sim$10 Myr, observations of the accretion rate point to the same timescale of disk evolution. The accretion rate is a measure of material moving from the disk onto the central star; thus, the accretion is halted when the

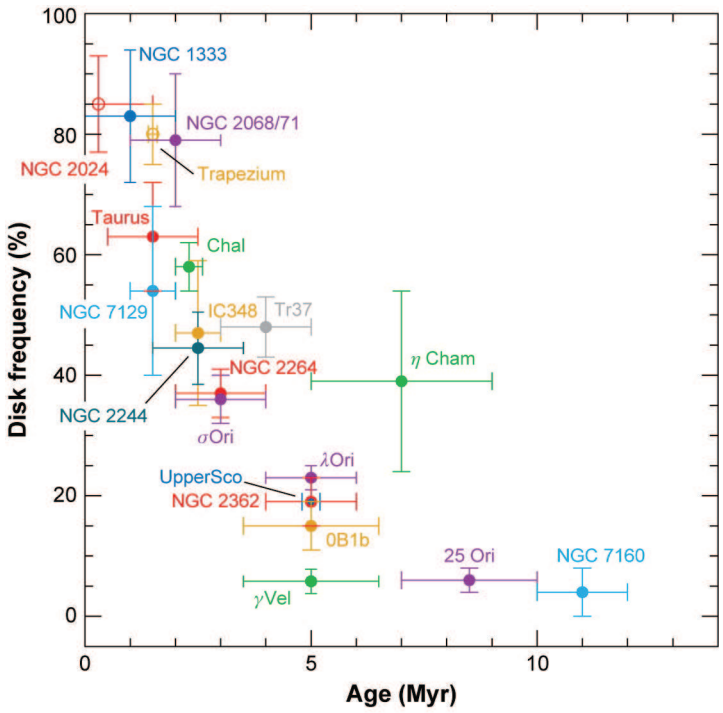

Wyatt MC. 2008.
Annu. Rev. Astron. Astrophys. 46:339–83

Figure 1.1 Figure from Wyatt (2008), with data from Hernández et al. (2007). Shows the disk fraction for solar-like stars in star forming regions or moving groups detected from near-infrared excess. Most stellar groups have high disk fractions (near 85%) at young ages, which drops to nearly 0% at ∼10 Myr. As the near-infrared excess traces the inner disk, the observations suggest that the inner disk dissipates on a timescale of <10 Myr.

inner disk is depleted. Observations of nearby star-forming regions show that the accretion rate of stars in these systems drops below detection limits at 10 Myr (Sicilia-Aguilar et al., 2005). While the accretion rate is difficult to measure, both the accretion rate and the disk fraction point to a disk lifetime of ∼10 Myr.

While the disk dissipation timescale places a constraint on the timescale for planet formation, it is not known how quickly planets form. The dissipation of the disk may be due to planets forming, but may also represent other mechanisms (e.g. photoevaporation; §**??**).

Additionally, the order of planet assembly it is unclear. Depending on the process of planet formation, large-mass planets may form first or they may form contemporaneously with lower-mass planets. A theory of planet formation must be able to reproduce our Solar System where the larger planets exist at ∼5 AU, but also must reproduce observations of the "hot Jupiters" that exist at ∼0.05 AU. Planet migration may be able to explain the latter (Armitage, 2007), but the planets must form early to be able to migrate inward from the presence of a disk.

There are two main theories of planet formation. The first is the theory of hierarchical building of planets, typically called the core accretion theory (Perri & Cameron, 1974; Mizuno et al., 1978). In this scenario, small grains collide with small grains, creating larger grains. Larger grains then accrete other grains, eventually building up a large core massive enough to gravitationally collect gas. The planet sweeps up the residual gas in the disk as the planet's mass grows. This scenario is attractive due to its simplicity, yet has problems. First, the process takes a long time (∼10 Myr). The depletion of gas in this scenario occurs at late times, and is strikingly close to the observed disk lifetimes (Haisch et al., 2001). Thus, it would not explain systems where the disk is dissipated earlier than 10 Myr.

The other scenario is the disk instability model (Boss, 1997). In this model, the disk becomes gravitationally unstable. Once the mass of the disk is large enough, generally ∼0.1 M_{star}, then the disk begins to fragment. In these fragments, giant gas planets can form very quickly (e.g. Mayer et al., 2007). However, this scenario produces inconsistent abundances in the planets in our solar system from what is observed (Saumon et al., 1995; Young, 2003). A comparison of these two models is presented in Matsuo et al. (2007).

Another unknown is the efficiency of planet formation, or how likely a system is to form a planet. A number of disk factors contribute, including the order of planet assembly, which may effect the efficiency for other planets to form. For example, a giant planet forming first and migrating through the disk may reduce the possibility for a Earth-sized planet to survive in the system (Armitage, 2003).

While much can be learned from observing the dust (e.g. the disk fraction from near-infrared excess), 99% of the mass in the disk is gas. Additionally, some scenarios that suggest planet formation also suggest other scenarios not involving a planet when observing

the dust alone (see §1.2.2). However, observing the gas distribution can distinguish between these scenarios. Additionally, the gas is also important to circularizing the gas. Indeed, only a small amount of gas is necessary to circularize the gas (<1 $M_\oplus$). Thus, determining how long gas remains in a system is important to determine if planets can exist at late times.

1.1 Observing the Gas

Observations of atomic species in circumstellar disks are limited to electronic transitions in the UV, forbidden transitions in the optical, and 21 cm observations of hydrogen. One good example of studying atomic species in circumstellar disks is from the study of β Pictoris (Brandeker et al., 2004). This study takes advantage of the close proximity of the system (19 pc), and the fact that the disk is edge-on. Brandeker et al. (2004) observe emission from Fe I, Na I, Ca II, Ni I, Ni II, Ti I, Ti II, Cr I and Cr II, and attempt to determine the spatial structure of the disk. Despite the fact that β Pictoris is a debris disk (dusty remnants of circumstellar disk evolution), they find that the distribution (both vertically and radially) follows closely the predictions of disk models for debris disks (e.g. Kamp et al., 2007).

A number of forbidden line transitions in the optical have been observed in young stars (Hamann, 1994). However, one particular study of note is the forbidden [O I]6300Å line observation in a number of circumstellar disks (Acke et al., 2005). They show from line profiles that the emission is likely from a flared disk, where a shadowed disk is much less likely to show emission. This is evidence that the emission is from a thin, upper layer of the circumstellar disk.

The forbidden lines probe regions where the conditions allow for the transition - at lower densities or with intense radiation. Thus, these observations are not a useful probe of gas for every part of the circumstellar disk.

Most of the mass in the disk is in hydrogen. In disks, the H_2/H ratio can be as large as $\sim 10^6$, so most of the disk mass is in molecular hydrogen (Kamp et al., 2007). Electronic transitions of UV can probe the inner regions of disks, where temperatures are high enough

to excite the H_2 electronically (Ingleby et al., 2009). However, in some cases it is unclear whether the H_2 is from the warm skin of a disk or an outflow (Herczeg et al., 2006).

H_2 has no permanent dipole, so rotational transitions in the infrared are extremely weak. UV radiation from the central star fluoresces the H_2 in the upper layers of the disk to produce emission from ro-vibrational transitions in the sources that have been observed (e.g. Bary et al., 2003). The amount of material that is probed is very small since the transition probabilities are so weak. In one study, only 6 of 29 T Tauri stars were found to show rotational emission from H_2, and in those sources only $\sim$1 $M_\oplus$ was observed (Bitner et al., 2008). Because detecting H_2 in the disk is difficult (Carmona et al., 2008), it is not an ideal tracer of gas in the disk.

Other molecular species present their own difficulties. For example, some of the most abundant molecules in the disk - CO, H_2O - are also abundant in Earth's atmosphere. Thus, observations of these species in the infrared where strong transitions occur, have to take advantage of doppler shifts that move the observed wavelengths of the transitions out of telluric features. Other abundant molecules, like the symmetric molecules of CH_4 and C_2H_2 are similar to H_2 in that they have no permanent dipole moment and have weaker transitions in the infrared.

The Spitzer Space Telescope has provided an extremely unique view of molecular species in circumstellar disks (see for one example; Lahuis et al., 2007). Being a space-based telescope, observing molecules that would normally be unobservable because of telluric features becomes possible. For example, understanding the distribution of H_2O and OH can provide information on the snow line and chemistry in the inner regions of circumstellar disks (Salyk et al., 2008).

1.1.1 CO as a Tracer

The next most abundant molecule to H_2 is CO. CO is a more sensitive probe of warm gas because the molecule has a permanent dipole, allowing ro-vibrational transitions. The oscillator strengths of these transitions are a 10^6 times larger than those for H_2, despite the fact that the abundance of CO in a disk is 10^4 times lower (van Dishoeck, 1986). Thus, the overall strength of the emission from CO is 100 times larger.

Additionally, CO has frequently been detected in circumstellar disks (Najita et al., 2000, 2003, 2007; Brittain et al., 2003, 2007a, 2009; Blake & Boogert, 2004; Rettig et al., 2004, 2006; Salyk et al., 2009). The distribution of gas in the disk can be inferred through high-resolution spectra of CO. Most directly, the maximum velocity in the features is related to the inner extent of the gas (assuming Keplerian motion, the stellar mass, and the inclination of the disk). Additionally, if the gas is excited by UV fluorescence, the vibrational temperature of the gas depends on the distance from the star (Krotkov et al., 1980). Fluorescence occurs when the CO molecule is electronically excited, the molecule relaxes to the ground electronic state in excited vibrational levels. Transitions from these levels result in ro-vibrational CO emission lines (Brittain et al., 2007a). These transitions are observed in the near-infrared. Infrared observations can detect a small amount of CO (<1 $M_{\oplus}$). This is below the threshold necessary to circularize the orbits of terrestrial planets.

1.2 Disks Around Herbig Ae/Be Stars

The focus of this dissertation will be Herbig Ae/Be stars (HAeBe). These stars are 2 to 10 $M_{\odot}$ that are spectral type A or B with emission lines, have an infrared excess coming from circumstellar dust, and are of luminosity class III - IV (Waters & Waelkens, 1998). HAeBe stars are identified as intermediate-mass analogs to T Tauri stars (Herbig, 1960; Finkenzeller & Mundt, 1984; Herbig & Bell, 1988; Walker & Wolstencroft, 1988; van den Ancker et al., 1998; Vieira et al., 2003). Because they are higher mass than T Tauri stars, the dynamic timescales are shorter.

HAeBes have a strong UV continuum, thus they can efficiently excite CO at large distances from the star. Further, they do not have photospheric absorption CO features, so the circumstellar lines do not need to be disentangled from photospheric features. Thus, the study of warm molecular gas in the disk is more straightforward than in disks around T Tauri stars (especially transition disks around late type stars). Further, there is evidence of giant planets around A stars; thus we focus on the study of gas in disks around HAeBes.

There are some important distinctions between the disks around HAeBe and T Tauri stars. First, the disks around HAeBe stars are thought to be more massive than the disk

around T Tauri stars (Herbig, 1960; Strom et al., 1972). Second, the disks around HAeBe stars are thought to evolve on faster dynamical timescales (Wisniewski et al., 2007).

1.2.1 Debris Disks

Debris disks are dusty remnants of circumstellar disks. The material is reprocessed dust and gas from collisions that is similar to the Zodiacal dust in our Solar System. The disks are usually less massive than circumstellar disks with a near-infrared excess, yet are usually higher mass than our own Solar System's Kuiper belt. Ages for debris disks are typically <100 Myr, though ages at early evolution can be difficult to determine (Zuckerman & Song, 2004a; Moór et al., 2006).

Typically these disks are thought to contain dusty material that is either remnant primordial or reprocessed dust from larger grains colliding together. This could be from a ring of smaller bodies colliding, larger planets migrating to change orbital resonances, or some other similar process. Models of the steady-state evolution, where dust is being processed in planetesimal belts, reproduce the observations of debris disks around early type stars.

From observations of excesses at infrared wavelengths (24 and 70 μm) around a large sample of A stars, it is seen that excesses at 24 μm dissipate with a characteristic timescale of 150 Myr, while excesses at 70 μm do not follow that same timescale (Rieke et al., 2005; Su et al., 2006; Wyatt et al., 2007). This can be explained with steady-state evolution, where the inner regions probed at 24 μm evolves on a faster timescale than the outer disk.

Additionally, there may be evidence for delayed evolution of these systems. From 24 μm excesses of A stars in different star-forming regions, there seems to be an increase in excess at an age of 10-15 Myr, which seems to be suggestive of self-stirring (Currie et al., 2008). Stirring in the disk could be from migrating planets, or from a grain destruction event. This may be a radial evolution of material in the disk, as the physical processes of collisions and planet migrations change over time.

1.2.2 Transitional Disks

Transitional disks are defined by an optically thick outer disk, typically probed by longer wavelength emission, while having an optically thin inner disks, probed by a lack of near-infrared excess in their SED. Though called transitional, they do not necessarily represent a stage between a full, optically thick disk and a non-existent or optically thin disk. Frequently, the lack of emission from the inner regions of the disk are claimed to come from an embedded companion, such as a planet. Despite the intriguing possibility often claimed that these are the result of a planet sculpting out a region within the disk, there are other possible scenarios that can give rise to a transitional SED. Indeed, one of the recent transitional disks, CoKu Tau 4, was found to have a binary companion and not a planetary companion (Ireland & Kraus, 2008).

There are four scenarios that can give rise to a transitional SED, explained by Najita et al. (2007). The scenarios are a small (< 5 M_J) companion, a large (< 5 $M_{Jupiter}$) companion, photoevaporation, and grain growth (Figure 1.2). These scenarios can be distinguished by observing the gas in the disk, but all produce identical SEDs and would be classified as transitional. The specific observational differences among these scenarios will be discussed in Chapter 3.

1.3 Summary

This dissertation will focus on the following questions: what is important in the excitation of CO? In order to study the gas and find expectations for detections, the important excitation mechanisms must be understood. How does the gas dissipate relative to the dust in a disk and how long does the gas remain in the system? And finally, what signatures of a planet can be found in the disk?

Chapter 2 will focus on the analysis of β Pictoris, a debris disk star that shows unique CO excitation. Chapter 3 presents a survey of Herbig Ae/Be stars, which are young, intermediate-mass stars ($\sim$2 - 10 $M_\odot$). We use this survey to understand the role various heating processes play in exciting the CO in a circumstellar disk. Chapter 4 describes the technique of spectro-astrometry, and the application to a specific source. This technique is a way of determining the distribution of gas on very small spatial scales ($\sim$1 AU at 100 pc).

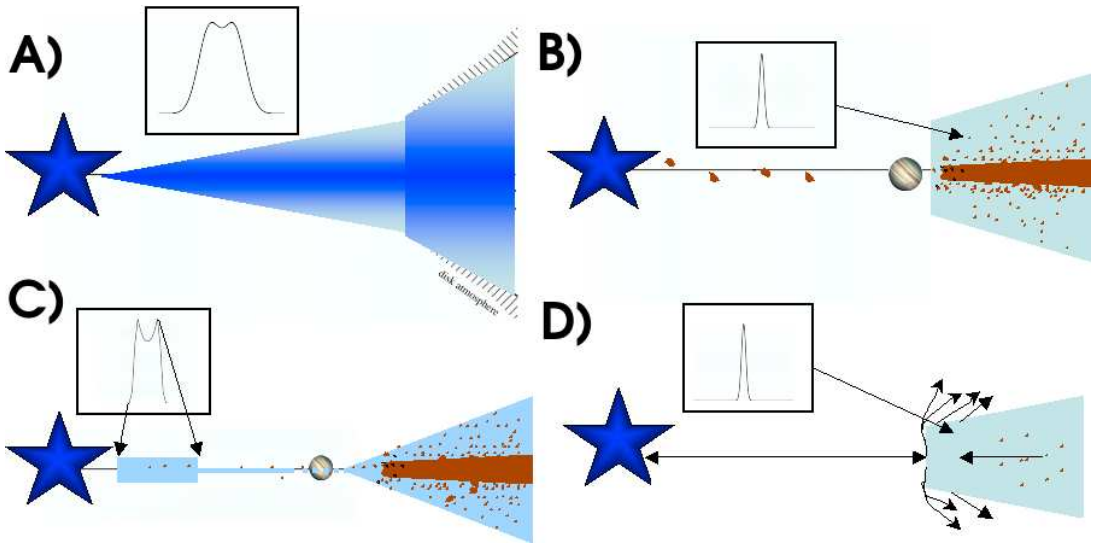

Figure 1.2 The different processes that may explain a transitional disk. The different panels represent grain growth (A), photoevaporation (B), a smaller-mass companion (<5 M_J; C), and a large companion (>5 M_J; D)

Finally, Chapter 5 will briefly summarize the results of this dissertation and explore future extensions of these studies.

1.3.1 Collisional Excitation

In systems like circumstellar disks, one of the dominant excitation mechanisms is collisions between CO and other species. In a high density medium, a thermal population described by the Boltzmann distribution determines the relative populations in each level. However, in lower densities, other excitation mechanisms occur that can cause the level populations to differ from a Boltzmann distribution. For example, collisions between CO and another species can determine the rotational populations of CO. A specific case of this will be studied in Chapter 2, where β Pictoris shows evidence for a sub-thermalized CO rotational population. Because of this, the colliding species and density of the species with which the CO is colliding can be determined. These results are in preparation for publication (Troutman et al., 2010a). Another example is from Gibb et al. (2010), where the

populations are thermalized, but the critical density of the surrounding material (hydrogen) can be determined since the temperature of the system is known.

1.3.2 Spectral Synthesis

To gain an understanding of planet formation, observations of CO ro-vibrational transitions will be used to probe the inner regions of the disk. These observations can determine the distribution of gas in the disk. To determine the distribution, a spectral synthesis model will be used which has been successful in previous studies of HAeBe disks (Brittain et al., 2007a, 2009). Determining the distribution is key to understanding the morphology of the disk, specifically noted earlier when discussing transitional disks. This research will complement observations from Spitzer in determining the transitional disks that may have planets creating the observed SEDs.

With this in mind, a large survey over a number of Herbig Ae/Be stars observing near-infrared CO was carried out. The goal is to understand better the excitation mechanisms in the disk. The other chapters in this dissertation explore some of the specific, interesting cases observed in this survey. However, Chapter 3 will focus on the overall picture of planet formation and disk excitation. These results will also be written for publication (Troutman et al., 2010c).

1.3.3 Spectro-astrometry

Spectro-astrometry is a relatively new technique, specifically in the study of circumstellar disks. It takes advantage of spatially extended emission beyond a stellar PSF. After subtracting the stellar PSF from each each spectral bin of a CCD, any extended emission will be present. Spectro-astrometry has been used in the past to detect binary companions (e.g. Baines et al., 2004) as well as outflows (such as jets; e.g. Whelan et al., 2004).

Spectro-astrometry is the process by which the centroid of each velocity bin is measured, providing high spatial resolution of the distribution of gas in the disk. As the gas in the disk rotates on a Keplerian orbit, the projected line-of-sight velocity changes throughout the disk (see Figure 1.3). This produces the well-known double-peaked emission feature,

a telltale sign of differential rotation (Figure 1.3, right panel). If emission of gas in a circumstellar disk extends for ∼100 AU, then at 100 pc, the disk appears to extend over 1.0″. This is large enough to leave an observable signature on the spectrogram (see Figure 1.4). By measuring the center-of-light in each velocity bin, the spatial offset can be determined, thus producing a spectro-astrometric signal.

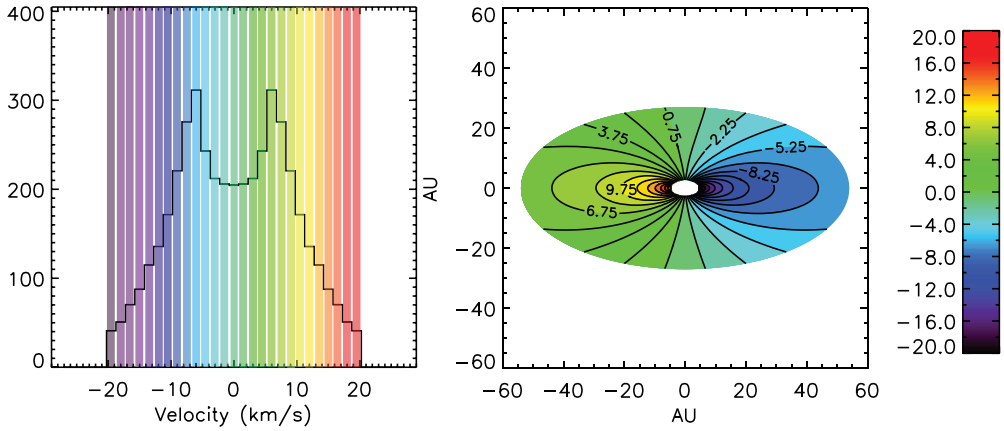

Figure 1.3 Model of a circumstellar disk and the resulting emission line flux. The right panel shows velocity contours from a disk, as it would appear on the sky. The disk is at an inclination of 50°, and the central star is 3 times the mass of the Sun. The left panel shows the velocity profile of an emission line from the disk, with the same colors as the velocity contours. The flux from a disk falls off as 1/r.

By using high-resolution spectra of the fundamental ro-vibrational CO emission lines, one can measure the position centroid of the emission as a function of velocity to provide an independent measurement of $M^{1/2}\sin(i)$. For a given inclination, we can place a dynamical constraint on the mass of the central star. If the CO emission has a simple geometry, such as an azimuthally symmetric inclined ring, we will be able to constrain the inclination directly by observing the emission at multiple positions angles. This provides a check on the disk inclination inferred from measurements of the outer disk. Knowing the inclination is crucial for determining the radial distribution of gas inferred by other high-resolution spectra using low spatial resolution instruments such as the Heterodyne Instrument for the Far Infrared on the Herschel Space Telescope.

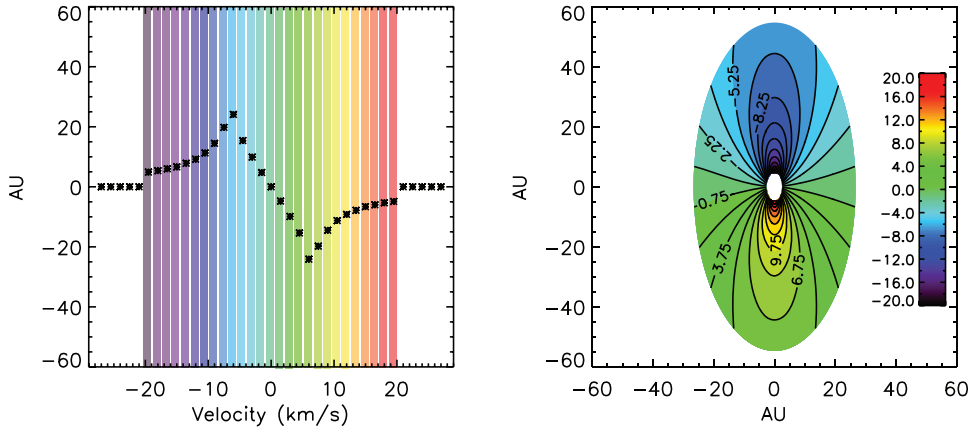

Figure 1.4 Model of a circumstellar disk and the resulting spectro-astrometric signal. The right panel shows velocity contours from a disk, as it would appear on the sky. The disk is at an inclination of 50°, and the central star is 3 times the mass of the Sun. The left panel shows the spectro-astrometric signal of an emission line from the disk, with the same colors as the velocity contours. The flux from a disk falls off as ∼1/r.

Spectro-astrometry was first used to study circumstellar disks by (Acke & van den Ancker, 2006a) to observe the [O I] 6300Å forbidden line. After subtracting the stellar PSF, the "center-of-light" for each spectral pixel was found. For an emission line coming from a rotating circumstellar disk, the spatial extent of each bin gives an idea of the radial location of the gas. Acke & van den Ancker (2006a) observed both HD 100546 and HD 97048, both of which will be discussed later. Using the technique, they were able to determine the position angle of the semi-major axis of the disks, as well as determining the inner radius of the [O I] gas in both systems. In the case of HD 100546, Acke & van den Ancker (2006a) find the inner radius of the [O I] is 10 AU and supports the hypothesis that the inner edge is being sculpted by a planetary companion. Specifically, they estimate a planet mass of 20 M_J at 6.5 AU.

The process of spectro-astrometry was shortly followed up with CO in circumstellar disks (Pontoppidan et al., 2008; van der Plas et al., 2009; Brittain et al., 2009). See Figure 1.5 for the specific case of HD 100546. In the case of van der Plas et al. (2009), both

HD 100546 and HD 97048 were studied. Direct comparison with this study will be presented in Chapter 4.

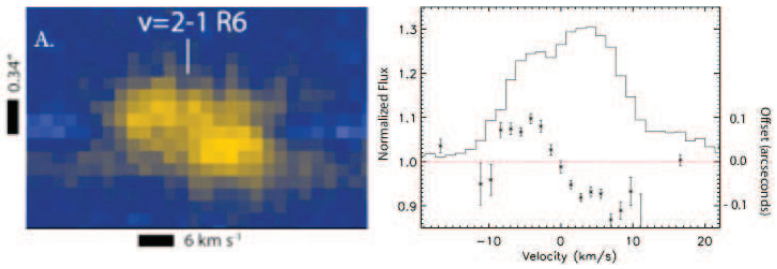

Figure 1.5 Spectrum of the v=2-1 R(6) CO line presented in Brittain et al. (2009). In the left panel is the continuum-subtracted spectrogram of the line. The vertical direction of the plot is the spatial dimension (0.085″ per pixel) and the horizontal direction is the spectral dimension (1.5 km s^{-1} per pixel). The resolution of each axis is denoted by the black rectangles. In the right panel is the 1-d spatial cut of the line plotted in velocity space (the scale of normalized flux is marked on the left side of the plot). The excess on the red-side is due to blending with ^{13}CO emission. The spatial offset of each velocity channel from the centroid of the continuum PSF (dominated by the star) is over-plotted and the scale is labeled on the right side of the plot.

Perhaps most importantly, by measuring the position centroid of the emission, we can determine where in the disk the CO emitting gas arises independent of assumptions about the disk velocity field, Keplerian or otherwise. The radial location of the CO emitting gas bear directly on the evolutionary state of the disks in the sample. The results also provide a fundamental test of the fluorescence emission model previously discussed, which allows the model to characterize the CO emission radii in systems that are too distant to spatially resolve the emission. In Chapter 4, I will discuss the analysis and specifics of this technique using the spectro-astrometery.

CHAPTER 2

CO EXCITATION ANALYSIS

2.1 Collisional Excitation in Disks

To determine the level populations of CO, in principle, every excitation and de-excitation mechanism should be accounted for. However, in practice, often there are many of those mechanisms that can be ignored. For example, in circumstellar disks, collisions between species dominate the excitation and de-excitation between rotational levels of CO in high density. In low density, radiation from the cosmic microwave background can play a part in the rotational levels. UV radiation from the central star can dominate the excitation of the vibrational levels. These show that for any level populations that are of interest, there may be different excitation mechanisms that are important for different densities. In this section, the specific mechanism of collisional excitation will be discussed. This is when collisions between CO and another species are dominant.

In circumstellar disks and some diffuse clouds, for example, collisional excitation is important. If the collisional partner with CO and its density are known, then the populations can be determined. More interestingly, if a CO spectrum is observed and a collisional partner can be assumed, then the density of the collisional partner can either be directly determined or a lower limit can be placed. An example of this used CO absorption to determine that the density of hydrogen, the collisional partner in this case, is more consistent with a dense cloud rather than a diffuse medium (Gibb et al., 2010). The codes discussed in the Appendix were used in this specific study.

2.1.1 LTE/NLTE

An extra constraint can come in if the level populations of CO do not reflect thermal equilibrium. In the case where collisions are dominant, if the density is below the critical density to thermalize CO, then the density can be determined directly. When this happens, the higher rotational levels of CO are populated at a lower rate than would be expected using a simple Boltzmann distribution. This also produces an higher population in the

levels just below the sub-thermal levels, which can be easily detected. The simplest way to check this is by plotting an excitation diagram using the column density of each of the observed features. The log of the column densities, when plotted against J"(J"+1), would be linear if the levels are thermalized. A sub-thermal population because of a low density of the collision partner, will produce level column densities lower than the linear fit. A specific case of this will be shown in Section 2.2.

2.1.2 Collision Partners and Rates

The determination of the density of the collision partner is only as good as the collision rates. The lack of collision rates and dearth of recent data are perhaps surprising. The most reliable rates for collisions with CO are from Green & Thaddeus (1976), and are given for H, H_2, and He. The rates are determined from 5 K to 100 K, and are typically good to within 30%. Unfortunately, rates for other species are rare, and in some cases like H_2O, extrapolated from other species (N_2 in the case of H_2O Green, 1993). Thus, it is only in particular cases where using collisional excitation can be done; fortunately, regions where hydrogen are abundant are common.

Perhaps most disturbingly, more recent studies that attempt to generalize collision rates to a simple relation good for a wide range of temperatures do not reflect the collision rates determined in laboratory measurements. It is difficult to determine the validity of such studies, but a simple check on the rates is to use the collision rates at a very high density to determine if the thermal populations are retrieved. If not, then the collision rates may be in question. In the case of Warin et al. (1996), we do not re-acquire the thermal population at high densities.

2.2 The Study of β Pictoris

β Pictoris (β Pic) is a 12 Myr (Zuckerman et al., 2001), A5V star at a distance of 19.3 pc (Crifo et al., 1997) with an edge-on debris disk. The dust component of the disk has been studied extensively from the optical through the sub-millimeter (Smith & Terrile, 1984; Artymowicz et al., 1989; Golimowski et al., 1993; Kalas & Jewitt, 1995; Mouillet et al., 1997; Pantin et al., 1997; Holland et al., 1998; Heap et al., 2000; Liseau et al., 2003; Okamoto et al.,

2004; Golimowski et al., 2006; Boccaletti et al., 2009). Asymmetries in the dust distribution, and in particular warps in the disk (e.g. Kalas & Jewitt, 1995; Mouillet et al., 1997; Heap et al., 2000), point to the presence of a planet in the disk which was recently imaged (Lagrange et al., 2009).

In addition to the dust, the disk has a reservoir of atomic gas with at least two components (e.g. Ferlet et al., 1987; Jolly et al., 1998; Roberge et al., 2000; Brandeker et al., 2004). One component shows lines red-shifted relative to the rest frame of β Pic, resulting from infalling gas released from star-grazing planetesimals (e.g., Vidal-Madjar et al., 1994). A second component (comprised of Na I, Fe I, Ca II, Ti II, Ni I, Ni II, Cr II) remains at rest relative to the star and has a spatial distribution similar to that of the dust (Ferlet et al., 1987; Olofsson et al., 2001; Brandeker et al., 2004). The existence of the stable gas in a debris disk was somewhat surprising because radiation pressure from β Pic to should be sufficient to radially accelerate the gas to high velocities ($\gtrsim$ 100 km s^{-1}; Brandeker et al., 2004). Thus, some braking mechanism is necessary to explain the stable component of the gas. Brandeker et al. (2004) suggested hydrogen gas may serve as the braking agent, and find that $\sim$50 $M_\oplus$ of material is needed. However, Freudling et al. (1995) show from limits on 21 cm emission that the atomic hydrogen mass must be less than 1.6 $M_\oplus$. As for the molecular gas, Lecavelier des Etangs et al. (2001) place a tight constraint on the mass of H_2 at $<$0.1 $M_\oplus$ based on the non-detection of absorption lines from electronic transitions. Additionally, Chen et al. (2007) use the absence of H_2 emission in Spitzer IRS spectra to limit the amount of warm H_2 (50 - 100 K) in the disk at $<$17 $M_\oplus$, ruling out a more extended reservoir of molecular gas. Thébault & Augereau (2005) use dynamical arguments to argue that the total gas mass must be $<$0.4 $M_\oplus$. From these observational constraints, it would appear that the disk is not massive enough to brake the gas.

However, Fernández et al. (2006) note that a much smaller mass of hydrogen may be sufficient to brake the gas because only the ionized component needs to be decelerated. This is because the elements that receive the highest radiative force are also the elements with the highest ionization rates, thus only the ions are important. The acceleration of the neutrals is negligible, thus they do not need braking. Fernández et al. (2006) explore possibilities

for braking the ions in the gas, which would explain the observed stable component of the gas.

The first possibility is ionized particle collisions, where the ions lose momentum by Coulomb interactions. The ions are dynamically coupled, so the radiative force on the particles can be described by an average over all of the particles. Some ions feel a low radiative force, so if these atoms were somehow overabundant, the average radiative force on the ions would go down - effectively slowing the gas. Carbon is one such atom that feels a low radiative force. Indeed, an increase in the carbon abundance by a factor of $\sim$10 with respect to other atoms may be sufficient to lower the average radiative force on the ions, braking the gas. Atomic carbon is observed to be enhanced compared to oxygen in the β Pic system by a factor of 18, relative to solar (Roberge et al., 2006).

Another possibility for braking the gas is ion collisions with neutral gas. In this scenario, a total disk mass of at least 0.1 $M_{\oplus}$ is required (Fernández et al., 2006), well within all of the observational limits mentioned above. This is much smaller than the value inferred by Brandeker et al. (2004), as they did not assume only the ionized particles need to be slowed. While the ion-ion collision scenario is possible, limits on the disk mass cannot rule out a contribution to the stabilization of the atomic gas from ion-neutral collisions as well.

To explore the role ion-neutral collisions play in braking the gas in the outer disk around β Pic, we present near infrared high resolution spectra of β Pic centered near 4.7 μm. We detect fundamental ro-vibrational CO lines in absorption and place strict constraints on fluorescent emission from higher vibrational bands. We find that the rotational levels are only thermalized up to J$''$=2 and describe how this information provides a means to calculate the density of gas in the disk. We also use the non-detection of fluoresced ro-vibrational CO emission to constrain the inward extent of CO in the disk.

2.2.1 Observations

We acquired high-resolution near-infrared spectra of β Pic using PHOENIX (Hinkle et al., 2003, 2000, 1998) at the Gemini South telescope and CSHELL (Tokunaga et al., 1990) at the NASA Infrared Telescope Facility. The resolutions of PHOENIX and CSHELL are

R=50,000 and R$\sim$40,000, respectively. The PHOENIX observations were taken on March 23, 2008 and January 12, 2003. The CSHELL observations were taken on August 8, 2000. The observations were centered around 4.7 μm to cover fundamental ro-vibrational transitions of CO. A summary of observations, presented in Table 4.1, includes the lines that are observed.

Table 2.1 Log of β Pic Observations

Date	Instrument	Spectral Range (cm^{-1})	Integration Time (m)	S/N	Lines covered
2008 Mar 23	PHOENIX	2104 - 2113	16	90	v=1-0: P(8), P(9), v=2-1: P(1), P(2), P(3)
2003 Jan 12	PHOENIX	2150 - 2160	8	125	v=1-0: R(1), R(2), R(3)
2000 Aug 8	CSHELL	2146 - 2152	16	100	v=1-0: R(0), R(1)

Observations in the 4.7 μm region are dominated by a strong thermal background, limiting the exposure times. Therefore, short exposures are taken while nodding between two positions separated by $\sim 5''$. The exposures are taken in an ABBA pattern in order to cancel the thermal continuum to first order. The scans are flat fielded, cleaned of hot and dead pixels, including cosmic ray hits, and then combined in the sequence (A_1-B_1-B_2+A_2)/2. Because the spectra are curved along the detector, they are first rectified by finding the centroid of each column and shifted to a common row. A one-dimensional spectrum is then extracted from the rectified spectrum. This spectrum is combined with an atmospheric transmittance model spectrum in order to find a wavelength solution. The model is created using the Spectral Synthesis Program (Kunde & Maguire, 1974), which accesses the 2000HITRAN molecular database (Rothman et al., 2003). Each spectrum is then ratioed to a standard star observed at a similar airmass to remove telluric absorption lines. Areas where the transmittance is below 50% are omitted.

2.2.2 Results

We detect the R(0), R(1), and R(2) fundamental ro-vibrational CO absorption lines near 4.64 μm (Figure 2.1). The R(1) and R(2) lines are unresolved at the the 6 km s^{-1} resolution of PHOENIX, which is consistent with the intrinsic line width b=1.3 km s^{-1} inferred from the electronic absorption measurements observed in the UV (Roberge et al., 2000). Similarly, the R(0) line observed with CSHELL was unresolved at the effective $\sim$8 km s^{-1} resolution of the instrument. The R(1) was not detected with CSHELL as the CO line was not cleanly separated from the heavily saturated telluric component. The N_2O line on the red wing of the telluric feature lowers the transmittance of the atmosphere an additional 20%. The heliocentric Doppler shift of the CO absorption lines for all dates are $+21 \pm 1$ km s^{-1}, consistent with the heliocentric Doppler shift of β Pic, and indicates that it is part of the stable component of the gas disk (Ferlet et al., 1987; Jolly et al., 1998; Roberge et al., 2000; Brandeker et al., 2004; Roberge et al., 2006; Roberge & Weinberger, 2008).

Figure 2.2 shows the spectrum in the 4.74 μm region containing the v=1-0 P(8) and P(9) lines and the v=2-1 P(1), P(2), and P(3) lines. These features are not detected.

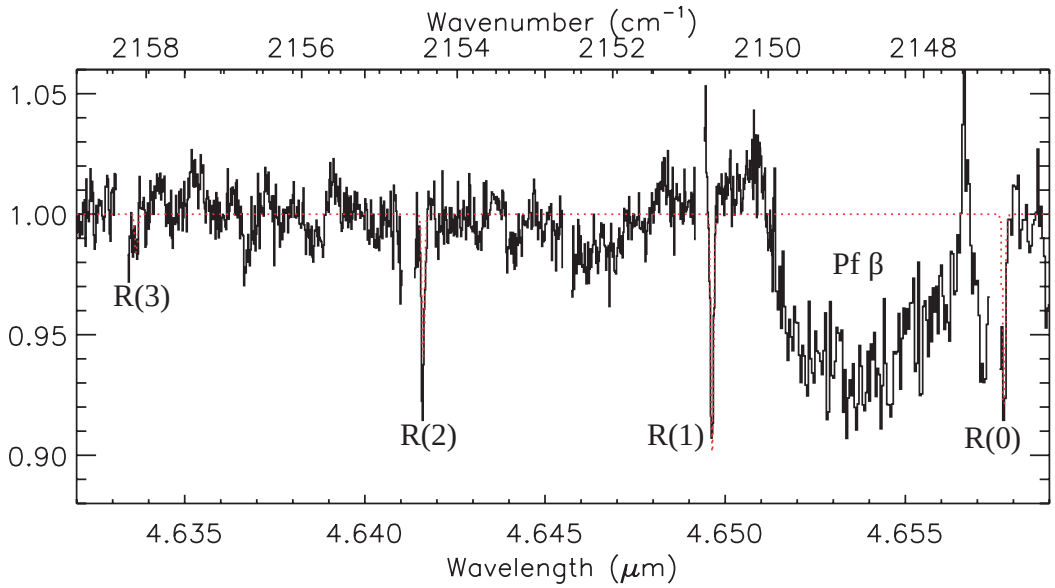

Figure 2.1 Spectrum of CHSELL (> 4.651 μm) and PHOENIX (< 4.651 μm). The concatenation of the data from Phoenix and CSHELL reveals the R(0), R(1), and R(2) ro-vibrational CO absorption lines. The R(3) ro-vibrational CO absorption line is not observed. The broad feature centered at 4.654 μm is the hydrogen line Pf β. The spectrum has been modeled by calculating the excitation of the rotational levels in the ground vibrational state (see Section 2.2.3.3). The resultant absorption spectrum is plotted over the data (red dotted line).

While the gas in the disk around β Pic is too cold to give rise to collisionally excited CO ro-vibrational emission or absorption, CO ro-vibrational emission can be excited by UV fluorescence (Krotkov et al., 1980). When CO is excited electronically and relaxes back to the ground electronic state, the excited vibrational bands are populated. Thus, even relatively cool gas can give rise to a large vibrational temperature. For example, the CO around HD 141569 has a rotational temperature of 200 K while the vibrational temperature is ∼5000 K (Brittain et al., 2003, 2007a). CO was first detected around β Pic in the UV via electronic absorption lines. Thus, one may expect to observe cold ro-vibrational emission from β Pic. We do not detect this emission in our spectrum around 4.74 μm, with a signal-to-noise ratio of 90. Assuming the lines are Gaussian and unresolved, our one-sigma upper limit on the equivalent width is $\sim 5 \times 10^{-4}$ cm^{-1}. Scaling the equivalent width by the flux

density as measured by the Infrared Space Observatory ($F_{4.7\mu m} = 1 \times 10^{-9}$ ergs s^{-1} cm^{-2} μm^{-1}), the upper limit on the flux of the individual lines is 7.1×10^{-16} ergs cm^{-2} s^{-1} (Table 2.2).

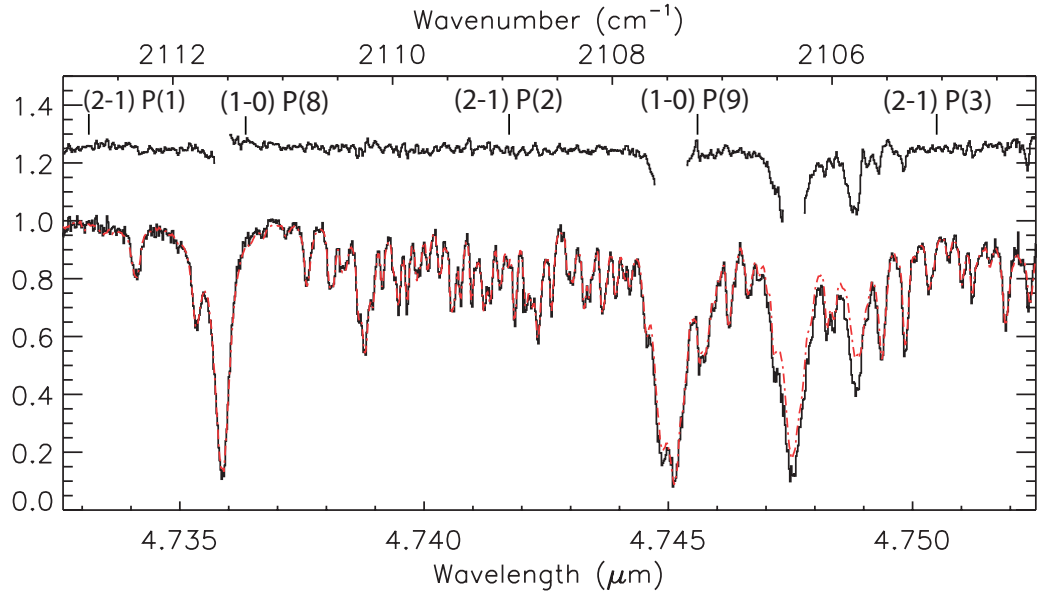

Figure 2.2 The spectrum of β Pic. The spectrum β Pic (solid line) and the telluric standard, HR 5671 (dot-dashed line), have been normalized and overplotted. The ratio of the spectra is also plotted and offset by 0.25 units. Areas where the transmittance is less than 50% are omitted. The locations of the CO transitions are shown for v=1-0 and v=2-1. No emission is observed, including the v=2-1 P(1) line at ~ 4.733 μm.

Table 2.2 Line Fluxes

Line	$\tilde{\nu}_{rest}$ (cm^{-1})	$\tilde{\nu}_{obs}$ (cm^{-1})	V_{rad} (km s^{-1})	Equivalent Width ($\times 10^{-3}$ cm^{-1})	N(CO) ($\times 10^{14}$ cm^{-2})	Flux (ergs cm^{-2} s^{-1})
v=1-0 R(0)	2147.08	2146.95	18	4.9 ± 0.8	4.3	$\cdots$
v=1-0 R(1)	2150.86	2150.71	21	6.0 ± 0.5	9.0	$\cdots$
v=1-0 R(2)	2154.59	2154.43	22	4.4 ± 0.5	7.2	$\cdots$
v=1-0 R(3)	2158.30	2158.14	22	$< 0.5 \pm 0.5$	< 2.3	$\cdots$
v=2-1 P(1)	2112.98	$\cdots$	$\cdots$	< 0.5	$\cdots$	$< 7.1 \times 10^{-16}$
v=2-1 P(2)	2109.14	$\cdots$	$\cdots$	< 0.5	$\cdots$	$< 7.1 \times 10^{-16}$
v=2-1 P(3)	2105.26	$\cdots$	$\cdots$	< 0.5	$\cdots$	$< 7.1 \times 10^{-16}$

2.2.3 Analysis

2.2.3.1 Constraint on CO Distribution

The absorption of UV flux by CO through the fourth positive system leads to the population of excited vibrational levels in the ground electronic state (e.g. Krotkov et al., 1980). For example, Brittain et al. (2003) observe ro-vibrational CO emission from the disk around HD 141569 distributed from the inner 50 AU and conclude that the vibrational temperature of the gas is ∼5500 K while the rotational temperature of the gas is ∼200 K. This situation occurs when the vibrational population of cool gas is dominated by the de-excitation of electronically excited molecules. In this "strong pumping limit," the vibrational population of CO near the star reflects the color temperature of the star's ultraviolet field (Krotkov et al., 1980). Further from the star, the spontaneous de-excitation of the vibrational levels becomes more significant relative to the rate at which these levels are populated by the relaxation of electronically excited molecules and the vibrational temperature decreases.

We use the non-detection of the CO emission in the disk to constrain the distribution of CO. Using the upper limits on the v=2-1 emission features (displayed in Figure 2.2) and the analysis in the previous section, the fluxes of the P(1), P(2) and P(3) lines are $< 7.1 \times 10^{-16}$ erg cm^{-2} s^{-1}. To place limits on the inner radius of the CO annulus, we will compare an observational limit on the number of CO emitting molecules to the disk profile used above.

Jolly et al. (1998) and Roberge et al. (2000) observe the CO absorption lines from the fourth positive system. When these molecules relax, they will populate v≥1. We have calculated the population of v=2 for CO as a function of distance from the star following the procedure described by Brittain et al. (2009). We take our input UV spectrum for β Pic taken from Kurucz atmospheric models (Kurucz, 1993), which are then scaled to the emission presented in Jolly et al. (1998). The UV flux is initially absorbed over an annulus extending from an inner radius, r_{in} = 13 AU, to 323 AU, following the same profile described in Section 2.2.3.3 (Equation 2.8; Brandeker et al., 2004). The UV flux is propagates through each gas annulus, where the flux is attenuated by the distance from the host star as it travels through the annulus. In this case, n_0 is normalized to reproduce a

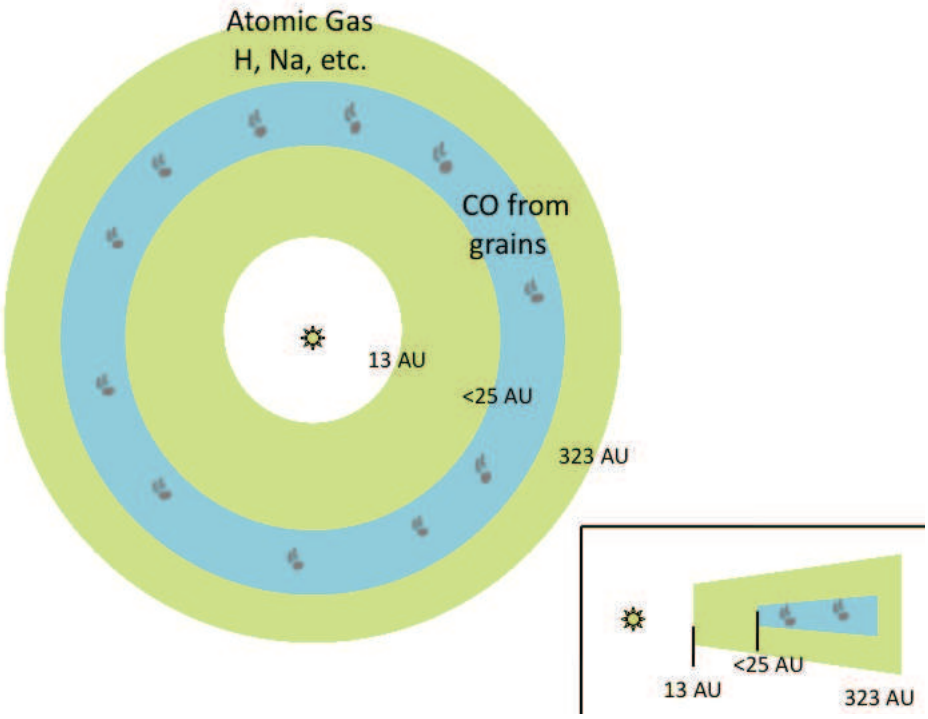

Figure 2.3 Diagram illustrating the distribution of CO relative to other gas in the β Pic system. The observed CO is coming off of grains from R>25 AU, and then colliding with hydrogen in the atomic gas disk.

column density of 2.1×10^{15} cm^{-2}. We require an inner radius $r_{in} \geq 25$ AU for the disk to intercept a small enough fraction of the stellar flux that the emergent UV fluorescent flux is below the observational limits. There is no constraint on the outer radius. Figure 2.3 shows our picture of the disk.

2.2.3.2 Ro-vibrational Absorption

We use the equivalent width of the absorption features to determine the rotational temperature. The column density of molecules in each state is related to the equivalent width of absorption by:

$$N_{J''} = \frac{W_{\tilde{\nu}}}{8.85 \times 10^{-13} f_{J'J''}} \tag{2.1}$$

where J″ is the lower transition state, $W_{\tilde{\nu}}$ is the equivalent width of the line, 8.85×10^{-13} cm is the classical electron radius ($\pi e^2/m_e c^2$), and $f_{J'J''}$ is the oscillator strength of the transition. The equivalent widths and column densities are presented in Table 2.2. If the gas is in local thermodynamic equilibrium, then the relative population of each label is given by the Boltzmann distribution,

$$N_{J''} = \frac{N_{tot}(2J''+1)}{Q} e^{-hcBJ''(J''+1)/kT}, \tag{2.2}$$

where Q is the rotational partition function, and B is the rotational constant. This can be rewritten as:

$$\frac{k}{hcB} ln\left(\frac{N_{J''}}{2J''+1}\right) = -\frac{1}{T}J''(J''+1) + \frac{k}{hcB} ln\left(\frac{N_T}{Q}\right), \tag{2.3}$$

where N_T is the total number of CO absorbing molecules. Thus, we plot $(k/hcB)\ ln(N_{J''}/2J''+1)$ vs J″(J″+1) so that the negative reciprocal of the slope is equal to the rotational temperature (Figure 2.4). The rotational temperature is 15 ± 2 K, which is consistent with the temperature inferred from observations of the electronic absorption spectrum. This fit indicates that the $J'' = 3$ is sub-thermally populated. This can occur when the gas density is too low for collisions to balance spontaneous emission. Thus, we can calculate the density of the gas for a given set of collisional partners.

The column density of CO is determined from the addition of all of the observed levels and found to be $N(CO) = (2.1 \pm 0.3) \times 10^{15}$ cm^{-2}. Jolly et al. (1998) used electronic absorption spectra of CO from the Goddard High-Resolution Spectrograph (∼1500Å) to measure the column density and temperature of CO and found $N(CO) = (2 \pm 1) \times 10^{15}$ cm^{-2} and T=20±5 K. Roberge et al. (2000) used the Space Telescope Imaging Spectrograph (STIS) to find a CO column density of $N(CO) = (6.3 \pm 0.3) \times 10^{14}$ cm^{-2} at a temperature of 15.8 ± 0.6 K. Our column density is consistent with that of Jolly et al. (1998), and a factor of ∼3 larger than that reported by Roberge et al. (2000), while the temperature we derive is consistent with both studies. As both Jolly et al. (1998) and Roberge et al. (2000) are measuring absorption of the same electronic transitions, these two UV studies should be tracing the same column of gas. Further, the ro-vibrational absorption we observe should be probing the column of gas observed against the continuum of the star, so it is unclear why

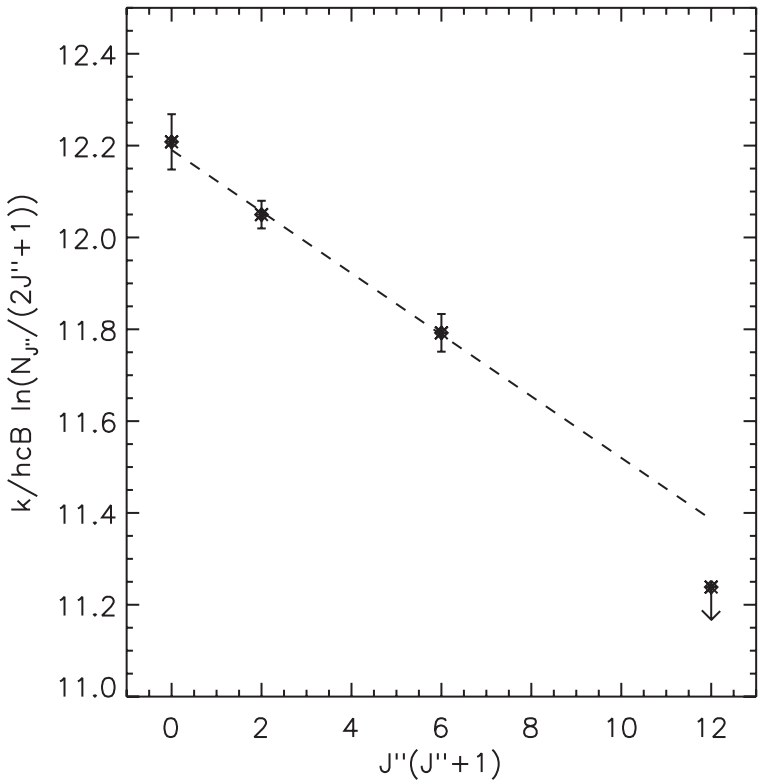

Figure 2.4 CO excitation plot of the low-J ro-vibrational absorption lines. The dashed line represents a temperature of 15 ± 2 K. The R(3) feature is an upper limit, and much lower than the LTE fit to the lower J lines, suggesting that $J'' = 3$ is sub-thermally populated. The sub-thermal population allows the calculation of the density of the collision partner.

the column density observed on these three epochs is so different. One possibility is that the absorption is variable on the 3 year timescale between the UV observations on November 1994 (Jolly et al., 1998), and December 1997 (Roberge et al., 2000). However, we do not see this degree of variability between August 2000 and January 2003. If the column of CO changed by a factor of three during this time, we would not find the rotational temperature diagram linear. Indeed, a change in the column density by a factor of three between the 2000 and 2003 observations would cause the $J'' = 0$ point to be offset by ~ 0.4 units relative to the other data points in our excitation diagram (Figure 2.4). Another explanation may be that the UV observations of the $J'' < 3$ lines are saturated, providing an underestimate to the total column density. Roberge et al. (2000) assumed the rotational levels were in LTE; however, our results indicate that this is not the case (see Figure 2.4). If the lowest three lines were slightly saturated ($\tau_0 \gtrsim 1$), then it is possible that the total column of CO could be significantly underestimated by fitting to sub-thermally populated, optically thin lines. To determine if the assumption of NLTE can reproduce the observed equivalent widths, we calculate the rotational levels explicitly in the next section.

2.2.3.3 Excitation

The population of the rotational levels of CO are calculated explicitly under the assumption that the molecules are excited by a combination of collisional excitation and radiative pumping by the cosmic microwave background, and that the level populations are in steady state. The lifetime of CO in the disk is ~200 years (Roberge et al., 2000), so we assume that the creation and destruction of CO in the disk is unimportant. To highlight the role these various processes play in determining the populations of each rotational level, we consider the state J=1,

$$\begin{aligned} \frac{dn_{J=1}}{dt} &= +B_{01}\mathcal{J}_{01}n_0 - (A_{10} + B_{10}\mathcal{J}_{10})n_1 \\ &\quad - \sum_{i=0, i\neq 1}^{7} k_{1i}n_1 + (A_{21} + B_{21}\mathcal{J}_{21})n_2 \\ &\quad + \sum_{m=0, m\neq 1}^{6} k_{m1}n_m = 0, \end{aligned} \tag{2.4}$$

where B_{ij} is the Einstein coefficient, $\mathcal{J}_{ij}$ is the energy density of the cosmic microwave background at the frequency of the transition, and k_{ij} is the collisional (de)excitation coefficient from the ith state to the jth state, and n_i is the fractional population of the i^{th} level. The collisional coefficients are given by

$$k_{ij} = \sum n_s f_s(T), \tag{2.5}$$

for an up transition ($i < j$), and

$$k_{ji} = \frac{2J' + 1}{2J'' + 1} e^{-hc\tilde{\nu}/kT} \sum n_s f_s(T) \tag{2.6}$$

for a down transition ($i > j$).

The variable n_s is the number density of the collision partner, J$''$ is the lower state, J$'$ is the upper state, and $f_s(T)$ is the collision rate for a specific species, s. A suite of synthetic spectra were created with the number density of the collision partner as a free parameter. We assume an intrinsic line broadening of 1.3 km s^{-1} (Roberge et al., 2000). The equivalent widths of the features from the synthetic spectrum are compared to the observed equivalent widths. We determine the best fit to the density by calculating chi-squared for each density of a given collision partner.

The CO in the disk is likely being photodesorbed from icy grains. This is a process by which the molecules in the ice lattice are electronically excited. This energy breaks the bonds of the lattice allowing the moleucles to escape. The photodesorption efficiency of CO is similar to the photodesorption efficiency of H_2O (Öberg et al., 2009a,b). The mixing ratio for H_2O/CO can range from as low as theoretical values of 1 (D'Hendecourt et al., 1985) to as high as $\sim$50 as observed in Oort cloud comets (Disanti & Mumma, 2008). Thus it is plausible that H_2O could be the dominant collision partner with CO. The collision rate between H_2O and CO has been estimated by Green (1993) to be 1.04×10^{-11} cm^3 s^{-1} at 15 K for the transition between the ground and first excited rotational level. Adopting these parameters, we find that the best fitting H_2O density is $n_{H_2O} = (3.0^{+1.5}_{-1.0}) \times 10^3$ cm^{-3}, found from the minimization of the chi-squared values comparing the equivalent widths of the model to the data. Figure 2.5 shows the chi-squared values assuming 15 K for different densities of H_2O. The chi-squared contours are given from (Wall & Jenkins, 2003). The

specific implementation of these codes is described in Appendix 6. If we assume that the column density of H_2O is 1-50 times the column density of CO, and the CO and H_2O are co-spatial in an annulus, then the path length of the water annulus would be:

$$L_{annulus} = \frac{N(H_2O)}{n_{H_2O}}, \tag{2.7}$$

where $N(H_2O)$ is the column density of H_2O and n_{H_2O} is the density. The path length of the annulus will range from 4.7×10^{-2} AU to a maximum of 2.3 AU, which seems implausibly small. The desorption efficiency depends on the intensity of the incident UV, and the disk is optically thin to UV photons. The UV flux will fall of as r^{-2} in the radial direction, therefore it seems unlikely that the desorption would decrease so sharply at a distance of 25 AU from the star, restricting the gas to such a small annulus. Thus, we conclude that it is unlikely that H_2O is the dominant collision partner. Other species, such as CH_4, may also come off grains and collisionally excite CO, as the photodesorption efficiencies are similar to CO and H_2O (Öberg et al., 2009a,b). Collision rates between these species and CO have not been measured, though if we assume that collision rates for species like CH_4 behave similarly to non-polar molecules such as N_2 (for which rates do exist), we conclude that it is unlikely that other such molecules serve as the dominant collision partner.

Another possibility is that at an age of of 12 Myr, β Pic retains some primordial hydrogen. Thus the CO could be photodesorbed from icy grains and collisionally excited by hydrogen gas in the disk. While H I has not been observed, the upper limits do not rule out the possibility that the hydrogen abundance reflects a solar composition (Brandeker et al., 2004). Indeed, Brandeker et al. (2004) use a photoionization code to infer the radial profile of hydrogen in the gas disk based on their measurement of the distribution of Na I:

$$\begin{aligned} n_H(r,z) &= n_0 \left[\left(\frac{r}{117 \text{ AU}} \right)^{2.4} + \left(\frac{r}{117 \text{ AU}} \right)^{5.3} \right]^{-1/2} \\ &\quad \times \exp\left(-\frac{z^2}{(0.17r)^2} \right), \end{aligned} \tag{2.8}$$

where the metals are observed to extend from 13 AU to 323 AU. Assuming the disk reflects a solar composition, they find the mass of the disk is $\sim$0.1 $M_\oplus$. This is below the detection limits of the mass determined from 21 cm observations of the disk (Freudling et al., 1995).

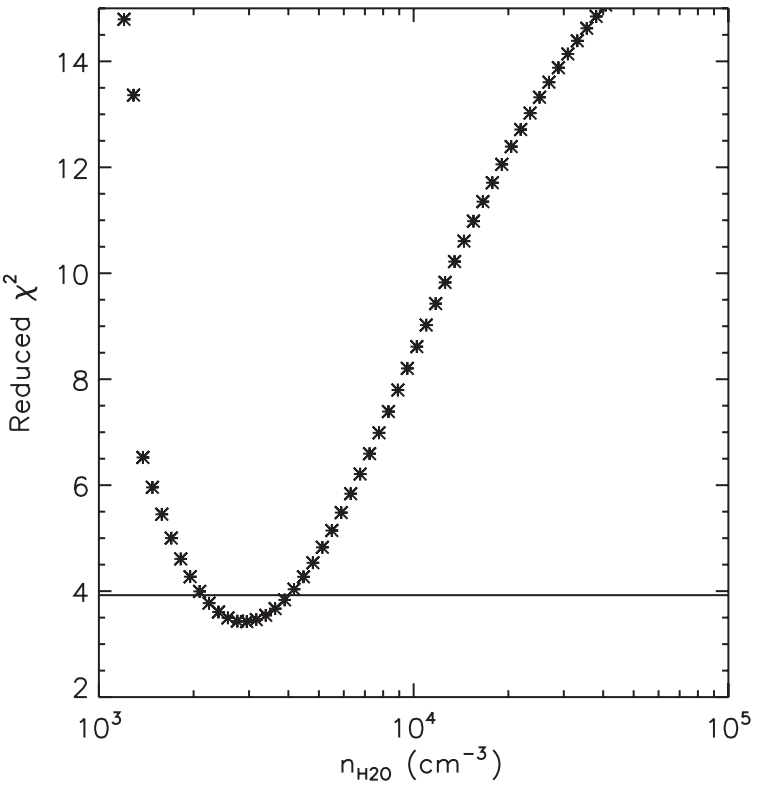

Figure 2.5 A one-dimensional chi-squared plot for the fitting of the equivalent widths using H_2O as the collision partner. Chi-squared versus n_{H_2O}. For each value of n_{H_2O}, we calculated the rotational population of CO and the resultant equivalent widths of the v=0-1 R(0), R(1), R(2), and R(3) lines. The reduced chi-square statistic for each run of our model is plotted, and the 68% confidence level corresponding to our 1σ uncertainty is plotted as a solid line. We find that $n_{H_2O} = 3.0 \times 10^3 cm^{-3}$ provides the best fit to the data.

We determine the density of H I necessary to collisionally excite the observed rotational levels of CO.

To calculate the density of H I necessary to generate the observed rotational population of CO, we adopt the collision rates between hydrogen and CO from Green & Thaddeus (1976) and calculate the population of the rotational levels of CO using equation 2.4. We vary the density of the hydrogren from 10^4 cm^{-3} to 10^7 cm^{-3} with 100 evenly-spaced points in log space. For each density we calculate the population of the levels. These numbers are compared to the measured levels and the reduced chi-square is calculated (Figure 2.6). We find the best-fitting density is $n_H = (2.5^{+7.1}_{-1.2}) \times 10^5$ cm^{-3}. Figure 2.7 shows the comparison of different hydrogen densities. Thus, assuming the levels are not in LTE sufficiently can describe the observations, possibly resolving the discrepancy between the observed column densities.

2.2.3.4 Constraint on Disk Column Density and Mass

We assume the density of hydrogen we determined is the fiducial density at the mid-plane (z=0), and the hydrogen continues inward beyond the CO to where the atomic gas originates (13 AU). If the hydrogen follows the density profile described using the distribution given by Brandeker et al. (2004, Equation 2.8) for other metals in the disk, then the fiducial density scaled to 117 AU becomes $n_0=(3.9^{+11}_{-1.8})\times10^4$ cm^{-3}. We can calculate the column density of atomic hydrogen by integrating through the disk and compare to observational limits. The line-of-sight hydrogen column density becomes:

$$\begin{aligned} N(H) &= \int_{13}^{323} n_0 \left[\left(\frac{r}{117 \text{ AU}} \right)^{2.4} + \left(\frac{r}{117 \text{ AU}} \right)^{5.3} \right]^{-1/2} dr \\ &= (2.1^{+5.9}_{-1.0}) \times 10^{20} \text{ cm}^{-2}. \end{aligned} \tag{2.9}$$

Integrating the distribution over the disk from 13 AU to 323 AU, we find that the total gas mass is:

$$\begin{aligned} \text{H atoms} &= 2\pi \int_{13}^{323} \int_{-\infty}^{\infty} n_H(r,z) r \, dr dz \\ &= (6.2^{+17}_{-2.9}) \times 10^{50} \text{ atoms} \\ &= (0.17^{+0.47}_{-0.08}) \text{ M}_\oplus. \end{aligned} \tag{2.10}$$

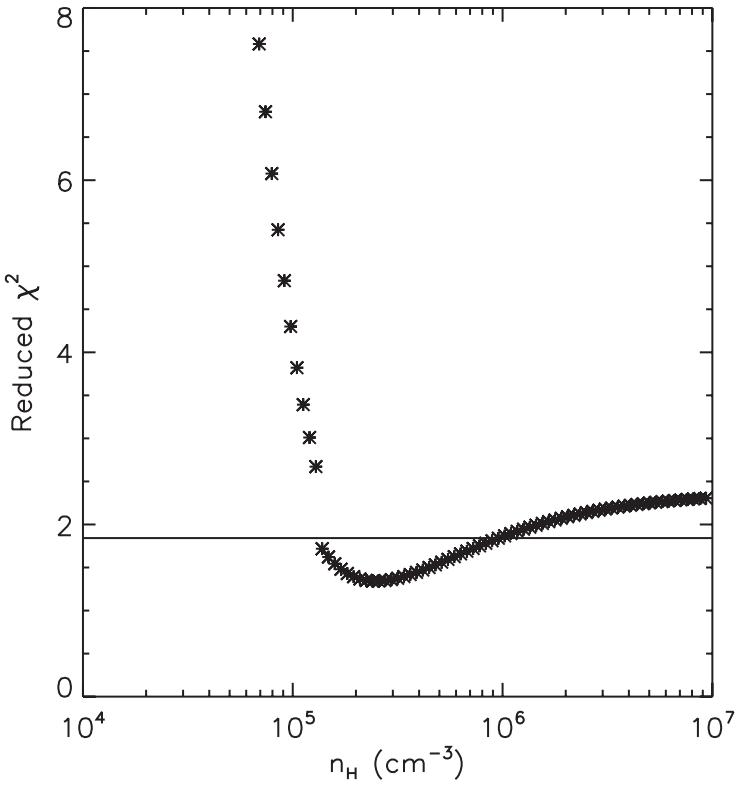

Figure 2.6 Chi-squared versus n_H. For each value of n_H, we calculated the rotational population of CO and the resultant equivalent widths of the v=0-1 R(0), R(1), R(2), and R(3) lines. The reduced chi-square statistic for each run of our model is plotted, and the 68% confidence level corresponding to our 1σ uncertainty is plotted as a solid line. We find that $n_H = 2.5 \times 10^5 cm^{-3}$ provides the best fit to the data.

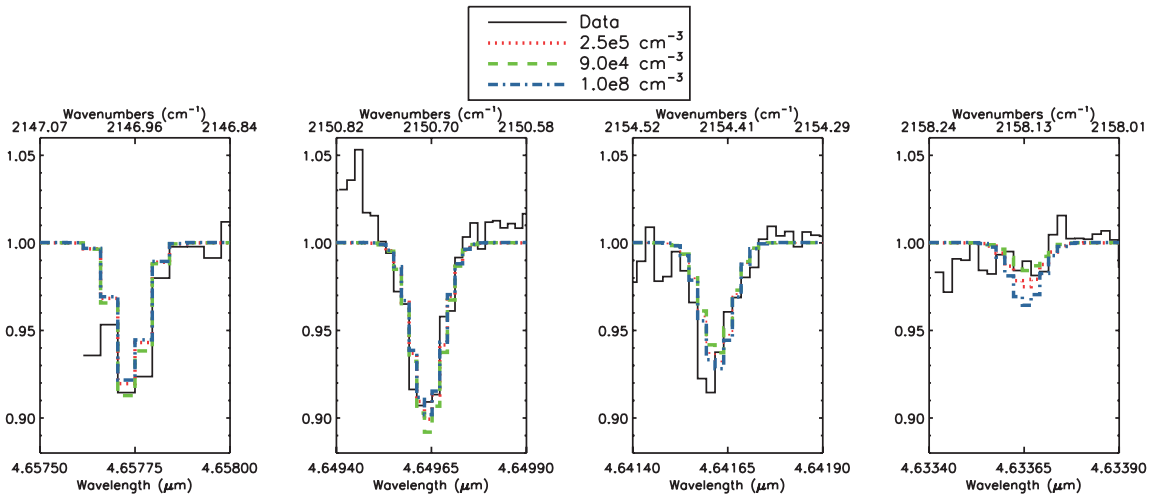

Figure 2.7 Absorption features with models overplotted. The data is represented with a solid line, while all of the colored lines represent the model for different temperature and density combinations. Plotted is the best-fitting value of 15 K and n_H=2.5×10^5 cm^{-3}, as well as comparison from a low density of n_H=0.9×10^5 cm^{-3} and the thermalized case at a very high density. The low density is shown to fit well to the sub-thermal R(3) feature, but over-predicts the R(1) feature while under-predicting the R(2) feature. The high density case is used to emphasize the sub-thermal population of the R(3) feature.

The mass is within the limits from 21 cm observations (1.6 $M_\oplus$; Freudling et al., 1995), but also within limits from dynamical arguments (0.4 $M_\oplus$ Thébault & Augereau, 2005). The determined mass is also close to the mass inferred by Brandeker et al. (2004) from fitting the distribution of the sodium emission line profile in a solar-composition disk (∼0.1 $M_\oplus$). Brandeker et al. (2004) also fit a profile assuming the metals were more depleted in the disk, finding a disk mass of ∼40 $M_\oplus$. As we find a disk mass that is close to (in the lower limit) or higher than the disk mass found in the solar case, the disk appears to have a solar composition or is very slightly metal depleted.

2.2.4 Discussion

We observe absorption of CO that is sub-thermally populated in the disk around β Pic. We attempted to use H_2O as the collision partner for the CO, representing the possibility that the CO is coming from planetesimals. However, we found that a molecule

with a cross section similar to that of H_2O would require a high density and concomitantly an extremely narrow annulus of absorbing gas. Since the disk is optically thin and CO photodesorption scales with the UV flux, it is unlikely that the CO and H_2O originate from a narrow annulus. We determine that a small amount of primordial hydrogen is a more plausible collision partner. The determined density implies a column density and mass of N(H)=$(2.1^{+5.9}_{-1.0})\times10^{20}$ cm^{-2} and M_H=$(0.17^{+0.47}_{-0.08})$ $M_\oplus$, respectively. These are consistent with the non-detection of hydrogen with 21cm observations and upper limits on gas in the disk (Freudling et al., 1995), as well as even tighter constraints based on dynamical arguments (0.4 $M_\oplus$; Thébault & Augereau, 2005). This scenario requires that the CO and hydrogen are well mixed in the region where the CO is coming off the grains. The mass determined is just at the 0.1 $M_\oplus$ required for ion-neutral collisions with hydrogen to explain the braking of the gas. Thus, it seems that while the excess carbon abundance is consistent with ion-ion collisions to be the breaking mechanism of the gas, the mass of the hydrogen is itself enough to brake the gas through ion-neutral collisions. The fact that the β Pic disk is so long-lived is not surprising given the fact that there is enough mass to brake the gas.

We speculate that the metals and CO observed in the disk around β Pic are released from grains into a remaining reservoir of hydrogen gas. It is difficult to understand the origin of the enhanced carbon abundance measured by Roberge et al. (2006). One possibility is the material subliming off of the planetesimals is carbon rich (for example CH_4/CO$\sim$10) and most of the oxygen is tied up in water, which has a much higher sublimation temperature (170 K versus 30 K). If most of the oxygen is tied up in water and the carbon is mostly in reduced species like CH_4, it is possible that the carbon comes primarily from subliming planetesimals at the inner edge of the disk, while the other metals come from desorption of grains throughout the disk. Grains will have organic species rich in carbon that may desorb at the same rate as CO (Öberg et al., 2009a,b). While the amount of the molecular material is not enough to be a primary collision partner to explain the populations of CO, there will be enough to dissociate and produce an overall carbon-rich disk.

The result presented here, especially the prediction for the mass of hydrogen, can be tested with more sensitive measurements of hydrogen. Deeper observations than Freudling et al. (1995) are necessary to test these predictions (an order of magnitude improvement would be

sufficient to explore the estimated mass, while a factor of $\sim$50 improvement could rule out the lower limit to 3σ). The Square-Kilometer Aarray, estimated to be 50-100 times more sensitive than current radio telescopes (Carilli & Rawlings, 2004; Dewdney et al., 2009), should be able to test these predictions.

CHAPTER 3

HERBIG AE/BE SURVEY

Circumstellar disks are believed to be the birthplace of planets. Recently, a companion was directly imaged around β Pictoris (Lagrange et al., 2009), consistent with previous indirect evidence at the existence of an embedded companion (Heap et al., 2000). Followup observations did not confirm the planet, though it is possible that the planet was behind the star. Future observations should confirm the existence of a massive companion. Similarly, the presence of planets have been inferred from disk observations in a few systems: Vega (Wilner et al., 2002) and HD 100546 (Bouwman et al., 2003). Thus, the study of disks bears directly on the processes of planet formation.

Disks appear to evolve from the inside out. A small fraction appear to have inner holes as evidenced by their SED, referred to as transitional disks Strom et al. (1990). Because their numbers are small, it appears that this is a short phase of disk evolution. However, it may be that not all disks go through this phase. Also it isn't clear if it is always a consequence of star formation.

Transitional disks are described by SEDs with excess at long wavelengths, yet a lack of excess at near-infrared wavelengths (Strom et al., 1989; Skrutskie et al., 1990). This is explained as a circumstellar disk that has an optically thin inner disk and an optically thick outer disk. These disks are thought to represent a short-lived time of inside-out clearing of the disk. Indeed, the stellar accretion rate decreases with age for T Tauri stars(Hartmann et al., 1998; Sicilia-Aguilar et al., 2005), while the far-infrared excess that traces the outer disk is depleted on longer timescales (Meyer et al., 2008). The timescale of depletion of gas and dust in circumstellar disks limits the time available for planet formation.

It is not entirely clear how the transitional phase is tied to planet formation. Najita et al. (2007) summarize four scenarios that result in a disk that gives rise to a transitional SED:

Grain growth (Strom et al., 1989; Dullemond & Dominik, 2005) - dust agglomerates into into small bodies, decreasing the opacity of dust while leaving the gas density the

same. The gas remains as thermally excited emission lines throughout the inner disk.

Companion < 5 M_{Jup} (Skrutskie et al., 1990) - a Jupiter-mass planet will slow down the replenishing of material from the outer disk to the inner disk, causing the inner disk to be filled with less material (Lubow et al., 1999). As the planet forms, the planet creates a gap similar to that of the moons of Saturn sculpting the rings (Lubow et al., 1999; Lubow & D'Angelo, 2006). Material from the outer disk continues to flow inward. As the amount of material (both gas and dust) near the planet will be relatively little, gas will be contained close to the host star while the inner region empties. HD 100546 may be an example of this scenario (Brittain et al., 2009).

Companion > 5 M_{Jup} (Lubow et al., 1999) - if the mass of the planet exceeds 5 M_{Jup}, this will stop the replenishing of the inner disk entirely, and likewise halt accretion of material from the inner disk onto the host star. There will be a very massive outer disk as the accretion flow has halted and the outer disk cannot empty material. The inner gas will quickly accrete onto the host star, thus this transitional disk will not show any gas emission from the inner disk. HD 141569 is an example of this scenario (Brittain et al., 2007a).

Photoevaporation (Clarke et al., 2001) - the inner disk is heated by the star, eventually decoupling the inner disk and outer disk. The inner disk accretes, while the outer disk is evaporated over time. The gas has been accreted, leaving behind an empty inner disk.

These scenarios show that studying planet formation requires an understanding the disk as a whole - studying *both the circumstellar gas and dust.*

CO has been a successful tracer of the gas in a circumstellar disk. For example, sub-mm observations of CO are used to probe the outer disk (e.g. Dent et al., 2005). However, to probe the inner, planet-forming region of the disk, we use ro-vibrational transitions of CO. These have been detected in many cases (Najita et al., 2000, 2003, 2007; Brittain et al., 2003, 2007a, 2009; Blake & Boogert, 2004; Rettig et al., 2004; Goto et al., 2007; Pontoppidan et al., 2008; Salyk et al., 2009; van der Plas et al., 2009).

We present observations of ro-vibrational CO in the circumstellar disks around Herbig Ae/Be (HAeBe) stars in order to 1) learn how the circumstellar gas correlates with the dust and/or accretion diagnostics and 2) determine the distribution. There are 41 total HAeBes presented: 27 from this work, and 14 from previous studies (Blake & Boogert, 2004; Brittain et al., 2007a, 2009). In the cases of transitional disks, we use resolved spectra of molecular emission lines to trace the distribution of gas in the inner disk, attempting to distinguish between the scenarios.

The paper is organized as follows: the observations and sample justification are described in §3.1. The results and how they can be used to understand the disk morphology are summarized in §3.2. Finally, a brief discussion about what the results can be used to infer are described in §2.2.4.

3.1 Observations

Included in this survey are 41 HAeBe objects, combining 27 objects observed here with other studies of HAeBe stars (Blake & Boogert, 2004; Brittain et al., 2007a, 2009). These have been observed using PHOENIX (Hinkle et al., 2003, 2000, 1998) at the Gemini South telescope and NIRSPEC (McLean et al., 1998) at the Keck II telescope. Both are high-resolution near infrared spectrographs, with resolutions of $R = 50,000$ and $R = 25,000$, respectively. A summary of observations are presented in table 4.1.

Observations in the M-band are dominated by a strong thermal background. Therefore, an ABBA nod pattern between two positions $\sim 5''$ is used to cancel the thermal continuum to first order. The scans are flat fielded, cleaned of hot and dead pixels, including cosmic ray hits, and then combined in the sequence $(A_1\text{-}B_1\text{-}B_2\text{+}A_2)/2$, resulting in two rows which are summed to produce a spectrum. This spectrum is combined with an atmospheric transmittance model spectrum in order to find a wavelength solution. The model is created using the Spectral Synthesis Program (Kunde & Maguire, 1974), which accesses the HITRAN molecular database (Rothman et al., 1998, 2003). Each spectrum is then ratioed to a standard star observed at a similar airmass. Areas where the transmittance falls below 50% are omitted.

3.2 Results

This survey consists of 41 HAeBe stars, spanning a wide range of sources. We combine our observations of 27 HAeBe stars with objects from Blake & Boogert (2004), Brittain et al. (2007a), and Brittain et al. (2009). The survey sample spans spectral types B8-F7, and represents disks in a wide range of evolutionary state (debris disks, transitional disks, full disks, and non-detected disks). The sample includes 2 intermediate-mass T Tauri stars (CO Ori and GW Ori) and 2 debris disks (β Pictoris and 49 Ceti). A summary

Table 3.1 Log of Observations

Object	Date	Instrument	Spectral Range (cm^{-1})	Integration Time (m)
CO Ori...	2006 Jan 13	PHOENIX	2027 - 2038	20
GW Ori...	2006 Jan 13	PHOENIX	2027 - 2038	16
T Ori...	2008 Mar 22	PHOENIX	2141 - 2150	16
	2006 Jan 13	PHOENIX	2027 - 2038	20
V380 Ori...	2006 Jan 13	PHOENIX	2027 - 2038	16
HD 37357...	2008 Mar 22	PHOENIX	2141 - 2150	16
HD 37806...	2006 Jan 13	PHOENIX	2027 - 2038	16
HD 38678...	2008 Mar 23	PHOENIX	2104 - 2113	8
HD 49662...	2008 Mar 22	PHOENIX	2141 - 2150	16
HD 97048...	2008 Mar 22	PHOENIX	2141 - 2150	24
	2008 Mar 23	PHOENIX	2104 - 2113	32
	2006 Jan 13	PHOENIX	2028 - 2038	20
HD 98922...	2006 Jan 13	PHOENIX	2027 - 2038	12
HD 100453...	2007 Feb 6	PHOENIX	2006 - 2016	8
HD 101412...	2006 Jan 13	PHOENIX	2027 - 2038	16
HD 104237...	2007 Feb 7	PHOENIX	2139 - 2148	8
	2007 Feb 6	PHOENIX	2006 - 2016	8
HD 121847...	2008 Mar 23	PHOENIX	2104 - 2113	16
HD 135344b...	2007 Feb 7	PHOENIX	2142 - 2151	16
	2008 Mar 23	PHOENIX	2104 - 2113	40
	2007 Feb 6	PHOENIX	2006 - 2016	8
HD 139614...	2007 Feb 7	PHOENIX	2139 - 2148	24
	2007 Feb 6	PHOENIX	2006 - 2016	16
HD 142527...	2008 Mar 22	PHOENIX	2141 - 2150	16
	2008 Mar 23	PHOENIX	2027 - 2038	8
HD 142666...	2008 Mar 22	PHOENIX	2141 - 2150	16
HD 144432...	2008 Mar 22	PHOENIX	2141 - 2150	16
HD 144668...	2008 Mar 22	PHOENIX	2141 - 2150	8
	2008 Mar 23	PHOENIX	2027 - 2038	8
HD 150193...	2008 Mar 22	PHOENIX	2141 - 2150	8
	2008 Mar 23	PHOENIX	2027 - 2037	8
HD 158352...	2008 Mar 22	PHOENIX	2141 - 2150	16
	2008 Mar 23	PHOENIX	2027 - 2037	8
HD 169142...	2007 Feb 7	PHOENIX	2142 - 2151	24
	2007 Feb 6	PHOENIX	2006 - 2016	24
HR 4796A...	2008 Mar 23	PHOENIX	2104 - 2113	48
49 Ceti...	2007 July 24	NIRSPEC	2120 - 2152	12
			1988 - 2018	12
Beta Pic...	2008 Mar 23	PHOENIX	2104 - 2113	16
	2006 Jan 14	PHOENIX	2084 - 2093	28
PDS 144N...	2008 Mar 22	PHOENIX	2141 - 2150	16
	2008 Mar 23	PHOENIX	2104 - 2113	24
	2008 Mar 23	PHOENIX	2027 - 2037	56

of results are shown in table 3.2. With this sample, the relation of disk parameters to circumstellar gas is explored. Appendix 3.6 contains a short description of each object, including the references for table 3.2. The individual spectra for each object are shown in figures 3.10 through 3.36.

Table 3.2

Summary of Disks

Object	Sepectral Type	d (pc)	Age (Myr)	Meeus Group	K-L	PAH[1]	Pf β?	Brγ Luminosity (erg s^{-1})	L(P30 or P26) (erg s^{-1})	CO[2]
This Work										
CO Ori...	F7V	400	3.3	II	1.07	N	···	···	4.0×10^{29} P(26)	T
GW Ori...	G5	308	1.0	Ia	1.09	N	···	···	1.2×10^{29} P(26)	T
T Ori...	A3IV	400	2.8	II	1.17	N	Y	···	6.3×10^{29} P(26)	T
V380 Ori...	A1	510	7.4	II	1.59	N	···	3.9×10^{31}	9.0×10^{29} P(26)	T
HD 37357...	A2V	240	10.0	II	0.91	N	Y	···	···	N
HD 37806...	A2V	470	0.8	II	1.54	N	···	$> 7.3 \times 10^{30}$	8.2×10^{29} P(26)	T
HD 38678...	A2V	21.5	231	II	0.2	···	···	···	···	N
HD 49662...	B7IV	188	···	Ib	-0.2	···	N	···	···	N
HD 97048...	B9.5V	180	3	Ib	1.43	S	Y	5.6×10^{30}	5.5×10^{28} P(26)	F
HD 98922...	B9Ve	203	2.6	II	1.61	S	···	1.4×10^{31}	4.1×10^{29} P(26)	F
HD 100453...	A9V	111	10	Ib	1.32	S	···	5.2×10^{29}	$< 1.3 \times 10^{27}$ P(30)	N
HD 101412...	B9.5V	600	2	II	1.41	S	···	···	7.3×10^{29} P(26)	F
HD 104237...	A4IV	116	4.8	II	1.37	N	Y	6.5×10^{30}	2.1×10^{29} P(30)	T
HD 121847...	B8V	104	···	···	-0.05	···	···	···	···	N
HD 135344b...	A0V	140	8	Ib	0.48	S	Y	5.7×10^{29}	···	T
HD 139614...	A7V	140	> 10	Ia	1.08	M	N	5.7×10^{29}	9.8×10^{27} P(30)	F
HD 142527...	F6III	140	1	Ia	1.31	M	Y	1.2×10^{30}	2.2×10^{29} P(26)	T
HD 142666...	A8V	116	4.4	II	1.07	N	Y	7.2×10^{29}	···	N
HD 144432...	A9V	124	6.65	II	1.00	M	Y	2.7×10^{30}	···	T
HD 144668...	A7	207	0.5	II	1.06	N	Y	2.4×10^{31}	2.0×10^{29} P(30) 3.8×10^{29} P(26)	T
HD 150193...	A2IV	150	2.6	II	1.27	N	Y	···	6.8×10^{28} P(26)	T
HD 158352...	A8V	63	750	Ib	0.93	···	N	···	$< 3.8 \times 10^{27}$ P(26)	N
HD 169142...	A5V	145	5	Ib	0.89	M	N	2.7×10^{30}	$< 2.9 \times 10^{27}$ P(30)	T
HR 4796A...	A0V	67	8	Ib	···	···	···	···	···	N

– continued from previous page

Object	Sepectral Type	d (pc)	Age (Myr)	Meeus Group	K-L	PAH[1]	Pf β?	Brγ Luminosity (erg s^{-1})	L(P30 or P26) (erg s^{-1})	CO[2]
49 Ceti...	A4V	61	8	II	-0.3	N	N	···	$< 7.6 \times 10^{26}$ P(30)	N
Beta Pic...	A5V	19.3	20	II	-0.2	N	···	···	···	N
PDS 144N...	A2IV	1000	···	Ia	1.92	S	Y	···	4.9×10^{30} P(26)[3] d	T
From Blake & Boogert (2004)										
HD 36112	A8	160	3.2	Ia	1.15	···	Y	2.3×10^{30}	3.5×10^{28} P(30)	T
HD 31648	A5	130	2.5	Ia	1.08	M	Y	3.8×10^{30}	1.5×10^{28} P(30)	T
VV Ser	A0	250	0.6	II	1.49	M	Y	1.8×10^{31}	3.1×10^{28} P(30)	T
From Brittain et al. (2007a)										
HD 31293...	A0	144	4.8	Ia	1.07	···	Y	3.8×10^{30}	1.8×10^{29} P(30)	F
HD 38087...	B6	199	< 0.5	II	-0.08	···	N	···	$< 5 \times 10^{27}$ P(30)	N
HD 58647...	B9	277	0.2	···	1.4	···	Y	···	1.3×10^{29} P(30)	T
HD 141569...	A0	108	5	II	0.21	M	Y	···	5×10^{26} P(30)	F
HD 149914...	B9.5	165	0.75	···	0.08	···	N	5.6×10^{29}	$< 7 \times 10^{27}$ P(30)[4] e	N
HD 158643...	B9.5	131	0.3	II	0.90	···	N	4.0×10^{30}	4.5×10^{29} P(30)	T
HD 163296...	A1	122	6.0	II	1.18	M	Y	1.1×10^{31}	7.5×10^{28} P(30)	T
HD 250550...	B7	696	1	Ib	1.04	N	Y	3.4×10^{31}	2.0×10^{30} P(30)	F
HD 259431...	B2	290	0.2	Ia	1.36	N	Y	9.6×10^{31}	3.7×10^{29} P(30)	T
SAO 185668...	B3	700	···	···	0.56	···	N	···	$< 8 \times 10^{27}$ P(30)	N
From Brittain et al. (2009)										
HD 100546...	B9	103	10	Ia	1.05	S	Y	···	9.3×10^{28} P(30) 1.3×10^{29} P(26)	F

– continued from previous page

Object	Sepectral Type	d (pc)	Age (Myr)	Meeus Group	K-L	PAH[1]	Pf β?	Brγ Luminosity (erg s^{-1})	L(P30 or P26) (erg s^{-1})	CO[2]

[1] S = "Strong" PAH emission observed; M = "Moderate" PAH emission observed; N = No PAH emission observed

[2] T = Only v=1-0 transitions observed; F = v=1-0 and v=2-1 or greater observed; N = no detection

[3] MC = Possible massive companion; LC = Possible low-mass companion; P = Photoevaporation; G = Grain growth

[4] The CO in PDS 144N is actually in absorption. The Luminosity is calculated by the absolute value of the equivalent width of the feature.

[5] Extrapolated from lower excitation lines.

Table 3.3

PAH Summary for Disks

Object	3.3 μm Feature ($\times 10^{-15}$) W m^{-2}	6.2 μm Feature ($\times 10^{-15}$) W m^{-2}	Reference[1]
CO Ori...	< 0.69	...	1
T Ori...	< 6.2	...	1
V380 Ori...	< 8.6	...	1
HD 37357...	< 0.62	...	1
HD 37806...	< 1.7	...	1
HD 97048...	6.5	...	1
	18.5	88.3	2
HD 98922...	44	...	3
HD 100453...	8.99	26.3	2
HD 101412...	1.3	...	1
	2.8	...	3
HD 104237...	< 2.54	< 2.00	2
HD 135344b...	3.06	10.9	2
	...	3.47	4
HD 139614...	< 2.83	6.07	2
HD 142527...	7.21	< 16.9	2
HD 142666...	< 2	...	1
HD 144668	< 1.1	< 7.54	2
HD 144432...	< 1.75	8.98	2
HD 150193...	< 1.3	...	1
	< 3.06	< 1.81	2
HD 169142...	< 7.38	19.3	2
	...	32.71	4
HD 31648	< 2.41	15.9	2
VV Ser	< 2.3	...	1
	< 2.63	10.6	2
HD 141569...	< 2.42	6.91	2
	...	6.84	4
	≤ 0.69	...	3
HD 163296...	< 12	...	1
	< 3.04	26.1	2
HD 250550...	< 5.9	...	1
HD 259431...	< 3.2	...	1
HD 100546...	24	...	1
	24	121	2

[1] For references, 1 is from Acke & van den Ancker (2006b), 2 is from Acke & van den Ancker (2004), 3 is Geers et al. (2007), and 4 is Sloan et al. (2005).

Overall, CO is detected in 28/41 sources, for an overall detection rate of 68%. In the sources with observed CO, the emission ranges from a few percent above the continuum, up to $\sim$ 25% above the continuum. The average emission is $15 - 20\%$. PDS 144N, the only observed in absorption, has features that are $30 - 50\%$ deep. Most of the lines are resolved and centrally peaked. The emission is symmetric to within $\sim 5\%$; any outflows or inflows would show as asymmetric features, such as those seen in V1647 Ori (Brittain et al., 2007b). When observations of a source sampled high and low J lines, only one source revealed emission for low-J, but not high-J (HD 169142). This may be due to a low-quality spectrum, as seen in figure 3.32.

Of the 28 sources that show CO detections, most systems (20/28; 71%) with observed CO show only v=1-0 emission . The sources with emission from higher vibrational levels are HD 97048, HD 98922, HD 101412, HD 139614, HD 31293, HD 141569, HD 250550, and HD 100546.

3.2.1 K-L

The hot gas can be compared with the hot dust probed by the K-L excess (Strom et al., 1989; Skrutskie et al., 1990; Hillenbrand et al., 1992; Malfait et al., 1998; Haisch et al., 2001; Dullemond et al., 2001). The warm gas is traced by collisionally excited CO. If the gas and dust are co-spatial, then one might expect that K-L is related to the luminosity of CO. Figure 3.1 shows the detection rate of CO as a function of K-L.

Overall detection rates of CO compared to different K-L bins are shown in figure 3.1. Four bins are used (detection rates in parenthesis): K-L$<$ 0.5 (2/9), 0.5 $\leq$K-L$<$ 1.0 (2/5), 1.0 $\leq$K-L$<$ 1.25 (12/13), and 1.25 $\leq$K-L$<$ 1.5 (12/13). The bins were chosen to see if there is a sharp cutoff in detection rates as a function of K-L. Overall, the detection rate is much higher in sources with a high K-L ($>$ 1.0; 92%) versus those sources with a low K-L ($<$ 1.0; 29%). Thus, it appears that there is a sudden cutoff of CO detections as a function of K-L.

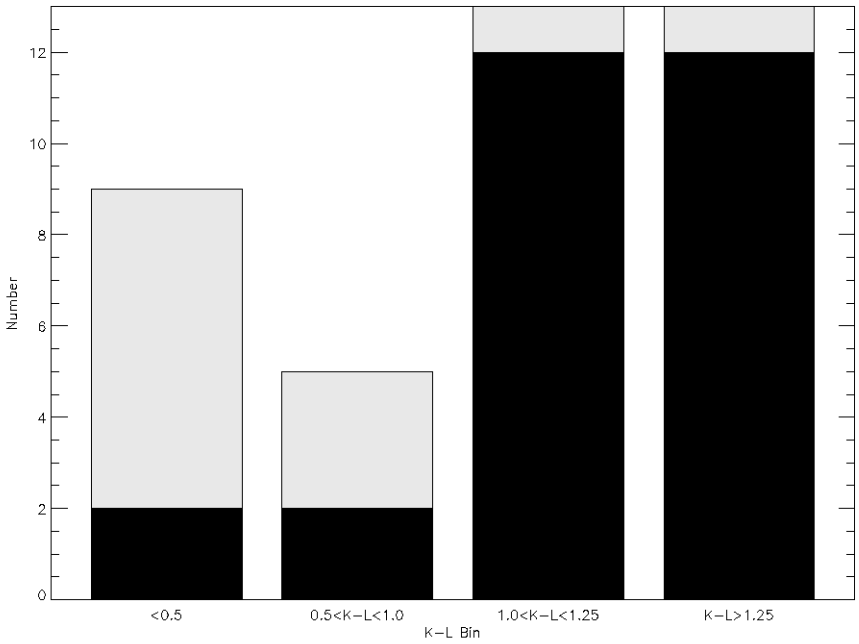

Figure 3.1 CO detection rate versus K-L excess. The total number in each bin is plotted in light gray, while the number of CO detections are shown in black. The sources with a low K-L have a much lower detection rate than those with a high K-L.

For the hot gas, we use the v=1-0 P(26) and P(30) line luminosities as tracers. These lines are free of telluric features that may contaminate the lines. Figure 3.2 shows the relation of the CO luminosity to K-L for sources with an observed P(26) or P(30) feature. A correlation is seen, where sources with a high K-L value show a high CO luminosity, while low K-L excess sources show low or non-detected CO. For sources with a K-L$>$ 0.85, all but three have detections of the high-J lines (HD 100453, HD 158352, and HD 169142). This is different than the 100% (9/9) detection rate seen by Brittain et al. (2007a), yet within the statistical uncertainty given the sample size. As mentioned before, HD 169142 has low-quality data, so the meaning of a non-detection is unclear. The two other sources that have no CO despite a high K-L (HD 100453 and HD 158352), will be discussed in §3.2.8.

Upper limits of HD 100453, HD 158352, and HD 169142 in table 3.2 are calculated by assuming the instrument profile is the width of the feature. However, most features

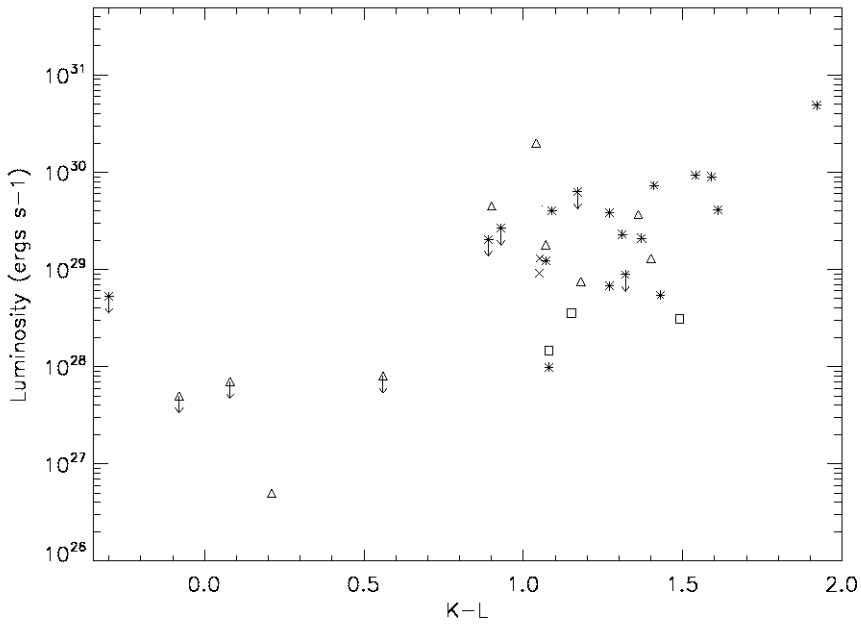

Figure 3.2 CO high-J luminosity versus K-L magnitude from this study (asterisks) and previous work (triangles). Upper limits reported from this study assume a rotational broadening a factor of ~ 70 higher than the instrument resolution (described in the text).

are much wider than the 6 km s^{-1} (0.04 cm^{-1}), as seen in the detections reported here. As an extreme example, Brittain et al. (2007a) observed a width of the P(30) feature in HD 158643 of ~ 400 km s^{-1}. If this is the case for the three non-detections here, the true upper limit would be increased by up to a factor of ~ 70. The "true" upper limits are those plotted in figure 3.2.

Naively, one might expect that this shows that the dust and gas simply correlate. It is possible that K-L traces the warm dust. However, it is also possible that the gas is not heated in the upper atmosphere of the disk, where the CO is being observed. Further, it is not clear why the CO is mostly observed in disks that evidently harbor a lot of dust. To explore this we turn to the excitation of CO in disks.

3.2.2 Meeus Groups

Meeus groups are defined by the SED in the mid-infrared, around 10 μm (Meeus et al., 2001). Group Ia and Ib sources have a dominant, rising MIR excess, while group II sources have a smaller and descending MIR excess. The difference between Ia and Ib sources have to do with solid state bands: Ia sources have solid state features, Ib sources do not. Further, group I sources are interpreted as highly flared disks with a large illuminated area of the disk atmosphere, while the group II sources are assumed to have a high degree of self-shielding, limiting the area of the disk illuminated by the host star (see Ardila et al., 2007).

The detection rate for Ia sources is 100% (9/9), for Ib sources is 50% (4/8), and for group II sources is 70% (14/20). The detection rates for each Meeus group are shown in figure 3.3. We see a higher detection rate for the group I sources compared to the group II sources, consistent with the expectations from a flared/non-flared disk (see figure 3.3). The group II source detection rate is comparable to the overall detection rate for the sources. However, a large difference is seen between the group Ia and Ib sources. Meeus et al. (2001) suggest that Ib sources are those with either a missing inner region of dust, or with a lack of small grains ($\leq 50\mu m$). Thus, in Ib sources, the gas may deplete in the inner region (along with the dust), or the large grains fail to supply a heating mechanism sufficient to excite the circumstellar CO.

3.2.3 PAHs

Ro-vibrational CO emission comes from the thin disk atmosphere. Models have shown that PAH emission is important to heating the upper disk atmosphere (Kamp & Dullemond, 2004). In fact, PAH heating is stronger in HAeBes than T Tauris (Visser et al., 2007). Thus, one would expect that the CO emission would scale with the PAH luminosity. To show the effect of PAH heating on the CO luminosity, a comparison between the disks around HD 100546 and HD 141569 is informative. The two sources have similar disks and similar CO distributions, yet the CO temperature in HD 100546 is much larger than the CO temperature in HD 141569 (Brittain et al., 2007a, 2009). The only difference between them seems to be the luminosity of PAHs in these sources. The PAH luminosity in

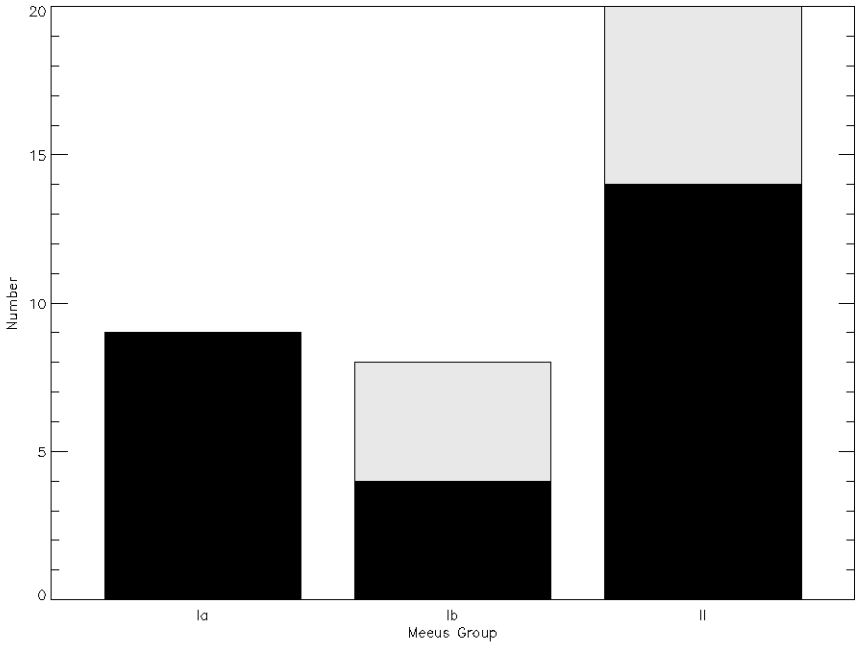

Figure 3.3 CO detection rate versus Meeus group. The total number in each bin is plotted in light gray, while the number of CO detections are shown in black.

HD 100546 is much larger than the PAH luminosity in HD 141569 (almost twice as large; Acke & van den Ancker, 2004), suggesting that PAHs are very important to the heating of the gas in a circumstellar disk at large radii.

To this end, we compare the detection of CO as a function of PAH luminosity. In sources that are described as "strong" PAH emitters, 85% of the sources are detected (6/7). Moderate and non-PAH emitters have detection rates of 100% (8/8), and 71% (10/14), respectively. The non-PAH source detection rate is comparable to the overall detection rate, while the other detection rates are higher than expected. These detection rates are plotted in figure 3.4. Of the detections classified as strong PAH sources, 4/6 are fluoresced sources. Of the detections in sources classified as moderate PAH emission, only 2/8 sources are found to be fluoresced.

Table 3.3 shows the luminosities of the different PAH features. These are plotted against the luminosity of CO in Figures 3.5 and 3.6. There does not seem to be any relation

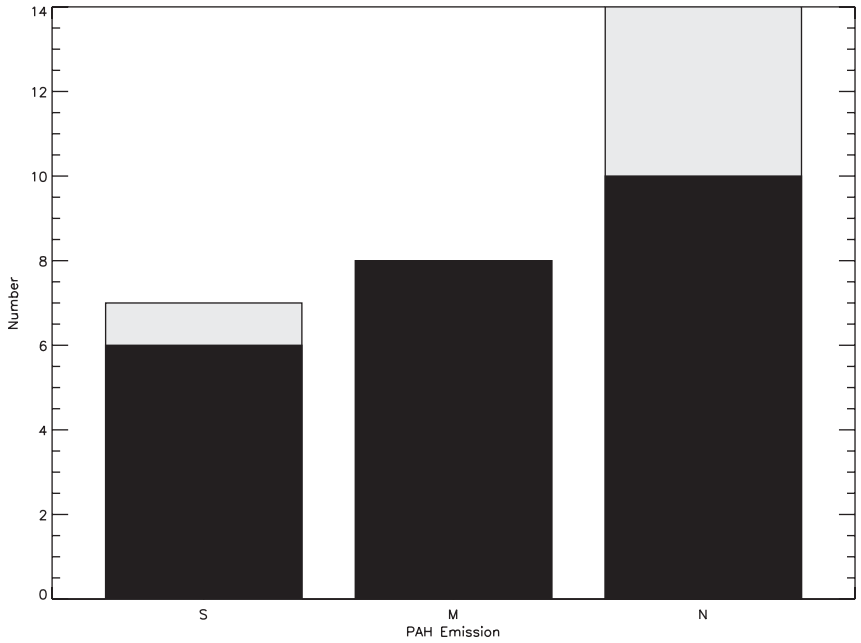

Figure 3.4 CO detection rate versus PAH emission. The total number in each bin is plotted in light gray, while the number of CO detections are shown in black.

between the CO luminosity and the PAH luminosity. The CO luminosity plotted probes high rotational gas temperature. If the PAH luminosity probes the fluorescent excitation (as hinted by the high number of fluoresced sources detected with strong PAH emission), then it does not necessarily have a connection to the rotational temperature.

3.2.4 Br γ

The hydrogen line Brγ has been empirically tied to accretion in T Tauris and intermediate-mass T Tauris (Muzerolle et al., 1998; Calvet et al., 2004). Brγ seems to be correlated to CO luminosity, though it may be questionable to use as a tracer of accretion in early type HAeBe stars (Brittain et al., 2007a; Donehew et al., 2010).

A correlation between the CO luminosity and Brγ luminosity is observed, which is shown in figure 3.7. As mentioned in §3.2.1, the upper limits of HD 100453, HD 158352, and HD 169142 from this study are increased by a factor of 70 to account for possible line

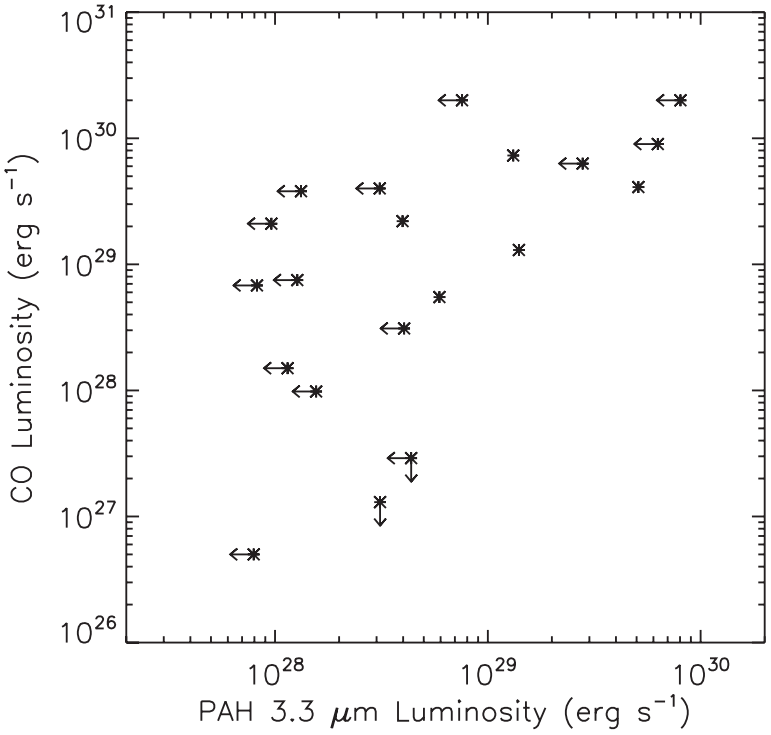

Figure 3.5 CO luminosity versus PAH 3.3 μm luminosity.

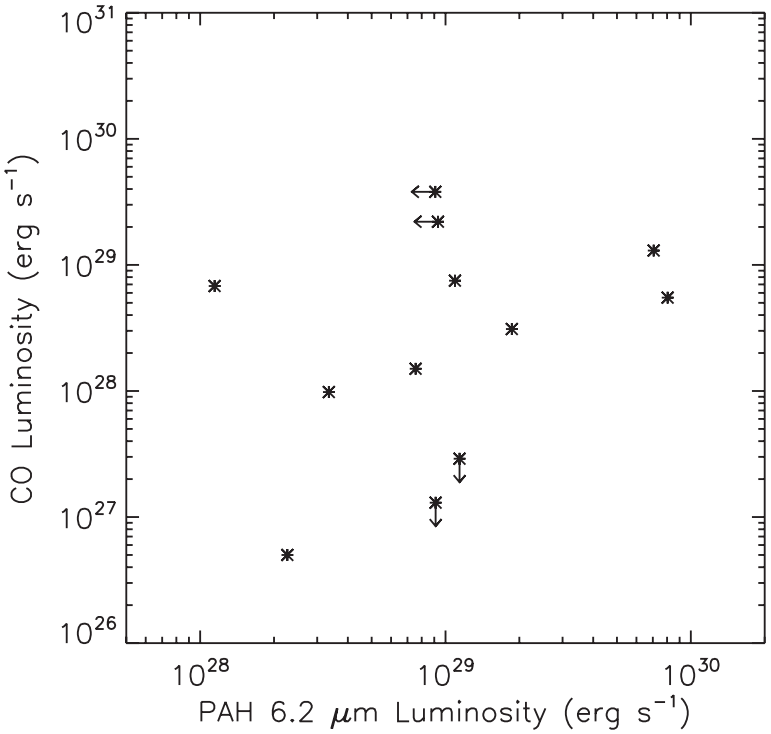

Figure 3.6 CO luminosity versus PAH 6.2 μm luminosity.

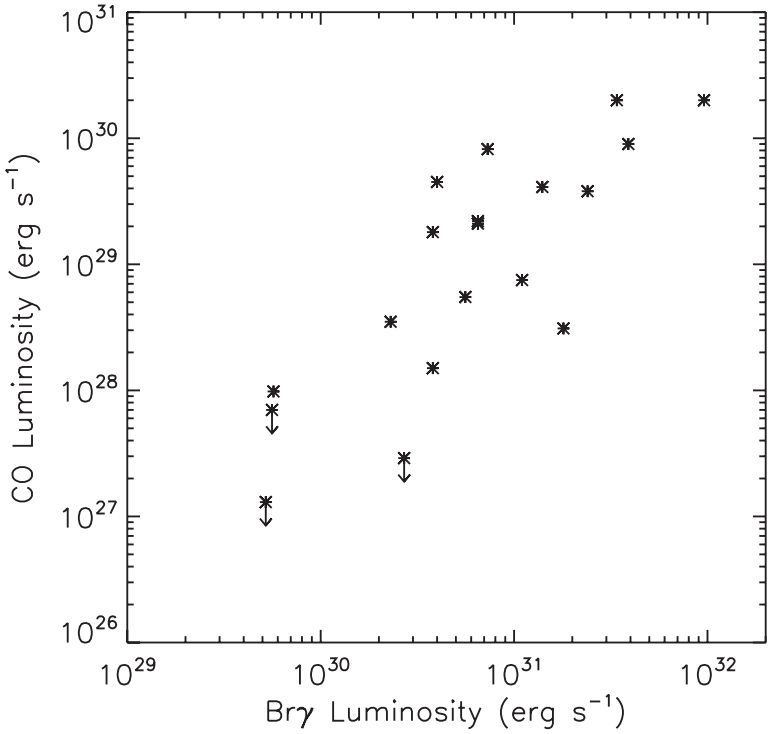

Figure 3.7 CO luminosity versus Brγ luminosity.

broadening. As the Brγ is tracing accretion, it a closer relation to the gas temperature, reflected by the CO luminosity.

3.2.5 Pf β

Pfβ is centered at 2149.38 cm^{-1}. When observed, this feature is very broad (e.g. HWZI of 200 km s^{-1} for HD 97048). The feature emission ranges from 0% to 80% over the continuum, with an average of $\sim$ 15%. Most of the sources (30 of 41) were observed over a spectral range that included this wavelength. Of the 30 sources, 21 showed Pfβ, while 9 do not. The detection rates of CO are 90% (19/21) for sources that show Pfβ and 33% (3/9) for those that do not show Pfβ. The detection rates versus detections of Pfβ are shown in figure 3.8. The high detection rate for sources with Pfβ compared to the non-detections of those without Pfβ implies that Pfβ is closely tied to circumstellar gas.

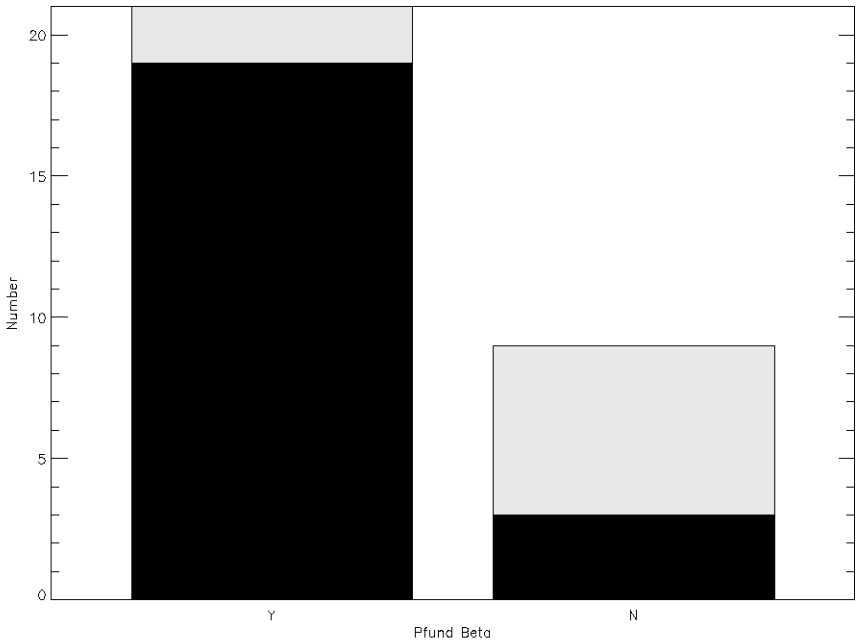

Figure 3.8 CO detection rate versus Pf β detections. The total number in each bin is plotted in light gray, while the number of CO detections are shown in black.

3.2.6 Age

To determine a possible evolution of gas in disks, one can look at the relation of circumstellar gas as a function of age. As pre-main sequence ages for stars are somewhat uncertain, we bin over large age ranges in order to account for such uncertainties. The bins and detection rates are 75% (6/8) for < 1 Myr, 100% (9/9) for 1-3 Myr, 69% (11/16) for 3-10 Myr, and 25% (1/4) for > 10 Myr. The detections versus different age bins are shown in figure 3.9. The detection rate is very high for systems younger than 5 Myr and drops off after 10 Myr.

3.2.7 HD 97048 and HD 169142

These sources show evidence for fluoresced gas. For HD 97048, transitions up to and including v=5-4 are observed, while in HD 169142, there are hints of observed v=2-1 emission (too low S/N to confirm), yet no high-J lines are observed. The high vibrational

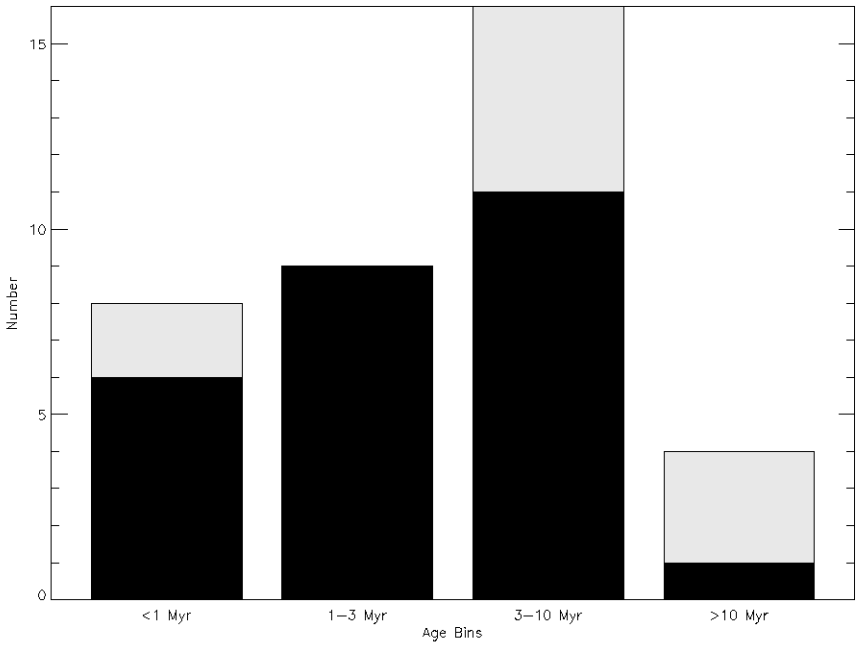

Figure 3.9 CO detection rate versus age bins. Age estimates are somewhat uncertain, so the bins are wide. There is only one detection for age of > 10 Myr, which is HD 139614.

temperature and low(er) rotational temperature is evidence for fluoresced gas. HD 97048 will be explored further in a future paper.

Grady et al. (2007) looked at the possible scenarios causing the transitional nature of the disk around HD 169142 and suggest an embedded planet. Observations of CO can rule out scenarios that may be occurring. If fluoresced CO is observed in this object, then the UV photons from the host star must be exciting the CO. This likely rules out the photoevaporation scenario, as the inner cavity would be evacuated to a large radius. Also, as high-J lines are not observed, thermally excited CO is not seen, likely ruling out the grain growth scenario. This leaves only an embedded planet as a possible scenario, in agreement with Grady et al. (2007).

3.2.8 HD 100453 and HD 158352

These two sources represent interesting non-detections. Both have K-L>0.85, which has a high detection rate, yet show no CO emission. Both are Meeus group Ib sources with similar $Br\gamma$ luminosities. As mentioned earlier, group Ib sources may represent sources with depleted gas in the inner disk. Alternatively, there may be a lack of heating in the upper layers of the disk. The disk heating will be discussed in §2.2.4.

3.2.9 HD 139614

This is an older source (> 10 Myr) that shows warm gas. However, there is evidence for older systems do have fluoresced gas, such as HD 100546 at an age of 10 Myr (Brittain et al., 2009).

It should be noted that the age is determined by fitting to pre-main sequence evolutionary tracks, which has uncertainties. The evolutionary tracks use a luminosity, temperature and stellar mass to derive an age - all having errors additional to those of the evolutionary model.

3.2.10 HD 142666

Has no detection of CO, yet a distinct Pfβ feature, a high K-L, Brγ detection, and moderate PAH emission. Somehow, the CO is remaining hidden.

3.2.11 PDS 144N

PDS 144N is the first resolved HAeBe star with an edge-on disk (Perrin et al., 2006). CO is observed in absorption in this disk. Both ^{12}CO and ^{13}CO are observed, but no v=2-1 absorption is seen. However, the v=1-0 P(26) line is observed, which traces hot gas. There also seems to be a slight asymmetry in the features, specifically a tail towards the red. If this is indeed the case, it would represent the inflow of material. This source will be discussed in further detail in a future paper.

3.3 Discussion

The sample size of objects for a K-L between 0.5 and 1.0 is small. Probing this region will determine if there is a relation between CO luminosity and K-L (see figure 3.2).

Alternatively, if there is a cutoff point under which warm CO is not detected, one could determine where that exists by sampling this region.

The sample size of group Ib sources is large enough to see a potential dearth of CO detections, yet small enough to not be able to statistically state this claim. If assuming poisson statistics, the detection rate of Ib sources is $50 \pm 25\%$. Thus, the detection of CO in Ib sources, when including statistical error, falls within the overall detection rate (68%).

Cieza et al. (2007) found disk detections for stars between spectral type K-M range about 20% to 30%, from a sample of ~ 200 stars. This study observed circumstellar dust around T Tauri stars, but the detection rate is significantly different for observed gas in this study. Similarly, they find that $\sim 50\%$ of < 2 Myr disks show no inner material, which is also different for the detection rate of CO presented here for systems < 3 Myr (15/17). Perhaps the *early* evolution of a circumstellar disk around HAeBe stars is not entirely similar to the evolution around T Tauris.

Similarly, for sources > 10 Myr, only 1 source shows a detection of circumstellar gas. The rate of 25% is similar to the rate of observed IR excess in T Tauri disks ($\sim 5 - 20\%$) at this age (Mamajek et al., 2004). This shows that the evolution timeline of disks around HAeBe stars may be analogous to T Tauri stars despite differences at an earlier age. It should be noted that the evolution of an individual system is likely to be environment/initial condition dependent.

For the sources that show no CO emission, gas may be hidden in the inner disk. In order to observe gas in emission, there has to be a thermal inversion layer above the optically thick continuum in the disk. Some heating mechanism is necessary in the upper layers to produce the CO emission. Kamp et al. (2005) suggest that photoelectric heating is integral to the warming the disk atmosphere. Their modeling indicates that UV flux from the star liberates fast electrons from small dust grains and PAHs that then heat the gas.

Brittain et al. (2009) find some support for this scenario in their comparative study of the CO spectra of HD 141569 and HD 100546. In each case the inner 10AU of the disk is evacuated and UV fluoresced CO is observed extending outward from the inner edge of the disk. While the central stars are nearly identical and the disks are in the same evolutionary state, the effective temperature of the CO around HD 141569 is ~ 200K and the effective

temperature of the CO around HD 100546 is $\sim$ 1400K. In addition to the difference in temperature the PAH luminosity of HD 100546 is two orders of magnitude greater than that of HD 141569 as expected if photoelectric heating plays a prominent role in heating the atmosphere of the disk.

As observed in this study, we see a relation of strong PAH emission to CO detections, indicating that PAH heating is important in the inner disk.

Similarly, mechanical heating by accretion may also affect the disk temperature and create the warm molecular layer observed in CO line emission (Glassgold et al., 2004). However, there is no confirmed method to measure the accretion rate (Muzerolle et al., 2004; Brittain et al., 2007a). We observe a relation between Brγ luminosity and CO luminosity. This would suggest accretion heating also plays a role in the disk if the accretion relation to Brγ holds for HAeBe stars.

We have observed no sources with warm gas detections with a depletion of inner dust, which is described by the grain growth scenario. This may indicate that core accretion alone may not the dominant process in planet formation. We also see a correlation with hot dust and hot gas, but a cool disk is needed to create gravitational instabilities. A hybrid scenario is more likely to be involved in planet formation (e.g. Youdin & Shu, 2002).

3.4 Conclusion of Survey

The main points to take from this study are as follows:

- Fundamental CO is detectable in 26 out of 41 HAeBe stars presented in this study (63%).
- Sources with a K-L$<$ 1.0 has a much lower detection rate of CO than the sources with a K-L$>$ 1.0. This indicates that the emissivity of CO in the inner disk scales with the near-infrared excess from dust. This could be due to the geometry of the system.
- PAH emission is important to set the temperature of the outer disk, while accretion dominates the inner disk.
- We do not see any sources that represent the grain growth scenario, that is gas-rich systems with dust depletion.
- For sources $>$ 10 Myr, the detection rate of CO is much lower than the overall detection rate, though this is still within the statistics of the small sample size.

3.5 Spectra of Survey Sources

The spectra for the sources in the survey are shown in the following figures.

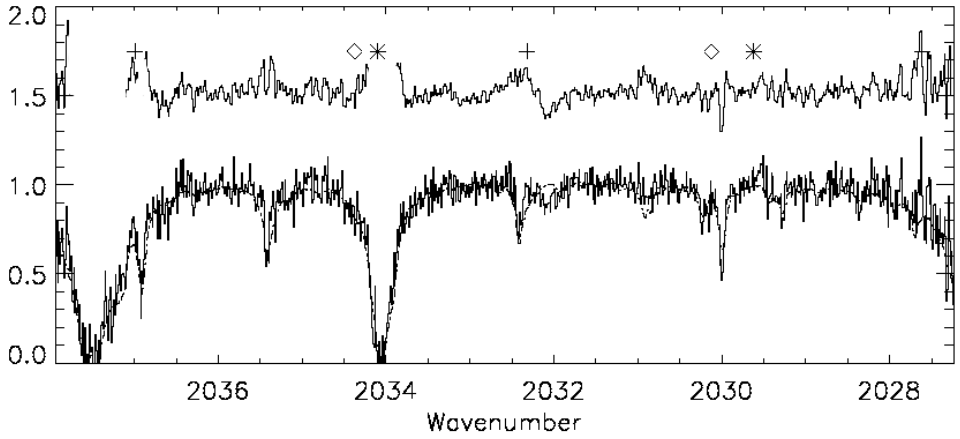

Figure 3.10 CO Ori. The science spectrum (solid line) and overplotted telluric standard Zeta Ori (dot-dashed line) are shown in normalized flux. The ratio is plotted, offset by 0.5. Areas where the transmittance is less than 50% are not plotted. CO transitions are shown for v=1-0 (cross), v=2-1 (asterisks), and v=3-2 (diamonds). The P(26) feature at ~ 2032.4 cm^{-1} is seen.

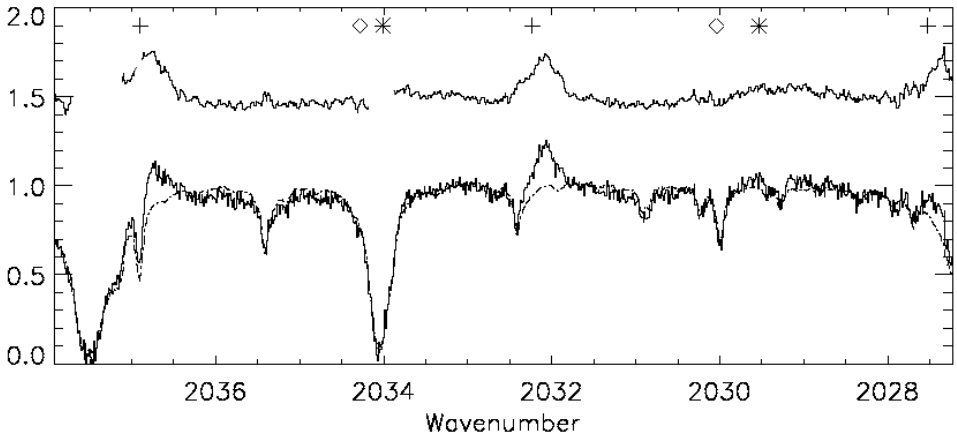

Figure 3.11 GW Ori. The science spectrum (solid line) and overplotted telluric standard Zeta Ori (dot-dashed line) are shown in normalized flux. The ratio is plotted, offset by 0.5. Areas where the transmittance is less than 50% are not plotted. CO transitions are shown for v=1-0 (cross), v=2-1 (asterisks), and v=3-2 (diamonds). The P(26) feature at ~ 2032 cm^{-1}, the P(25) feature at ~ 2037 cm^{-1}, and the P(27) feature at ~ 2027.5 cm^{-1} (at the end of the spectrum), are seen.

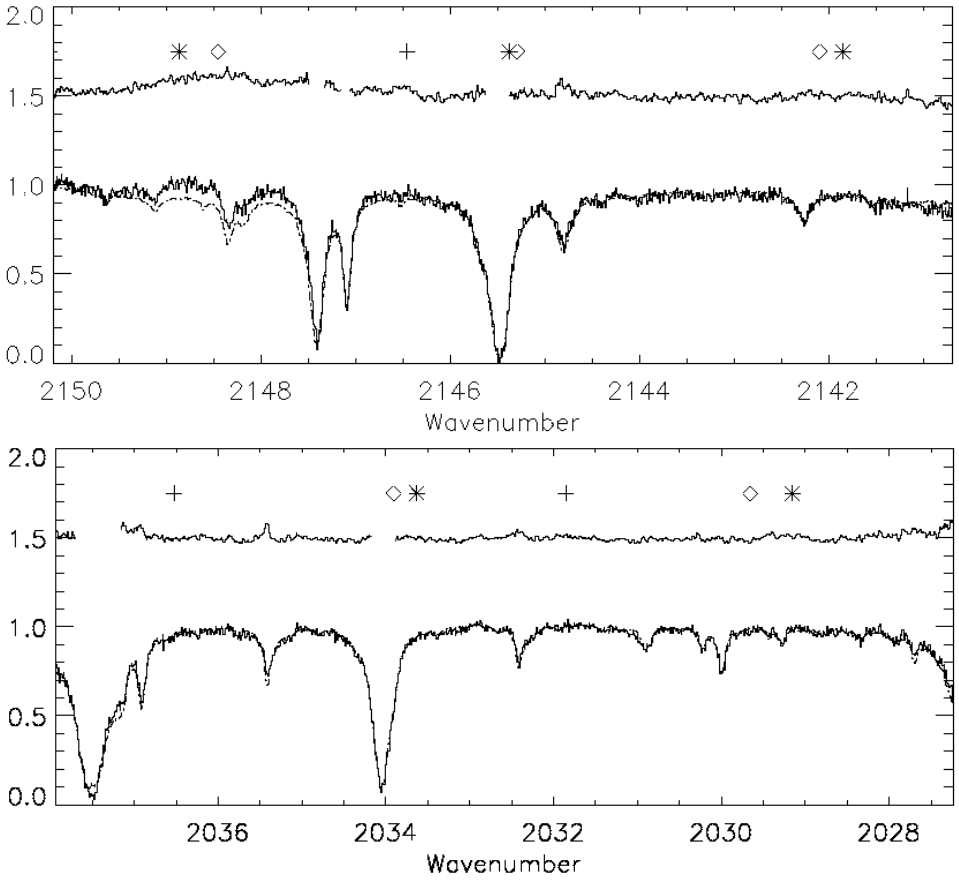

Figure 3.12 T Ori. The science spectrum (solid line) and overplotted telluric standards (dot-dashed line), Zeta Ori and HR 4798, for 2032 and 2146 settings, respectively. The ratio is plotted, offset by 0.5. Areas where the transmittance is less than 50% are not plotted. The broad Pfund Beta feature is seen, centered around 2149 cm^{-1}. CO transitions are shown for v=1-0 (cross), v=2-1 (asterisks), and v=3-2 (diamonds). ***CHECK DOPPLER SHIFT***

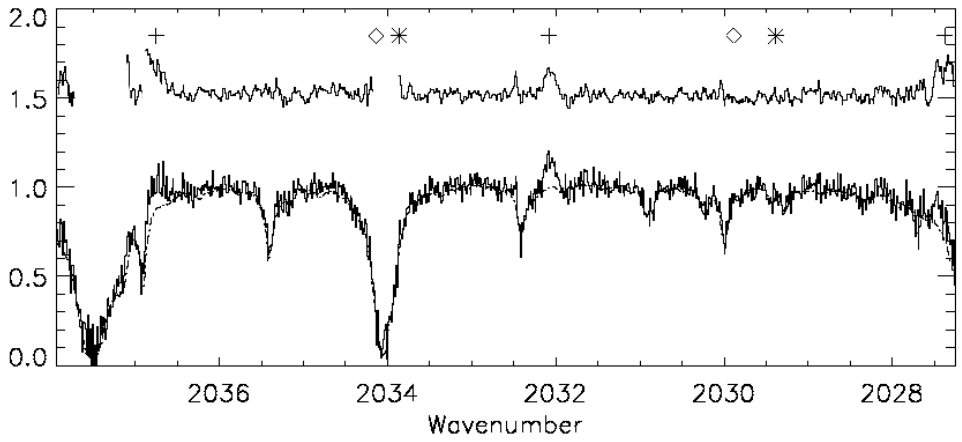

Figure 3.13 V380 Ori. The science spectrum (solid line) and overplotted telluric standard Zeta Ori (dot-dashed line) are shown in normalized flux. The ratio is plotted, offset by 0.5. Areas where the transmittance is less than 50% are not plotted. CO transitions are shown for v=1-0 (cross), v=2-1 (asterisks), and v=3-2 (diamonds). The P(26) feature at ~ 2032 cm^{-1} is clearly seen.

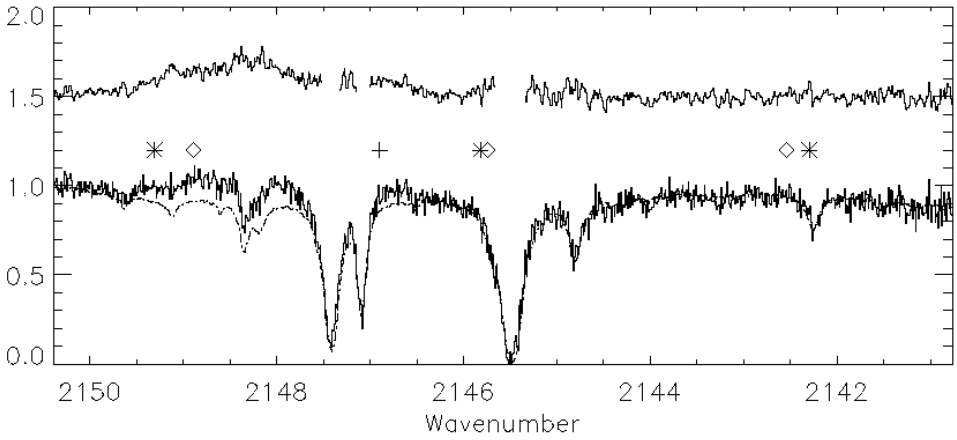

Figure 3.14 HD 37357. The science spectrum (solid line) and overplotted telluric standard HR 4798 (dot-dashed line) are shown in normalized flux. The ratio is plotted, offset by 0.5. Areas where the transmittance is less than 50% are not plotted. The broad Pfund Beta feature is seen, centered around 2149 cm^{-1}. CO transitions are shown for v=1-0 (cross), v=2-1 (asterisks), and v=3-2 (diamonds). No features are observed, including the R(0) line at ~ 2147 cm^{-1}

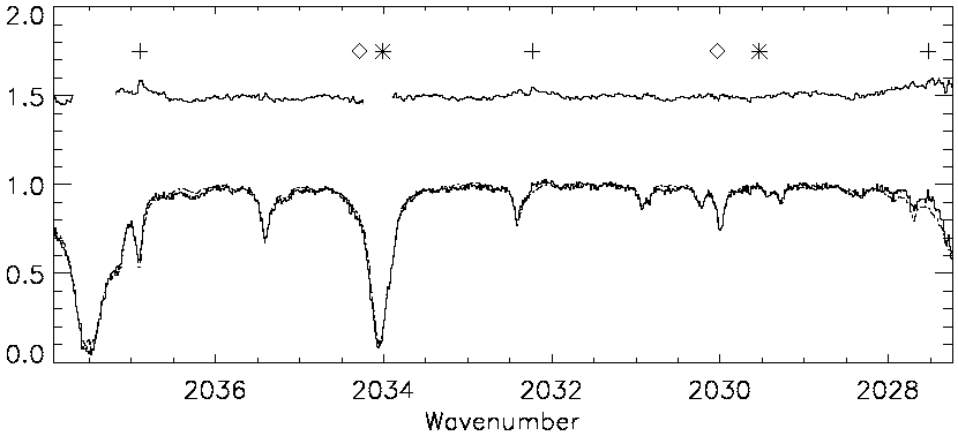

Figure 3.15 HD 37806. The science spectrum (solid line) and overplotted telluric standard Zeta Ori (dot-dashed line) are shown in normalized flux. The ratio is plotted, offset by 0.5. Areas where the transmittance is less than 50% are not plotted. CO transitions are shown for v=1-0 (cross), v=2-1 (asterisks), and v=3-2 (diamonds). The P(26) feature at ~ 2032 cm^{-1}, the P(25) feature at ~ 2037 cm^{-1}, and the P(27) feature at ~ 2027.5 cm^{-1} (at the end of the spectrum), are seen.

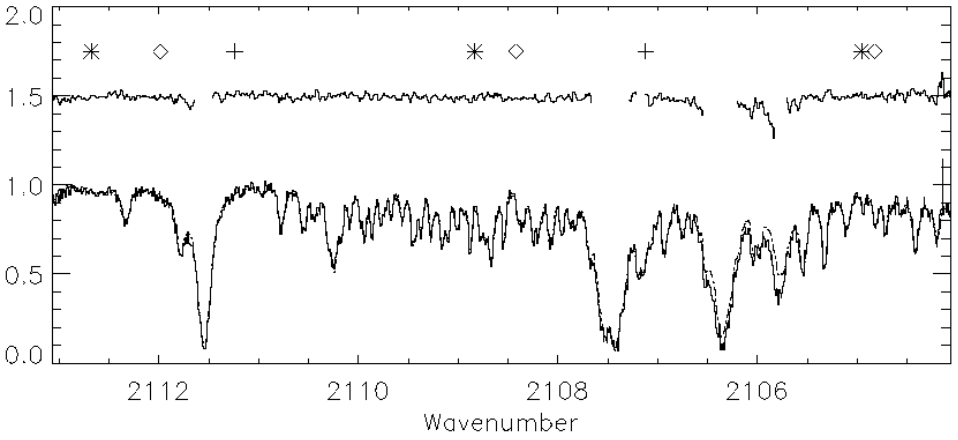

Figure 3.16 HD 38678. The science spectrum (solid line) and overplotted telluric standard HR 5671 (dot-dashed line) are shown in normalized flux. The ratio is plotted, offset by 0.5. Areas where the transmittance is less than 50% are not plotted. CO transitions are shown for v=1-0 (cross), v=2-1 (asterisks), and v=3-2 (diamonds).

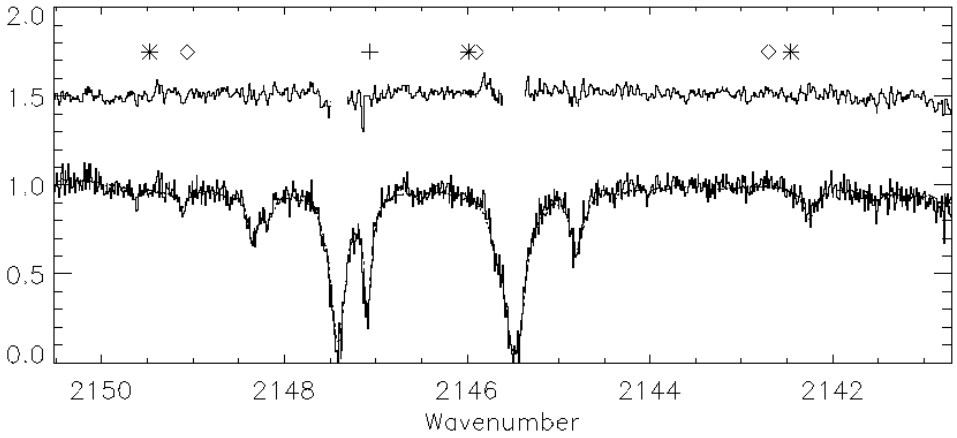

Figure 3.17 HD 49662. The science spectrum (solid line) and overplotted telluric standard HR 4798 (dot-dashed line) are shown in normalized flux. The ratio is plotted, offset by 0.5. Areas where the transmittance is less than 50% are not plotted. The broad Pfund Beta feature is not seen. CO transitions are shown for v=1-0 (cross), v=2-1 (asterisks), and v=3-2 (diamonds).

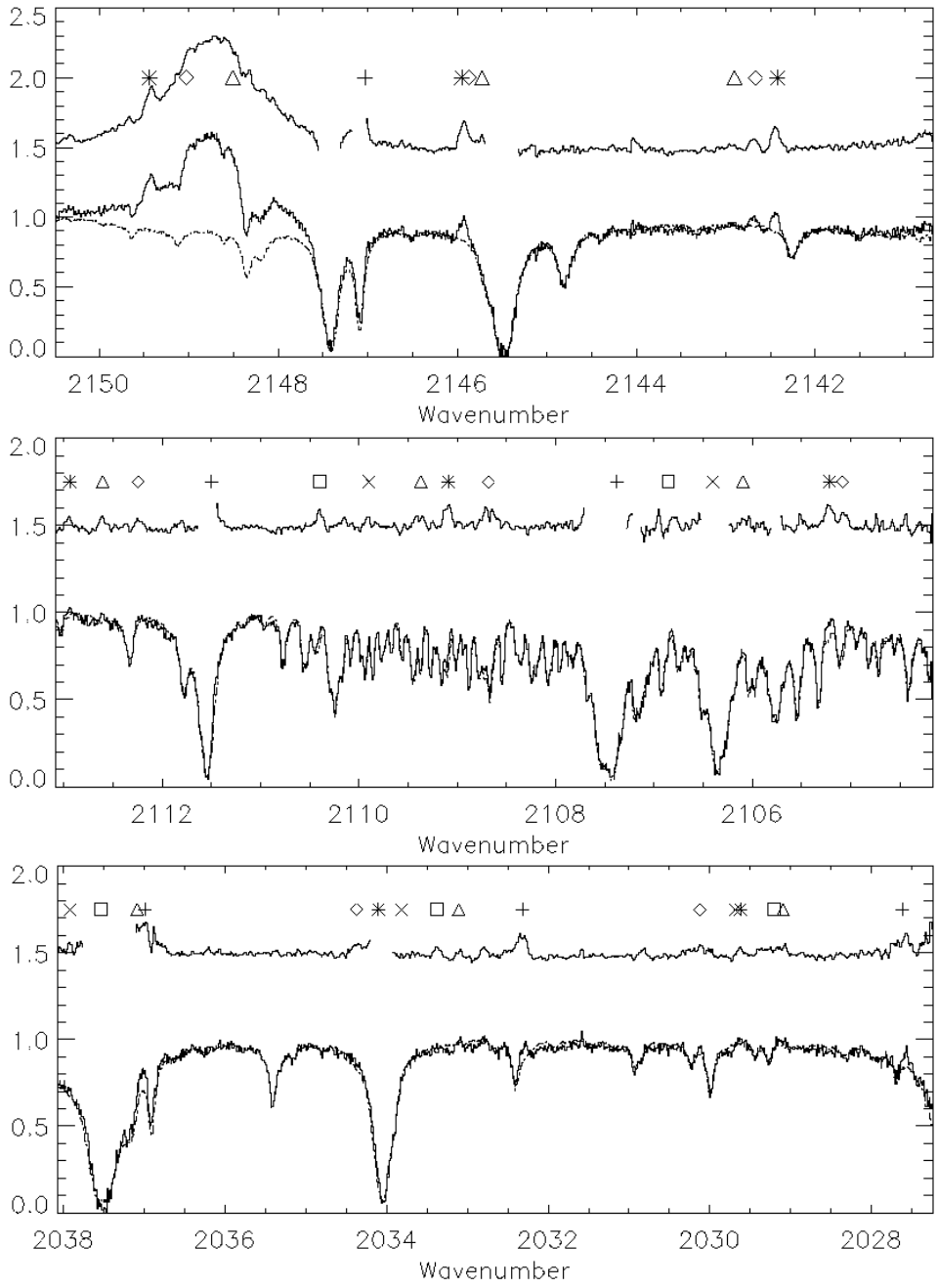

Figure 3.18 HD 97048. The science spectrum (solid line) and overplotted telluric standards (dot-dashed line) are shown in normalized flux. The standards used are HR 4798, HR 5671, and Zeta Ori, for the 2147, 2109, and 2032 settings, respectively. The ratio is plotted, offset by 0.5. Areas where the transmittance is less than 50% are not plotted. The broad Pfund Beta feature is seen, centered around 2149 cm^{-1}. Transitions are shown for ^{12}CO: v=1-0 (cross), v=2-1 (asterisks), v=3-2 (diamonds), and v=4-3 (triangles), ^{13}CO ('X's), and $C^{18}O$ (squares).

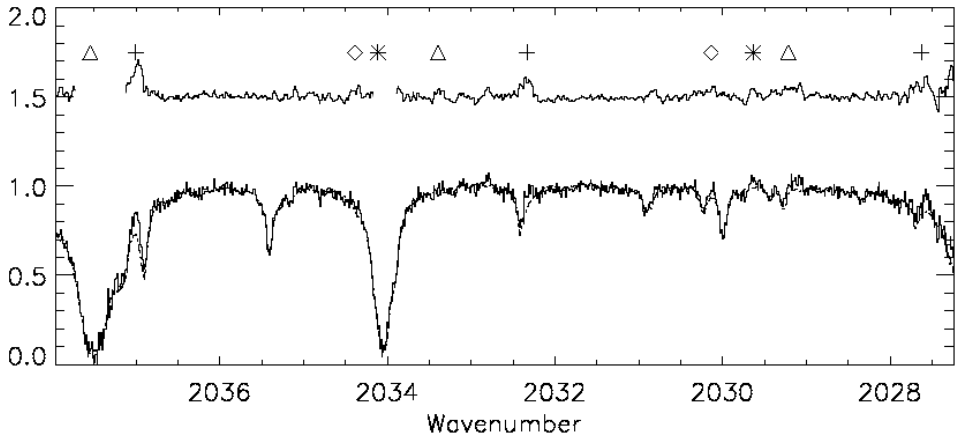

Figure 3.19 HD 98922. The science spectrum (solid line) and overplotted telluric standard Zeta Ori (dot-dashed line) are shown in normalized flux. The ratio is plotted, offset by 0.5. Areas where the transmittance is less than 50% are not plotted. Transitions for ^{12}CO are shown for v=1-0 (cross), v=2-1 (asterisks), and v=3-2 (diamonds), as well as the the ^{13}CO, v=1-0 transition (triangles).

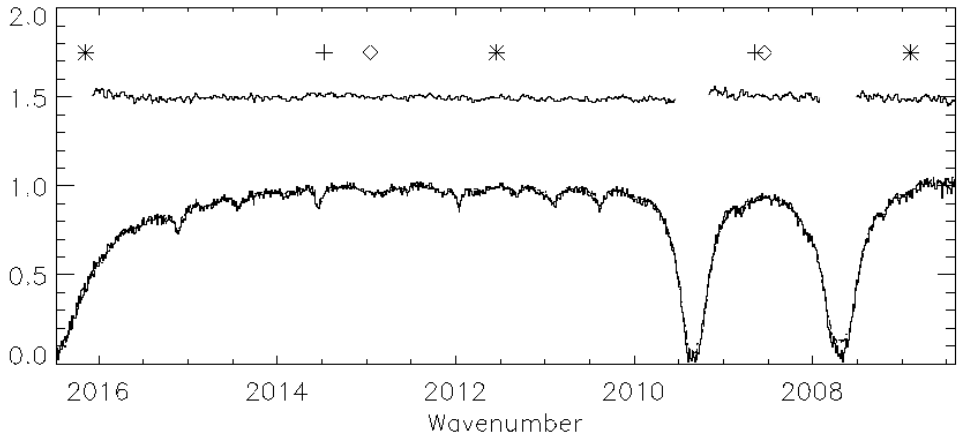

Figure 3.20 HD 100453. The science spectrum (solid line) and overplotted telluric standard HR 5671 (dot-dashed line) are shown in normalized flux. The ratio is plotted, offset by 0.5. Areas where the transmittance is less than 50% are not plotted. CO transitions are shown for v=1-0 (cross), v=2-1 (asterisks), and v=3-2 (diamonds). No emission is observed, including the P(30) line at $\sim$ 2013.5 cm^{-1}.

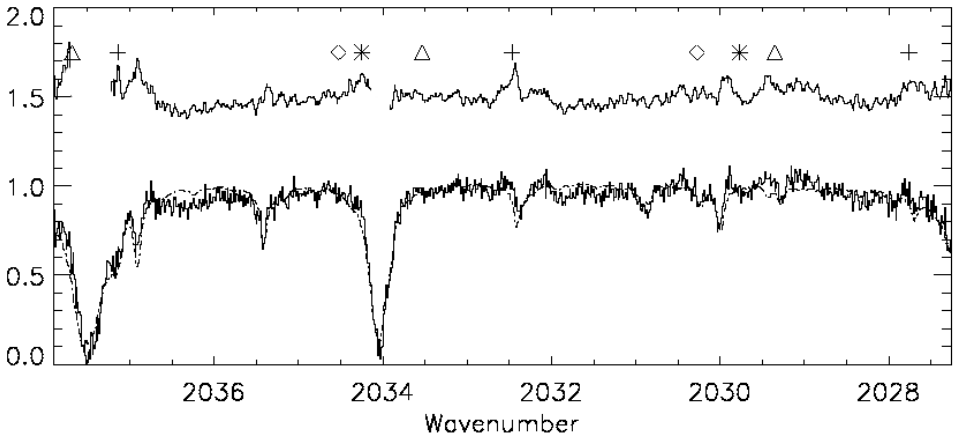

Figure 3.21 HD 101412. The science spectrum (solid line) and overplotted telluric standard Zeta Ori (dot-dashed line) are shown in normalized flux. The ratio is plotted, offset by 0.5. Areas where the transmittance is less than 50% are not plotted. Transitions for ^{12}CO are shown for v=1-0 (cross), v=2-1 (asterisks), and v=3-2 (diamonds), as well as the the ^{13}CO, v=1-0 transition (triangles).

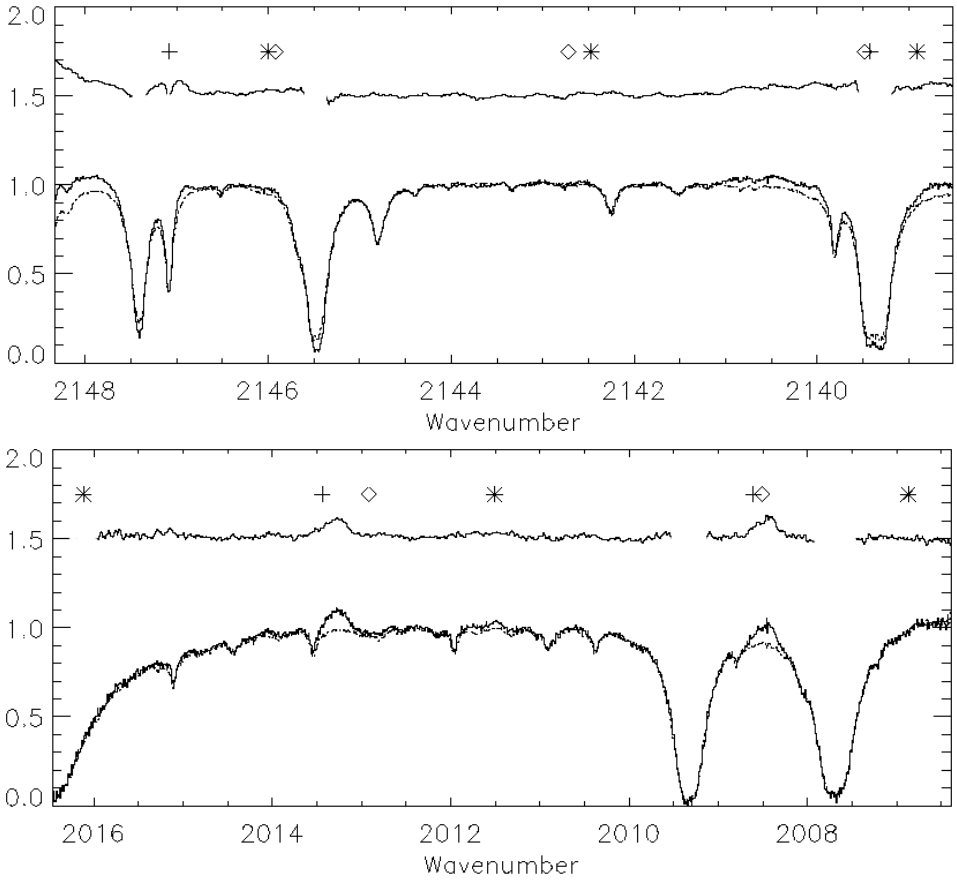

Figure 3.22 HD 104237. Shown in normalized flux are the science spectrum (solid line) and overplotted telluric standards HR 2618 and HR 5671 for the 2143 and 2012 settings, respectively (dot-dashed line). The ratio is plotted, offset by 0.5. Areas where the transmittance is less than 50% are not plotted. The broad Pfund Beta feature is seen, centered around 2149 cm^{-1}. CO transitions are shown for v=1-0 (cross), v=2-1 (asterisks), and v=3-2 (diamonds).

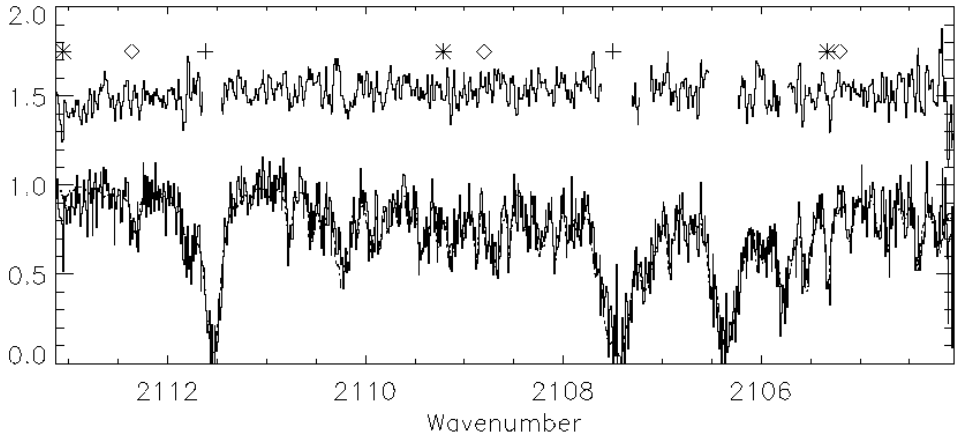

Figure 3.23 HD 121847. The science spectrum (solid line) and overplotted telluric standard HR 5671 (dot-dashed line) are shown in normalized flux. The ratio is plotted, offset by 0.5. Areas where the transmittance is less than 50% are not plotted. CO transitions are shown for v=1-0 (cross), v=2-1 (asterisks), and v=3-2 (diamonds). No features are observed, yet there is a large amount of noise in this spectrum.

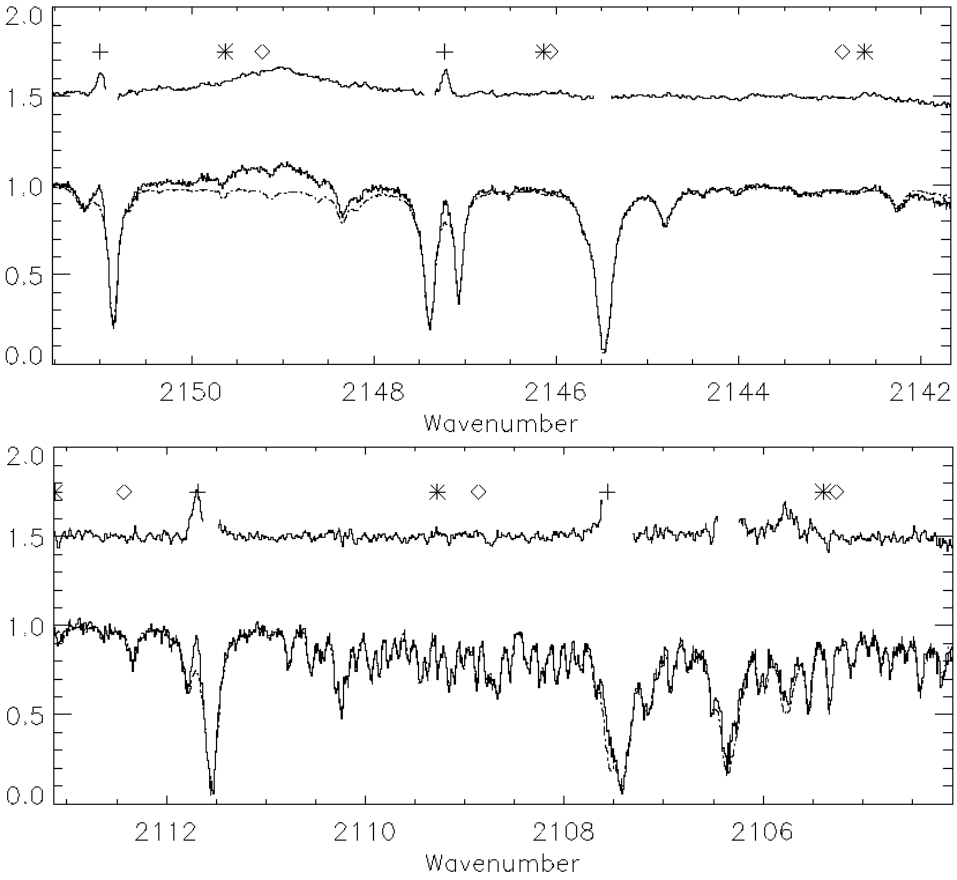

Figure 3.24 HD 135344b (SAO 206462). Shown in normalized flux are the science spectrum (solid line) and overplotted telluric standards HR 7121 and HR 5671 for the 2146 and 2109 settings, respectively (dot-dashed line). The ratio is plotted, offset by 0.5. Areas where the transmittance is less than 50% are not plotted. The broad Pfund Beta feature is seen, centered around 2149 cm^{-1}. CO transitions are shown for v=1-0 (cross), v=2-1 (asterisks), and v=3-2 (diamonds).

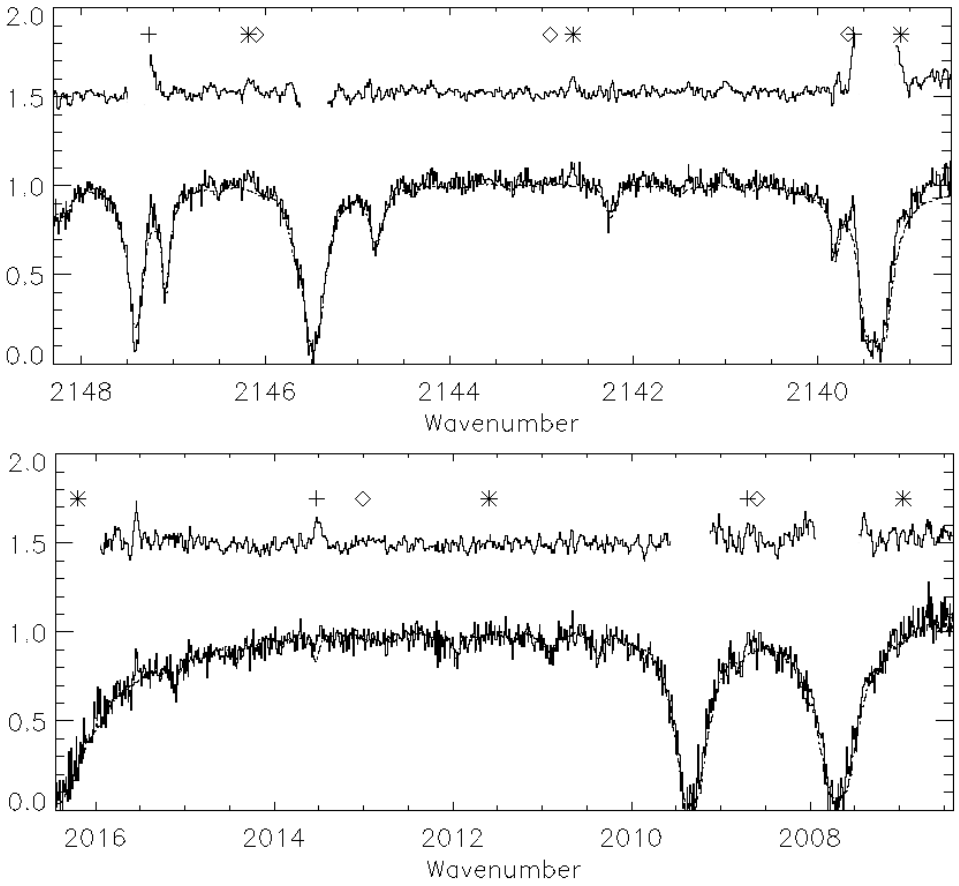

Figure 3.25 HD 139614. Shown in normalized flux are the science spectrum (solid line) and overplotted telluric standards HR 2618 and HR 5671 for the 2146 and 2010 settings, respectively (dot-dashed line). The ratio is plotted, offset by 0.5. Areas where the transmittance is less than 50% are not plotted. The broad Pfund Beta feature is not seen around 2149 cm^{-1}. CO transitions are shown for v=1-0 (cross), v=2-1 (asterisks), and v=3-2 (diamonds).

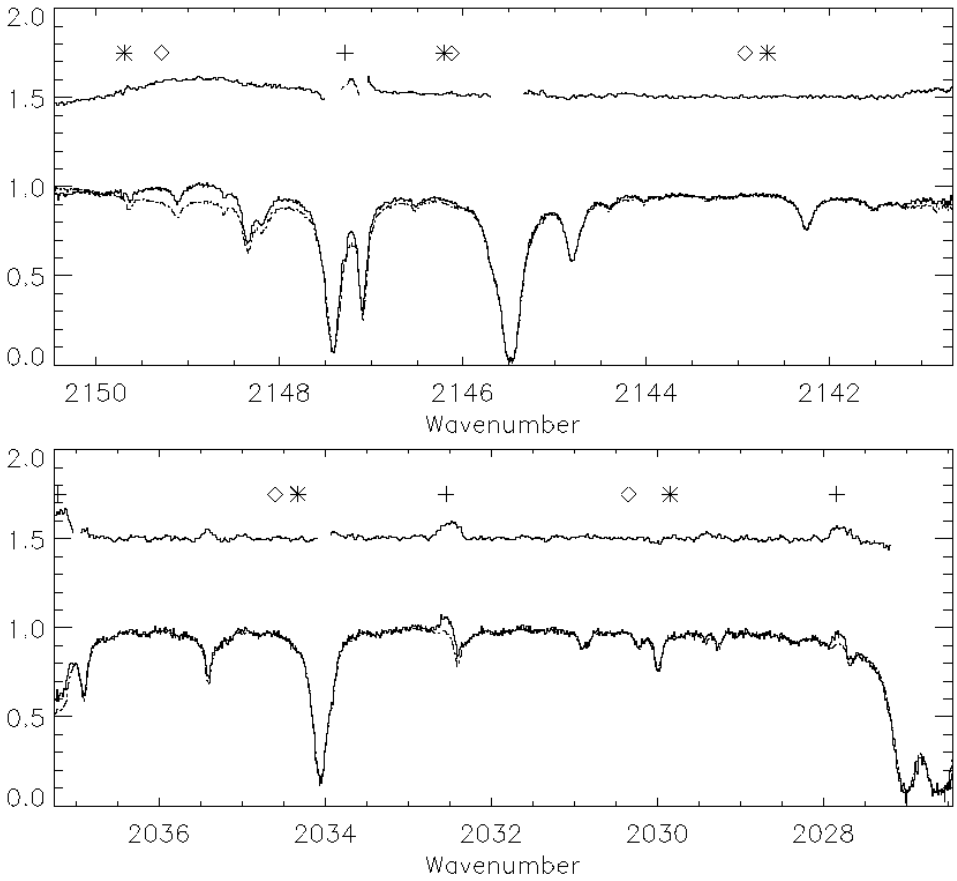

Figure 3.26 HD 142527. Shown in normalized flux are the science spectrum (solid line) and overplotted telluric standards HR 7121 and HR 4798 for the 2146 and 2032 settings, respectively (dot-dashed line). The ratio is plotted, offset by 0.5. Areas where the transmittance is less than 50% are not plotted. The broad Pfund Beta feature is seen, centered around 2149 cm^{-1}. CO transitions are shown for v=1-0 (cross), v=2-1 (asterisks), and v=3-2 (diamonds).

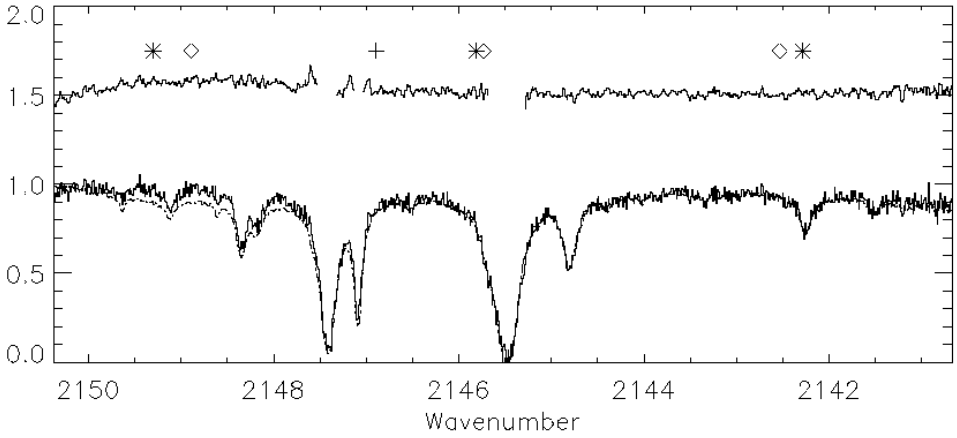

Figure 3.27 HD 142666. The science spectrum (solid line) and overplotted telluric standard HR 4798 (dot-dashed line) are shown in normalized flux. The ratio is plotted, offset by 0.5. Areas where the transmittance is less than 50% are not plotted. The broad Pfund Beta feature is seen, centered around 2149 cm^{-1}. CO transitions are shown for v=1-0 (cross), v=2-1 (asterisks), and v=3-2 (diamonds). No emission is observed, including the R(0) line at $\sim$ 2147 cm^{-1}.

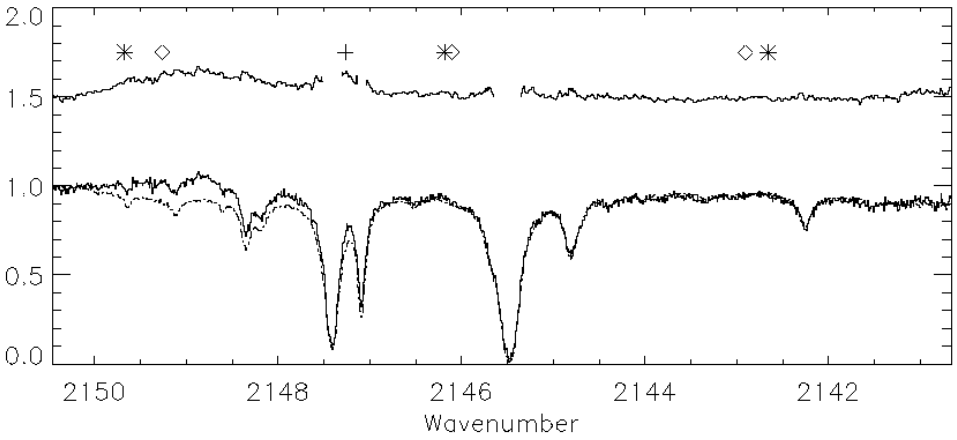

Figure 3.28 HD 144432. The science spectrum (solid line) and overplotted telluric standard HR 4798 (dot-dashed line) are shown in normalized flux. The ratio is plotted, offset by 0.5. Areas where the transmittance is less than 50% are not plotted. The broad Pfund Beta feature is seen, centered around 2149 cm^{-1}. CO transitions are shown for v=1-0 (cross), v=2-1 (asterisks), and v=3-2 (diamonds). Emission is observed from the R(0) line at $\sim$ 2147 cm^{-1}.

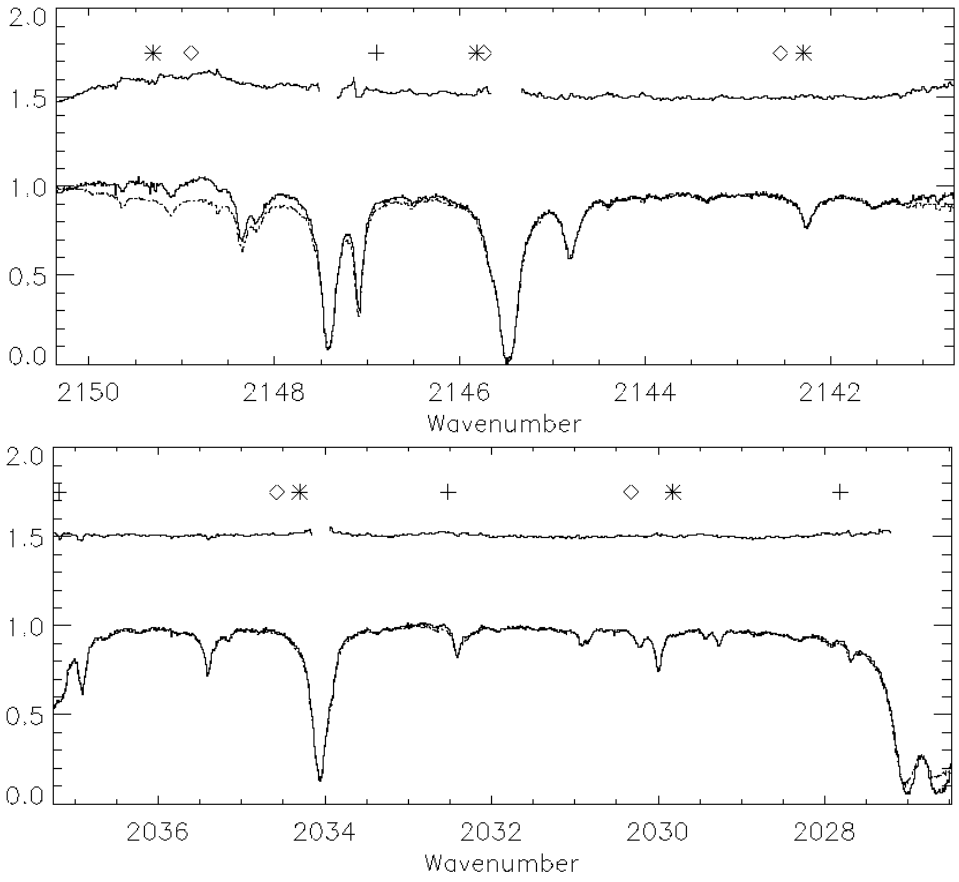

Figure 3.29 HD 144668. Shown in normalized flux are the science spectrum (solid line) and overplotted telluric standards HR 4798 and HR 5671 for the 2146 and 2032 settings, respectively (dot-dashed line). The ratio is plotted, offset by 0.5. Areas where the transmittance is less than 50% are not plotted. The broad Pfund Beta feature is seen, centered around 2149 cm^{-1}. CO transitions are shown for v=1-0 (cross), v=2-1 (asterisks), and v=3-2 (diamonds). No emission is observed from either the high-J or low-J lines, including the R(0) line at $\sim$ 2147 cm^{-1} and P(26) line at $\sim$ 2032 cm^{-1}.

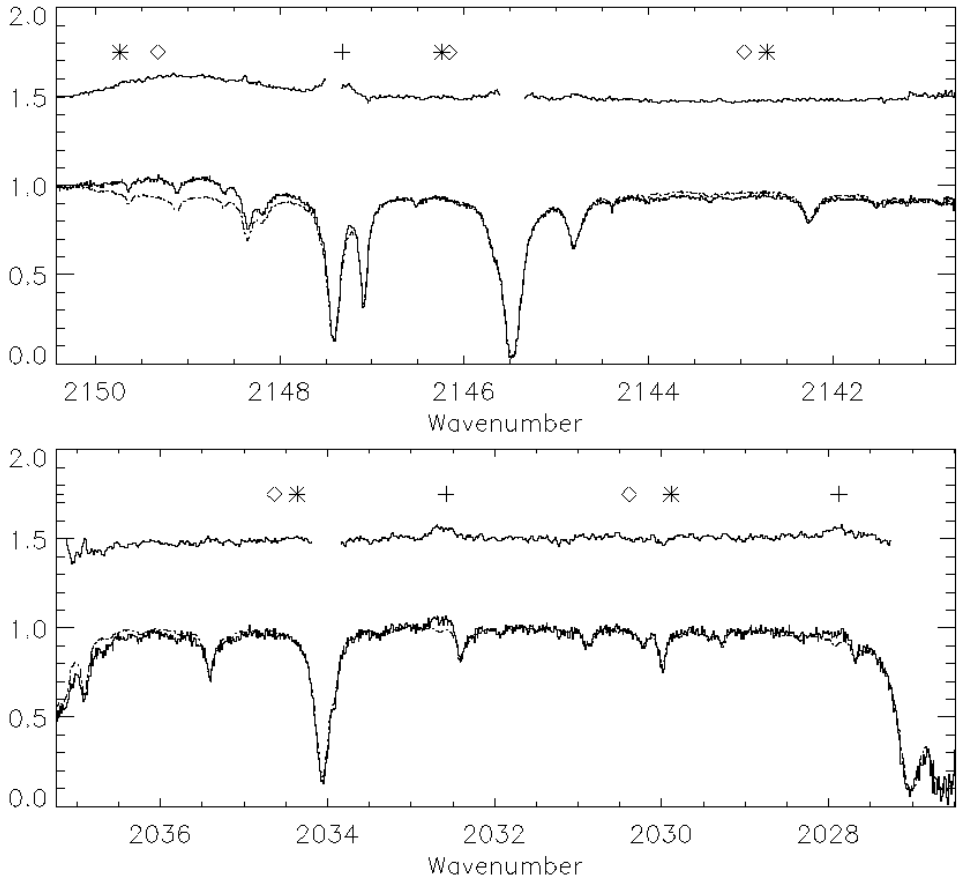

Figure 3.30 HD 150193. Shown in normalized flux are the science spectrum (solid line) and overplotted telluric standards HR 4798 and HR 7121 for the 2146 and 2032 settings, respectively (dot-dashed line). The ratio is plotted, offset by 0.5. Areas where the transmittance is less than 50% are not plotted. The broad Pfund Beta feature is seen, centered around 2149 cm^{-1}. CO transitions are shown for v=1-0 (cross), v=2-1 (asterisks), and v=3-2 (diamonds). Emission is observed from both the high-J and low-J lines, including the R(0) line at $\sim$ 2147 cm^{-1} and P(26) line at $\sim$ 2032 cm^{-1}.

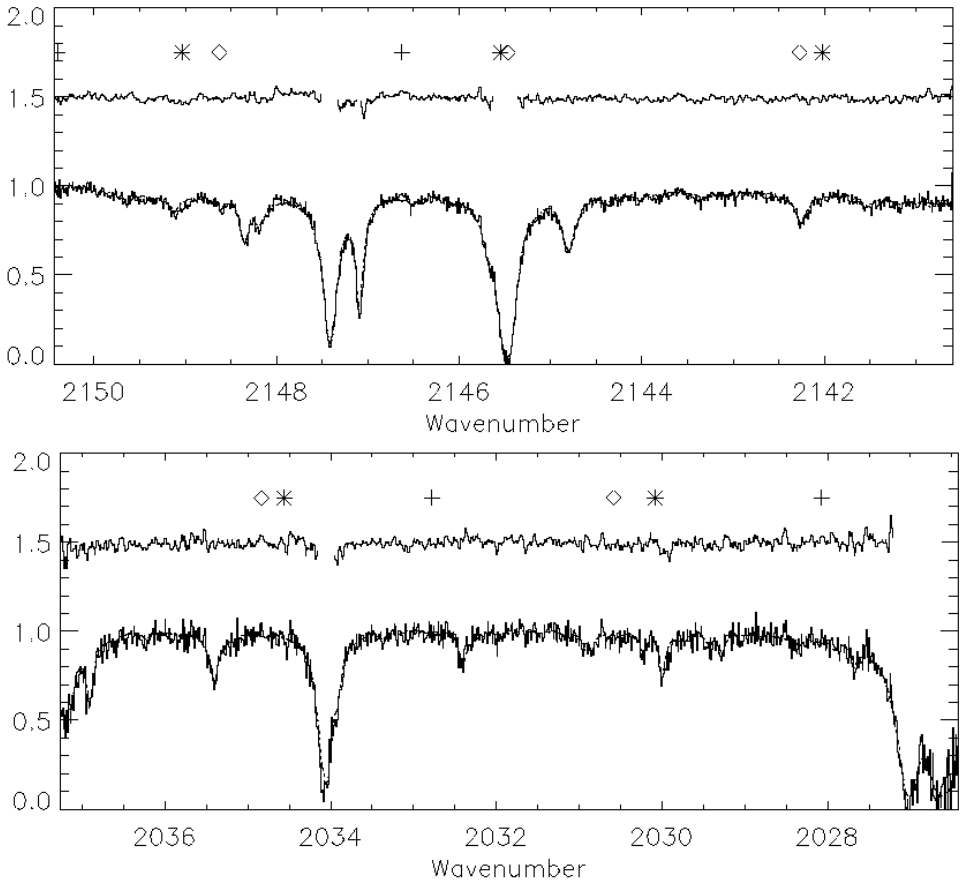

Figure 3.31 HD 158352. Shown in normalized flux are the science spectrum (solid line) and overplotted telluric standards HR 4798 and HR 7121 for the 2146 and 2032 settings, respectively (dot-dashed line). The ratio is plotted, offset by 0.5. Areas where the transmittance is less than 50% are not plotted. The broad Pfund Beta feature is seen, centered around 2149 cm^{-1}. CO transitions are shown for v=1-0 (cross), v=2-1 (asterisks), and v=3-2 (diamonds). No emission is observed from either the high-J or low-J lines, including the R(0) line at $\sim$ 2146.5 cm^{-1} and P(26) line at $\sim$ 2032.5 cm^{-1}.

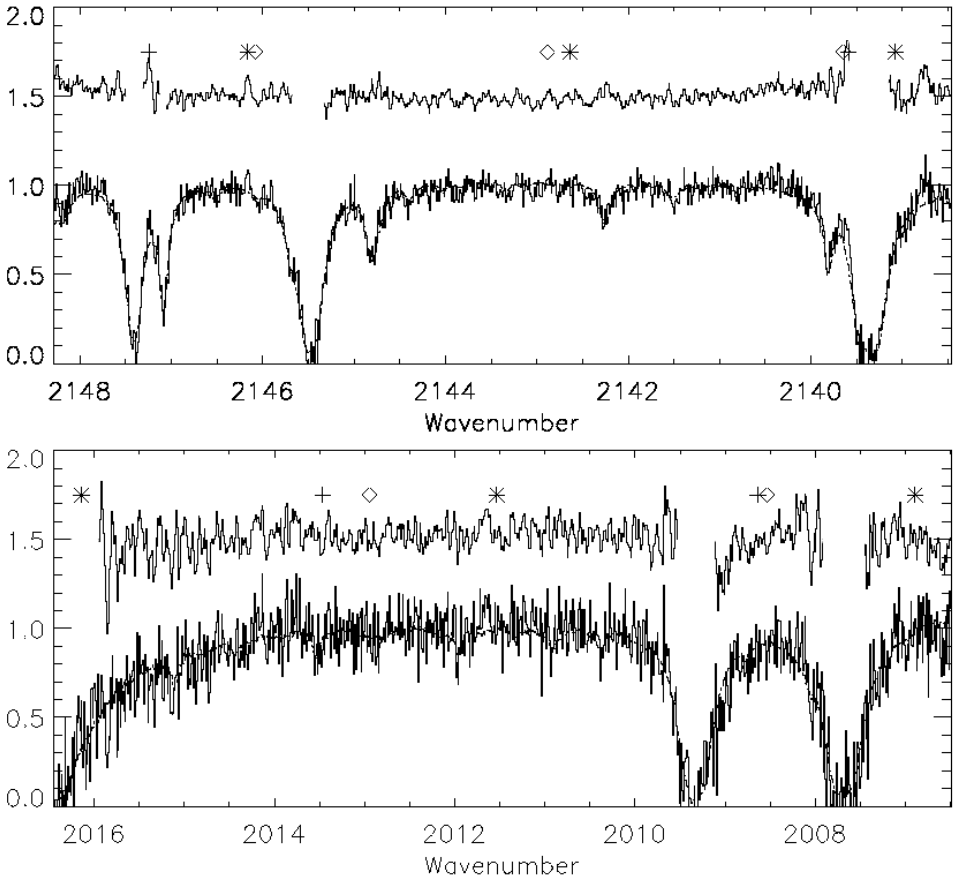

Figure 3.32 HD 169142. Shown in normalized flux are the science spectrum (solid line) and overplotted telluric standards HR 2618 and HR 5671 for the 2146 and 2010 settings, respectively (dot-dashed line). The ratio is plotted, offset by 0.5. Areas where the transmittance is less than 50% are not plotted. The broad Pfund Beta feature is seen, centered around 2149 cm^{-1}. CO transitions are shown for v=1-0 (cross), v=2-1 (asterisks), and v=3-2 (diamonds).

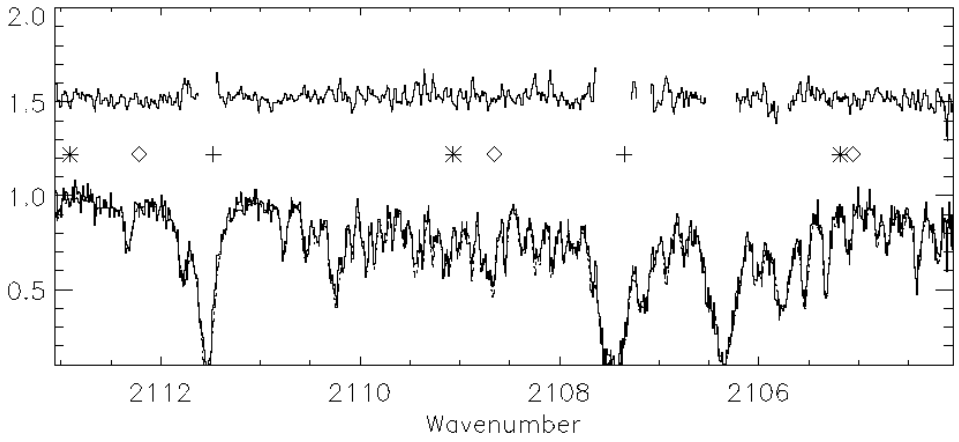

Figure 3.33 HR 4796A. The science spectrum (solid line) and overplotted telluric standard HR 5671 (dot-dashed line) are shown in normalized flux. The ratio is plotted, offset by 0.5. Areas where the transmittance is less than 50% are not plotted. CO transitions are shown for v=1-0 (cross), v=2-1 (asterisks), and v=3-2 (diamonds). No emission is observed, including the P(8) line at $\sim$ 2111.5 cm^{-1}. ***Low J from najita 2002?***

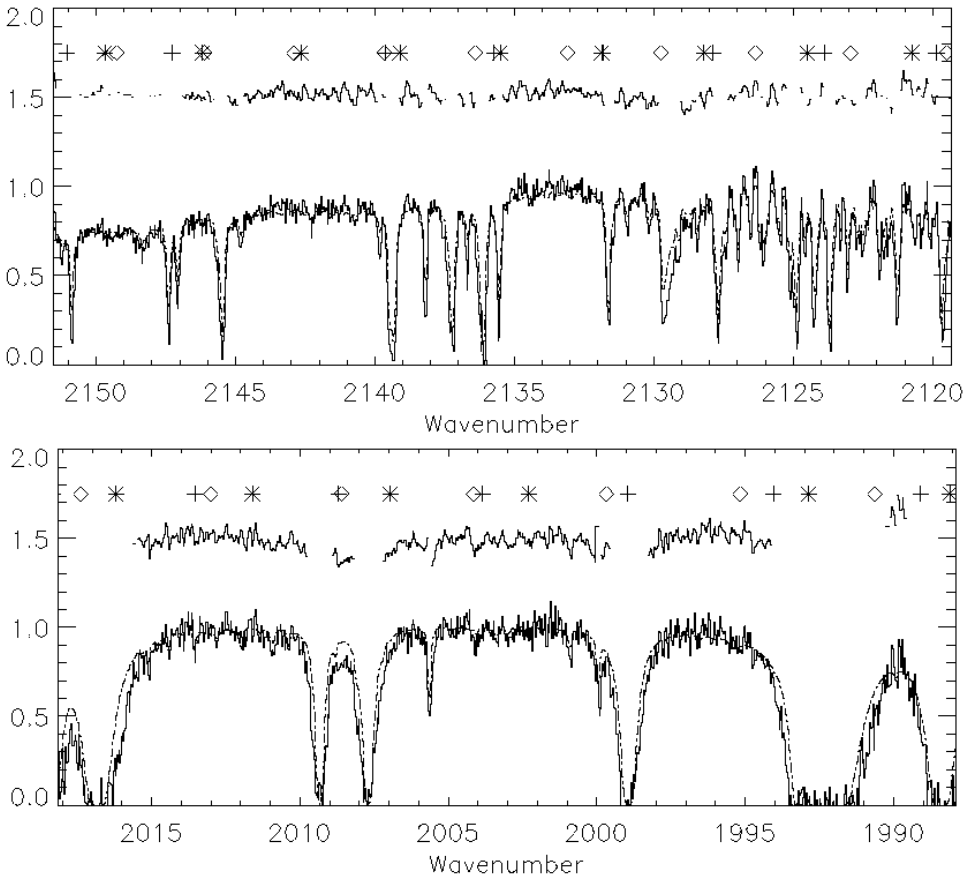

Figure 3.34 49 Ceti. The science spectrum (solid line) and overplotted telluric standard HR 8518 (dot-dashed line) are shown in normalized flux. The ratio is plotted, offset by 0.5. Areas where the transmittance is less than 50% are not plotted. The broad Pfund Beta feature is seen, centered around 2149 cm^{-1}. CO transitions are shown for v=1-0 (cross), v=2-1 (asterisks), and v=3-2 (diamonds). ***FIT model better***

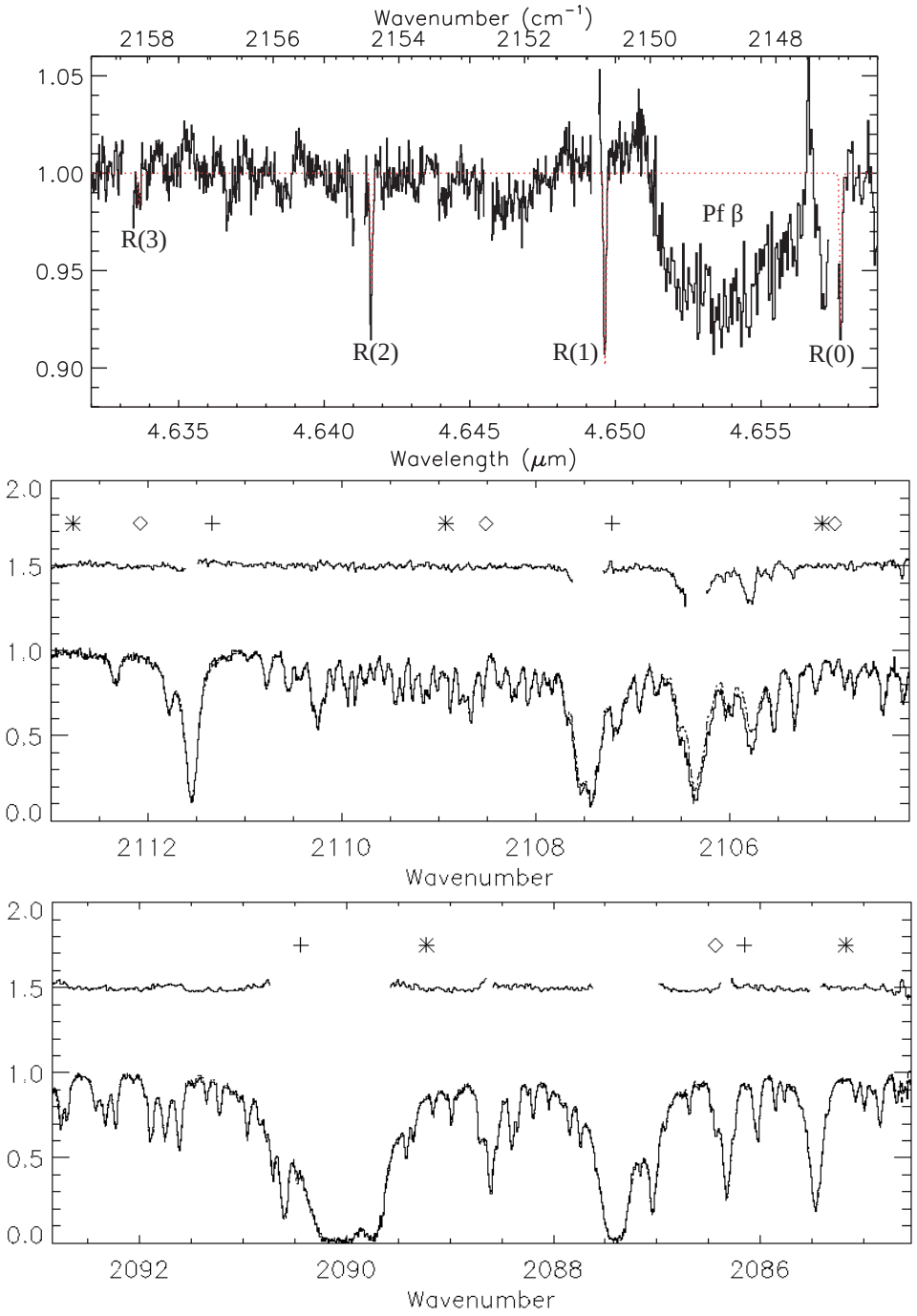

Figure 3.35 β Pictoris shown with detected absorption in top panel. Lower panels show the science spectrum (solid line) and overplotted telluric standards HR 5671 and Zeta Ori for the 2109 and 2090 settings, respectively (dot-dashed line). The ratio is plotted, offset by 0.5. Areas where the transmittance is less than 50% are not plotted. CO transitions are shown for v=1-0 (cross), v=2-1 (asterisks), and v=3-2 (diamonds). Absorption is observed (discussed in previous chapter). No emission is observed in the higher settings, including the P(8) line at ~ 2111.5 cm^{-1}.

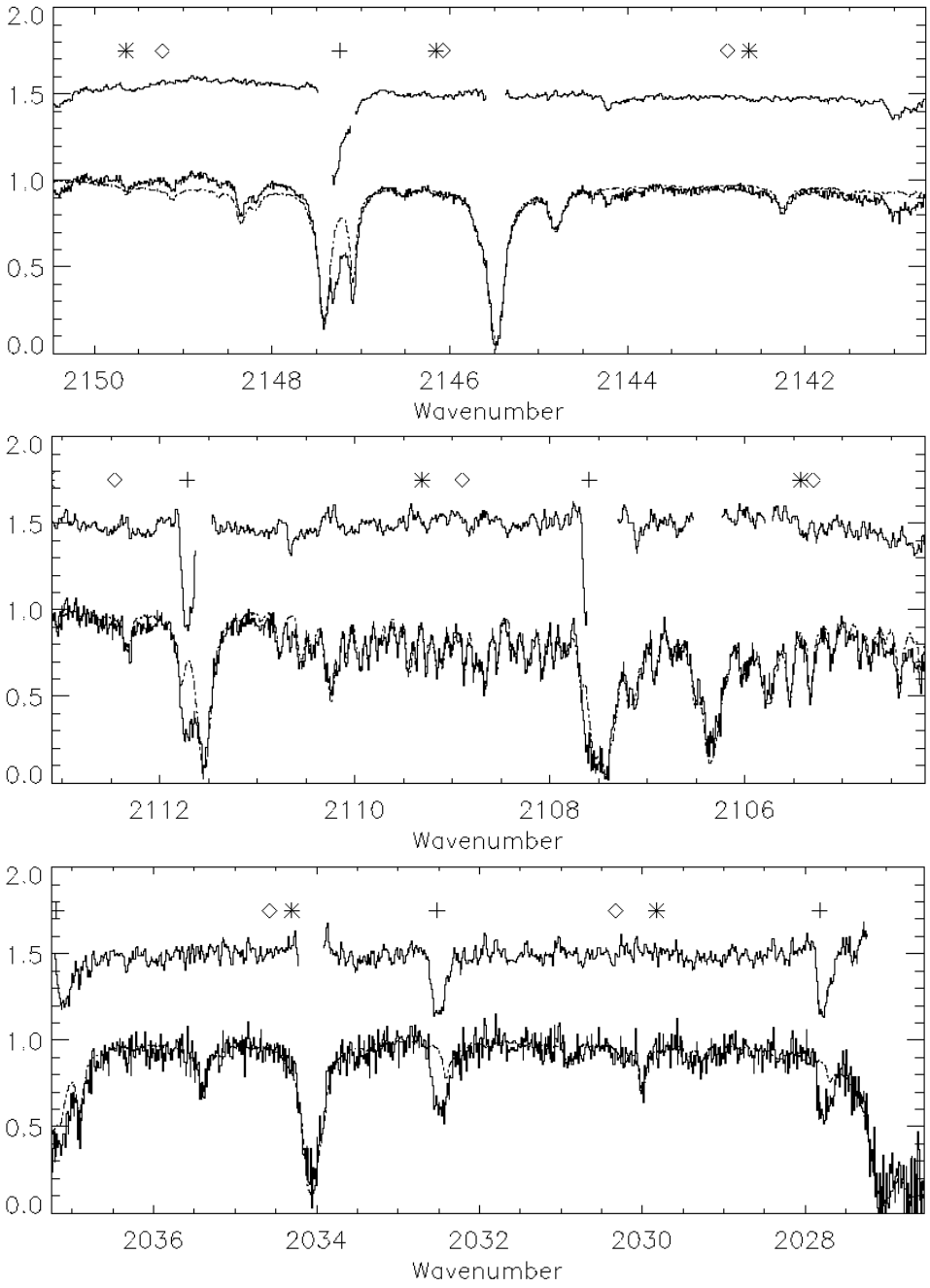

Figure 3.36 PDS 144N. Shown in normalized flux are the science spectrum (solid line) and overplotted telluric standards HR 4798, HR 5671, and again HR 5671 for the 2146, 2109, and 2032 settings, respectively (dot-dashed line). The ratio is plotted, offset by 0.5. Areas where the transmittance is less than 50% are not plotted. The broad Pfund Beta feature is seen, centered around 2149 cm^{-1}. CO transitions are shown for v=1-0 (cross), v=2-1 (asterisks), and v=3-2 (diamonds). Absorption is observed from both the high-J and low-J lines, including the R(0) line at $\sim$ 2147 cm^{-1} and P(26) line at $\sim$ 2032.5 cm^{-1}.

3.6 Object Data Summary and References

3.6.0.1 CO Ori

An F7V star (Mora et al., 2001). Estimated to be at the distance to the Orion cluster, $\sim$ 400 pc. Age of $3.3 \pm 0.4 Myrs$ (Calvet et al., 2004). Has a K-L of 1.09 (Glass & Penston, 1974). Classified as a group II source with no detectable PAH features(Acke & van den Ancker, 2006b).

3.6.0.2 GW Ori

Classified as a G5 star (Gullbring et al., 2000). At a distance of 308^{+245}_{-95} pc (Bertout et al., 1999). No PAHs emission observed (Przygodda et al., 2003). Has a K-l of 1.07(Mendoza, 1967). Age of 1 Myr (Calvet et al., 2004). Group Ia source based on SED.

3.6.0.3 T Ori

An A3IV star (Mora et al., 2001). Estimated to be at the distance 460 pc (Hillenbrand et al., 1992). Has a K-L magnitude of 1.17 (Kilkenny et al., 1985). Has no detected PAH emission (Acke & van den Ancker, 2006b). Classified as a group II source by Acke & van den Ancker (2006b). Age estimated to be either 3.89 or 1.68 Myr, depending on the extinction (Hernández et al., 2004). For analysis, we use an intermediate value of 2.8 Myr.

3.6.0.4 V380 Ori

An A1 star at a distance of 510 pc, identified as a group II source (van Boekel et al., 2005). Has a K-L magnitude of 1.59 (Strom et al., 1990). Has no detected PAH emission (Acke & van den Ancker, 2006b). Estimated to be an age of 7.4 Myr (Blondel & Djie, 2006). Has a Br γ luminosity of 3.9×10^{31} erg s^{-1} (Donehew et al., 2010).

3.6.0.5 HD 37357

An A2V star at a distance of 240 pc, identified as a group II source (van Boekel et al., 2005). Has a K-L of 0.91 (Malfait et al., 1998). Has no detected PAH emission (Acke & van den Ancker, 2006b). Estimated to be an age of 10 Myr (Blondel & Djie, 2006).

3.6.0.6 HD 37806

An A2V star at a distance of 470 pc, identified as a group II source, and estimated to be at an age of 0.8 Myr based on evolutionary tracks (van Boekel et al., 2005). Has a K-L of 1.54 (Malfait et al., 1998). Has no detected PAH emission (Acke & van den Ancker, 2006b). Has a Br γ luminosity of $> 7.3 \times 10^{30}$ erg s^{-1} (Donehew et al., 2010).

3.6.0.7 HD 38678 (ζ Lep)

An A2V star at a distance of 21.5 pc (Perryman et al., 1997). Estimated age of 231 Myr (Song et al., 2001). Has a K-L of 0.2 and a group II source from IRAF (Fajardo-Acosta et al., 1998).

3.6.0.8 HD 49662

Distance of 188 pc (Sylvester et al., 1996). Has a K-L of -0.2 with an infrared fractional excess of 1.1×10^{-3} (Sylvester et al., 1996). A group Ib source as seen in the SED presented by Kalas et al. (2002).

3.6.0.9 HD 97048

A B9.5V star (Whittet et al., 1987) at a distance of 180 pc (van den Ancker et al., 1998). Estimated to be an age of $\sim$ 3 Myr(Lagage et al., 2006). Specified as a group Ib source (van Boekel et al., 2005). Identified to have strong PAH emission and an $A_V = 1.26$ by Acke & van den Ancker (2004). K-L magnitude is 1.43 (Kilkenny et al., 1985). Has a Br γ equivalent width of -8.4Å(Garcia Lopez et al., 2006).

3.6.0.10 HD 98922

A B9Ve star (van den Ancker et al., 1998). Has a K-L of 1.61 (Malfait et al., 1998). Considered a group II source with strong PAH emission radially extending $\leq$ 130 AU(Geers et al., 2007). The star is 2.6 Myrs old at a distance of 203 pc (Blondel & Djie, 2006). Has a Br γ equivalent width of -3.7Å(Garcia Lopez et al., 2006).

3.6.0.11 HD 100453

A spectral class A9V star 111 parsecs away, estimated to be 10 Myrs old based on evolutionary tracks (van Boekel et al., 2005). A Group Ib star with moderately strong PAH lines and no silicate emission lines (Meeus et al., 2001). Has a K-L of 1.32 (Malfait et al., 1998), with an extinction $A_V = 0$ (Garcia Lopez et al., 2006). Has a Br γ equivalent width of -1.5Å(Garcia Lopez et al., 2006).

3.6.0.12 HD 101412

A 9.5V star identified as a group II source by van Boekel et al. (2005). K-L magnitude is 1.41 (van Boekel et al., 2005). Has strong PAH emission, radially extending ≤ 38 AU (Geers et al., 2007). Estimated to be an age of 2 Myrs (Wade et al., 2007). Distance between 500 and 700 pc away (Corradi et al., 1997). We will use 600 pc for this analysis.

3.6.0.13 HD 104237

An A4IV, identified as a group II source (van Boekel et al., 2005). Determined to be at a distance of 116 pc (van den Ancker, 1999). Has a K-L of 1.37 (Malfait et al., 1998). Identified as a group II source with no PAH emission and an $A_V = 0.29$ (Acke & van den Ancker, 2004). Estimated to be an age of 4.8 Myr (Blondel & Djie, 2006). Has a Br γ equivalent width of -6.7Å(Garcia Lopez et al., 2006).

3.6.0.14 HD 121847

A B8V star at a distance of 104 pc (Dent et al., 2005). Has a K-L of -0.05 (Dougherty et al., 1991).

3.6.0.15 HD 135344b (SAO 206462)

A group Ib source (Meeus et al., 2001), with moderate PAH features (Sloan et al., 2005; Geers et al., 2006). Has a K-L of 0.48 (Malfait et al., 1998). The distance and age are debated, but for this paper, we use the most recent values of $d = 140$ pc and an age of 8 Myr (van Boekel et al., 2005). Has a Br γ equivalent width of -1.3Å(Garcia Lopez et al., 2006).

3.6.0.16 HD 139614

An A7V star, with a K-L of 1.08 (Malfait et al., 1998). At a distance of 140 pc, HD 139614 has been identified as a group Ia source, and estimated to be at an age of > 10 Myr based on evolutionary tracks (van Boekel et al., 2005). Has a Br γ equivalent width of -3.0Å(Garcia Lopez et al., 2006).

3.6.0.17 HD 142527

An F6III star, with a K-L excess of 1.31(Malfait et al., 1998). Estimated to be 200pc away (van den Ancker et al., 1998). Classified as a group Ia source with moderate PAH features by Meeus et al. (2001). Based on evolutionary tracks, estimated to be at an age of 1 Myr (van Boekel et al., 2005). Has a Br γ equivalent width of -1.2Å(Garcia Lopez et al., 2006).

3.6.0.18 HD 142666

An A8V star with a K-L of 1.07 (Malfait et al., 1998). Determined to be at a distance of 116 pc by van den Ancker (1999). Classified as a group II source with moderate PAH emission by Meeus et al. (2001). Estimated to be an age of 4.4 Myr (Blondel & Djie, 2006). Has a Br γ luminosity of 7.2×10^{29} erg s^{-1} (Donehew et al., 2010).

3.6.0.19 HD 144432

An A9V star (Dunkin et al., 1997). Has a K-L of 1.00 (Malfait et al., 1998). Identified as a group II source with no PAH features (Meeus et al., 2001). Estimated to be an age of 6.65 Myr (Blondel & Djie, 2006).. Finding a distance estimate is problematic, as the literature reveals reasonable distances between 100-300 pc. Pérez et al. (2004) point out that depending on the star's spectral type, the distance may be between 124 and 216 pc, for an A9V or A9III star, respectively. As the star is in the same part part of the sky as Sco OB-2-2 (at 145 pc), we will assume the smaller distance of 124 pc. Has a Br γ flux of 2.7×10^{30} erg s^{-1} (Donehew et al., 2010).

3.6.0.20 HD 144668

An A7 star with a K-L of 1.06 (Malfait et al., 1998). HD 144668 is at a distance of 207 pc, identified as a group II source, and estimated to be at an age of 0.5 Myr based on evolutionary tracks (van Boekel et al., 2005). No detectable PAH emission Acke & van den Ancker (2004). Has a Br γ equivalent width of -6.5Å(Garcia Lopez et al., 2006).

3.6.0.21 HD 150193

An A2IV star (van Boekel et al., 2005). HD 150193 has a K-L magnitude of 1.27 (Malfait et al., 1998). At a distance of 150 pc (van den Ancker et al., 1997), HD 150193 is identified as a group II source with no PAH features Meeus et al. (2001). Mannings & Sargent (1997) have measured the dust mass to be 0.01 $M_{\odot}$, using submillimeter observations. Estimated to be an age of 2.6 Myr (Blondel & Djie, 2006).

3.6.0.22 HD 158352

An A8V star at a distance of 63 pc (Mora et al., 2001) . Estimated age from H-R diagram is 750 Myr (Moór et al., 2006). The K-L magnitude is 0.93 (Malfait et al., 1998). Has a fractional excess of 1.8×10^{-4} at an age of 750 Myr (Moór et al., 2006). Group Ib source from SED presented in Roberge & Weinberger (2008), with a fractional excess of 9.29×10^{-5}.

3.6.0.23 HD 169142

An A5V star (Dunkin et al., 1997) at a distance of 145 pc (de Zeeuw et al., 1999). Identified as a group Ib source with moderate PAH emission and an $A_V = 0.43$ (Acke & van den Ancker, 2004). Found by Malfait et al. (1998) to have a K-L magnitude of 0.89. Based on evolutionary tracks, estimated to be 5 Myr (van Boekel et al., 2005). Has a Br γ equivalent width of -9.7Å(Garcia Lopez et al., 2006).

3.6.0.24 HR 4796A

HR 4796A is an A0V star, 67 pc away. Estimated to be at an age of 8 ± 3 Myr (Stauffer et al., 1995). A Ib source based on SED presented in (Wahhaj et al., 2005).

3.6.0.25 Beta Pic

A group II source with no PAH emission based on the SED presented in (Walker & Heinrichsen, 2000). Estimated to be an age of 20 Myr (Barrado y Navascués et al., 1999). Has a K-L of -0.2 from ISO photometry.

3.6.0.26 49 Ceti

An A4V star (Mora et al., 2001), 61 pc away (Perryman et al., 1997). The inner dust radius is 60 AU (Wahhaj et al., 2007) and the inner gas edge found by Hughes et al. (2008) is 40 AU. A group II source with no PAH emission based on the SED presented in (Walker & Heinrichsen, 2000). Has a fractional excess of 9.2×10^{-4} (Moór et al., 2006). Age estimated to be 8 Myr (Zuckerman & Song, 2004b). Has a K-L of -0.3 from ISO photometry.

3.6.0.27 PDS 144N

An A5V star (Vieira et al., 2003). A group Ia source with strong PAH emission that has a K-L of 1.92, and estimated to be at a distance of 1000 pc (Perrin et al., 2006).

3.6.0.28 HD 36112

Classified as a group Ia source by Grady et al. (2005b). Has a Br γ flux of 2.3×10^{30} erg s^{-1} (Donehew et al., 2010).

3.6.0.29 HD 31648

Has a Br γ flux of 3.8×10^{30} erg s^{-1} (Donehew et al., 2010).

3.6.0.30 VV Ser

Has a Br γ flux of 1.8×10^{31} erg s^{-1} (Donehew et al., 2010).

3.6.0.31 HD 31293 (AB Aur)

Disk inclination of 65° (Keller et al., 2008). Estimated to be an age of 4.8 Myr (Blondel & Djie, 2006). Has a Br γ flux of 3.8×10^{30} erg s^{-1} (Donehew et al., 2010).

3.6.0.32 HD 58647

Estimated age from HR diagram of 0.2 Myr (van den Ancker et al., 1998).

3.6.0.33 HD 141569

Estimated age of 5 Myr (Wyatt et al., 2007). Disk inclination of 51° (Keller et al., 2008).

3.6.0.34 HD 144914

Has a Br γ equivalent width of 6.9 ± 0.3 (Garcia Lopez et al., 2006). Estimated to be an age of 0.5-1.0 Myr (0.75 Myr listed in table) (Habart et al., 2003). Has a Br γ equivalent width of -0.8Å(Garcia Lopez et al., 2006).

3.6.0.35 HD 158643 (51 Oph)

Has a Br γ equivalent width of 1.3 ± 0.3 (Garcia Lopez et al., 2006).

3.6.0.36 HD 163296

Estimated to be an age of 6.0 Myr (Blondel & Djie, 2006). Has a Br γ equivalent width of -4.7 ± 0.1 (Garcia Lopez et al., 2006). Has a Br γ flux of 1.1×10^{31} erg s^{-1} (Donehew et al., 2010).

3.6.0.37 HD 250550

Classified as a group Ib source with no PAH features (Acke & van den Ancker, 2006b). Estimated to be 1 Myr. Has a Br γ flux of 3.4×10^{31} erg s^{-1} (Donehew et al., 2010).

3.6.0.38 HD 259431

Age estimated to be either 0.32 or 0.09 Myr, depending on the extinction (Hernández et al., 2004). For this we use an intermediate value of 0.2 Myr. A group Ia source based on the SED, with moderate PAH emission (Kraus et al., 2008). Has a Br γ flux of 9.6×10^{31} erg s^{-1} (Donehew et al., 2010).

CHAPTER 4

SPECTRO-ASTROMETRY

4.1 Spectro-astrometry Model

We model both the flux and spectro-astrometric signal. We take the fluorescent model from Brittain et al. (2009) as an input to the spectro-astrometric model. The fluorescent model produces flux as a function of radius, which is then converted into flux as a function of position on the sky. The spectro-astrometric signal is calculated using the same formula as mentioned earlier, without the dilution correction. The codes to create the spectro-astrometric model are presented in the Appendix.

4.2 Spectro-astrometry of HD 100546

Much is unknown about the specifics of how planets form, evidenced especially with the recently detected planets in debris disks (e.g. β Pictoris; Lagrange et al., 2009). However, to date there has still not been a planet detected that is currently undergoing formation.

The HAeBe star HD 100546 may possess a forming planet. HD 100546 is a B9.5 V star, and at a distance of 103.6 pc (van den Ancker et al., 1997), it is particularly opportune to study the processes of planet formation.

There are several lines of evidence that a planet may be forming within the HD 100546 system. The Spectral Energy Distribution of the system shows a weak near-infrared excess short-ward of 10 μm, yet a strong far-infrared excess at $\sim$40μm (Dominik et al., 2003). It is hypothesized that this is caused by an inner cavity of $\sim$10 AU, inside which the dust is either optically thin or entirely cleared (Bouwman et al., 2003). A cause of this inner cavity may be a massive companion ($\geq$5 M_J) that halts the accretion of material from the outer part of the disk to replenish the inner disk beyond the planet (Lubow et al., 1999; Najita et al., 2007).

Observations using STIS on Hubble suggest that the inner cavity may be closer to 13 AU, due to the decreased Ly α emission and reflection nebulosity (Grady et al., 2005a).

Table 4.1 Log of PHOENIX Observations of HD 100546

Date	Integration (minutes)	Spectral Grasp (cm^{-1})	Slit P.A. (deg)
2002 December 16	20	2029 - 2040	90
2006 January 14	12	2027 - 2038	90
2006 January 14	20	2084 - 2090	90
2006 January 14	12	2105 - 2114	90
2006 January 14	20	2137 - 2147	90
2006 April 5	16	2006 - 2016	90
2008 December 21, 22	36	2141 - 2151	127, 217, 307

They also find that the central cavity is asymmetric, offset by $\sim$5 AU towards the southeast of the central star. Additionally, Grady et al. (2005a) place a constraint on the potential companion at M<0.06 $M_\odot$ based on unseen chromospheric emission beyond that of HD 100546. Thus, if companion exists it must either be a brown dwarf or exoplanet.

Acke & van den Ancker (2006a) observe the Oxygen [O i] 6300Å forbidden line. They observe a gap in the emission, and estimate an inner hole of 10 AU. From this, they infer the mass of a companion is 20 M_J and resides at 6.5 AU with an 11 yr orbital timescale.

Observations of ro-vibrational CO in the disk around HD 100546 also show evidence of a truncated disk. Brittain et al. (2009) find from the FWHM of the CO features that the gas disk has an inner radius of 13$\pm$6 AU.

We observe the ro-vibrational CO transitions and analyze the spectro-astrometric signal. From this, we attempt to explore further the inner disk of HD 100546.

4.3 Observations

We acquired high-resolution (R=50,000), near-infrared spectra of HD 100546 on December 16, 2002, January 14th, 2006, and December 21-22, 2008, using PHOENIX at the Gemini South telescope (Hinkle et al., 2003, 2000, 1998). The observations were centered around 4.7 μm to cover fundamental ro-vibrational transitions of CO. A summary of observations are presented in Table 4.1.

Observations in the 4.7 μm region are dominated by a strong thermal background. Therefore, an ABBA nod pattern between two positions separated by $\sim 5''$ is used to cancel the thermal continuum to first order. The scans are flat fielded, cleaned of hot and dead pixels, including cosmic ray hits, and then combined in the sequence (A_1-B_1-B_2+A_2)/2. Because the spectra are curved along the detector, they are first rectified by finding the centroid of each column and shifted to a common row. A one-dimensional spectrum is then extracted from the recrified spectrum. This spectrum is combined with an atmospheric transmittance model spectrum in order to find a wavelength solution. The model is created using the Spectral Synthesis Program (Kunde & Maguire, 1974), which accesses the 2000HITRAN molecular database (Rothman et al., 2003). Each spectrum is then ratioed to a standard star observed at a similar airmass to remove telluric absorption lines. Areas where the transmittance is below 50% are omitted. No corrections were made to match the airmass exactly, though the atmospheric lines matched to below 1% where the transmittance was above 50%.

4.4 Analysis

HD 100546 was observed on four different nights spanning six years, from 2002 to 2008. Table 4.1 describes when each observation was made, as well as the spectral coverage during those observations. These observations are separated into three different epochs: 2002, 2006 and 2008. The 2006 observations covered a number of settings, including an overlap of the 2002 and 2008 data, which only covers one setting, respectively. However, the data from 2002 do not overlap with 2008. The spectra from all of the observation dates are shown in Figure 4.1. Though there is not complete coverage between all of the epochs, we can compare the features from the different excitation levels over time. The normalized line profiles from the January 2006 data did not differ within the noise compared to the April 2006 data ($\sim$1%).

Emission is detected of a wide range of vibrational and rotational levels. The 2006 observations covered a number of settings, including an overlap in spectral coverage with the 2002 and 2008 data. The 2002 and 2008 observations each cover one setting, and they do not overlap. The normalized line profiles from the January 2006 data did not differ

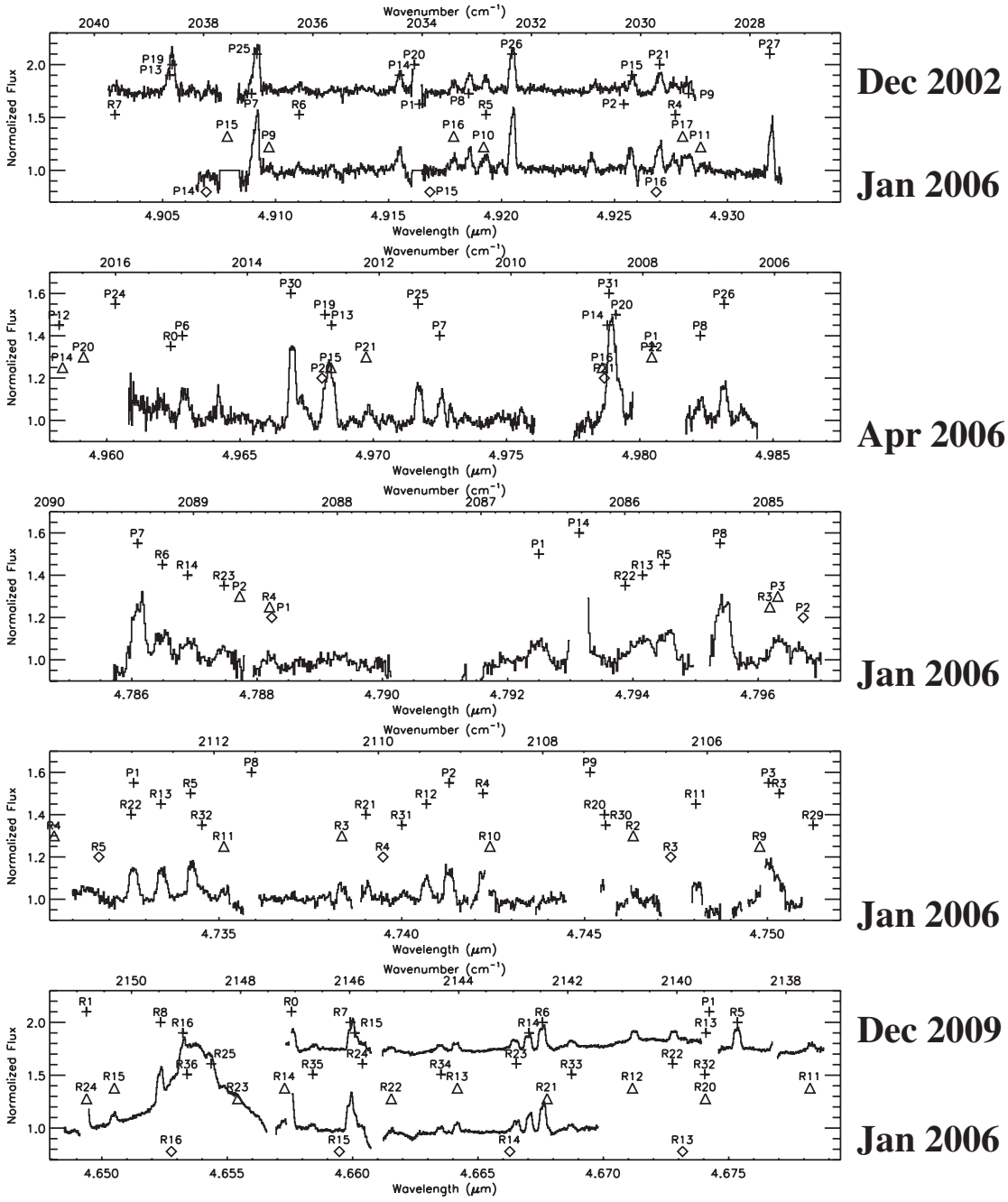

Figure 4.1 Observations of HD 100546 from 2002 through 2008, from 4.64 to 4.94 μm. A large range of excitation levels are probed both through different vibrational levels and also different rotational levels within a single vibrational level. The transitions of CO are overplotted on all of the spectra. Transitions of $^{12}C^{16}O$ are shown as crosses, $^{13}C^{16}O$ are shown as triangles, and $^{12}C^{18}O$ are shown as diamonds. The vertical spacing between the symbols represents the vibrational level - v=1-0 is near the top, v=2-1 is one level below, etc.

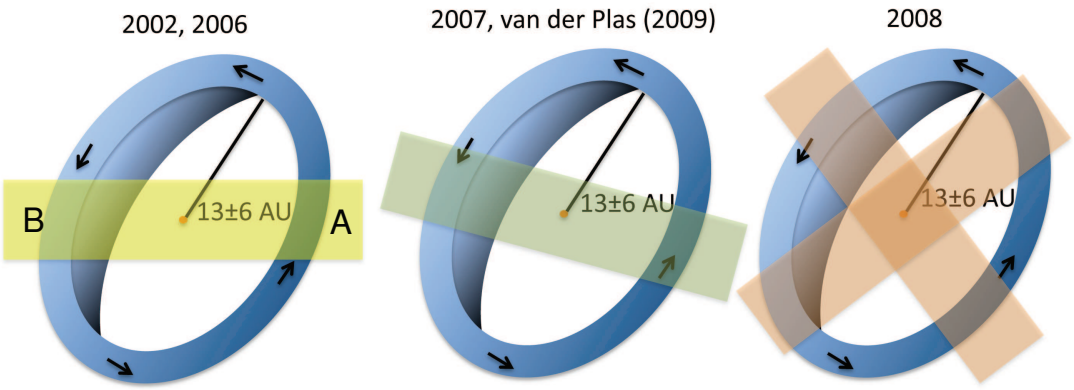

Figure 4.2 Schematic of the HD 100546 system. The ring represents the disk, while the inner wall is shown as the shaded region. The orientation of the slit with respect to the disk is presented for each epoch with a shaded rectangle (not to scale). For the 2002 and 2006 data, the direction of the A and B beams are indicated. The arrows on the disk represent the direction of rotation of the disk.

within the noise compared to the April 2006 data (∼1%), so we treat those observations as a single epoch. The inclination of the disk is 50°. There are conflicting reports of the disk PA. Coronagraphic imaging indicates that the PA is 127° (Grady et al., 2001). However, Acke et al. (2005) suggest the value is closer to 145°, which is supported by spectro-astrometry by van der Plas et al. (2009).

In addition to the line fluxes from the different dates, the spectro-astrometric signal is determined for each of the observations. Spectro-astrometry is a relatively new technique that takes advantage of high-resolution spectrometers with excellent imaging quality (**?**Acke et al., 2005; Pontoppidan et al., 2008; Brittain et al., 2009; van der Plas et al., 2009). If emission of gas in a circumstellar disk extends for ∼100 AU (as observed in HD 100546; Brittain et al., 2009), then at 103 pc, the disk appears to extend over ∼1″. By measuring the center-of-light in each velocity bin, the spatial offset can be determined, thus producing the spectro-astrometric signal. The orientation of the slit with respect to the position angle of the disk for the different observations is shown in Figure 4.2.

We adopt a similar method as Pontoppidan et al. (2008) to determine the spatial offset. We perform a Gaussian fit to each beam in the observation, summed up in frequency space, the centroid of which is then assumed to be the centroid of the star. Then, for each frequency, the "center-of-light" in that bin is compared to the centroid for the star, as such:

$$X_{\tilde{\nu}} = C\frac{\sum_i (x_i(\tilde{\nu}) - x_0)F_i(\tilde{\nu})}{\sum_i F_i(\tilde{\nu})}, \tag{4.1}$$

where C is the correction factor based on the amount of flux not included in the window over which the signal is calculated. $X(\tilde{\nu})$ is the spatial offset (the spectro-astrometric signal), x_i is the position of a given pixel, x_0 is the centroid of the star, and $F_i(\tilde{\nu})$ is the flux for pixel i at a specific wavenumber. For this analysis, C is found to be 1.13. We do not additionally correct for the dilution from the central star, because the model to which we will compare the data predicts a diluted signal. The dilution factor is related to the line-to-continuum ratio, written for a specific wavenumber bin:

$$X_{\text{undiluted}} = X_{\tilde{\nu}}\left(1 + \frac{F_{\text{cont},\tilde{\nu}}}{F_{\text{line},\tilde{\nu}}}\right). \tag{4.2}$$

To determine the spectro-astrometric signal, we analyze the unblended lines in each spectrum. Table 4.2 shows the unblended lines from each epoch.

4.5 Results

To begin, the 2002 data are shown in Figure 4.3. The data are separated in the v=1-0 data, and the v$'$ >1 data. There are 5 lines included in the v$'$ >1 data. Both levels show an asymmetry in the flux, yet there appears to be no asymmetric signal in the spectro-astrometric signal.

The 2006 data are shown in Figure 4.4. Again, the data are separated into the v=1-0 data, and the v$'$ >1 data. The spectral coverage was much greater in 2006 than 2002. The same v=1-0 line is used in both 2002 and 2006, yet there are a number of more lines used in the v$'$ >1 data (28). Again, an asymmetry is seen in the lines, yet now there is a larger asymmetry in the v=1-0 line. The spectro-astrometric signal is no longer symmetric, especially noticed in the v=1-0 P26 line.

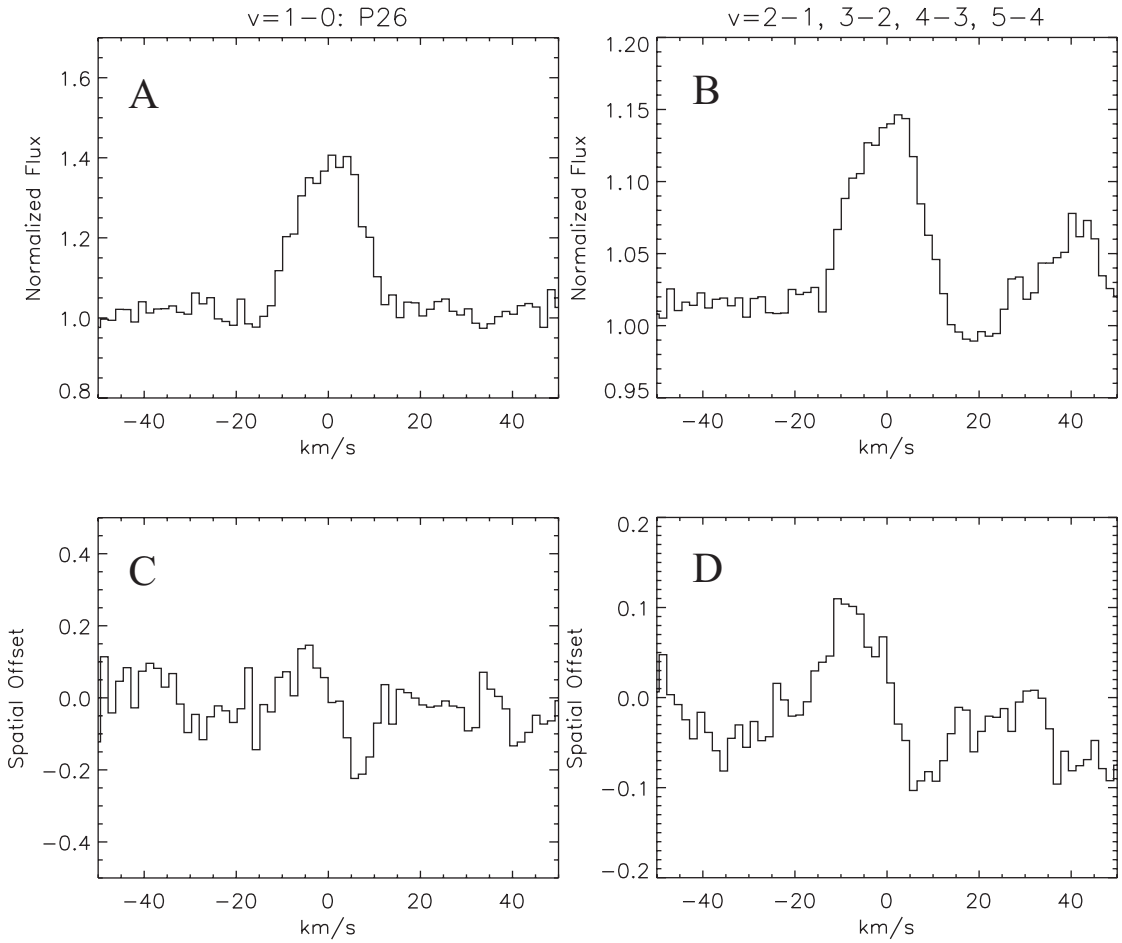

Figure 4.3 The normalized flux from the v=1-0 P26 line (A); the average of the v >1 lines in the order that are not heavily blended with telluric features (B); The spatial centroid of each velocity bin around the P(26) line in units of pixels (C); The spatial centroid of each velocity bin around the clear higher vibrational lines in units of pixels (D). There is a modest asymmetry in the line profiles, yet the spectro-astrometric profiles are symmetric to within our signal to noise. The measurement of the offset has not been corrected for dilution by the continuum PSF. The seeing was $\sim 0.8''$.

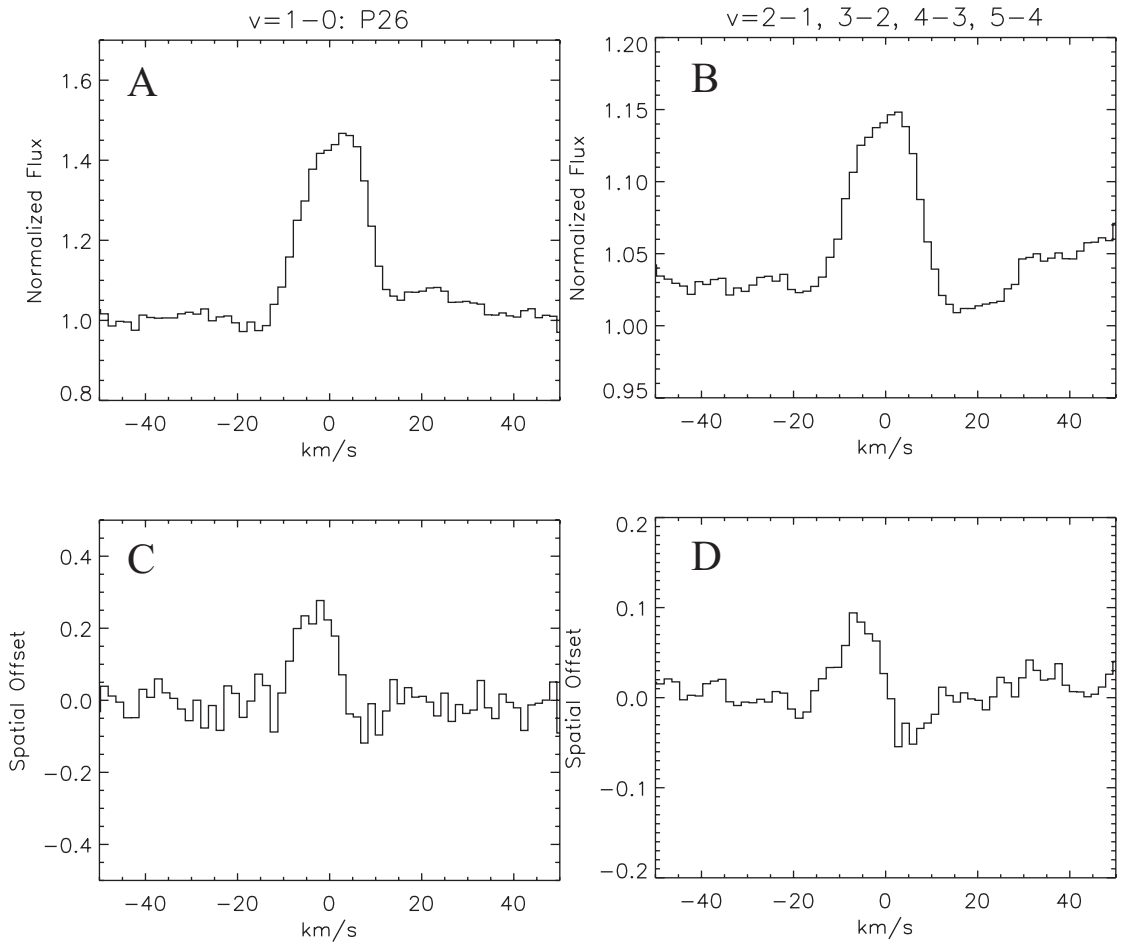

Figure 4.4 The normalized flux from the v=1-0 P26 line (A); the average of the v >1 lines in the order that are not heavily blended with telluric features (B); The spatial centroid of each velocity bin around the P26 line in units of pixels (C); The spatial centroid of each velocity bin around the clear higher vibrational lines in units of pixels (D). There is a modest asymmetry in the line profiles. In 2006, v=1-0 P26 line is more asymmetric than it was in 2002, though the lines originating in levels with v¿1 have the same profile as 2002. The spectro-astrometric measurement of the P26 line has varied dramatically, while the lines originating from higher levels are consistent with no variation from 2002 to 2006. The seeing was $\sim 0.5''$.

Table 4.2 Unblended Lines in Each Epoch

Epoch	Vibrational Level	Unblended Lines
2002	v=1-0	P26
	v=2-1	P21
	v=3-2	P14, P15
	v=4-3	P8, P9
	v=5-4	...
2006	v=1-0	P26
	v=2-1	P2, P8, P21, P25, P26, R6, R8
	v=3-2	P1, P14, P15, R4, R5, R14
	v=4-3	P8, P9, R5, R6, R12, R13, R23
	v=5-4	P6, P7, P8, R13, R14, R33, R34, R35
2008	v=1-0	...
	v=2-1	R5, R6
	v=3-2	R14
	v=4-3	R22, R23
	v=5-4	R33, R34, R35

The 2008 data are shown in Figure 4.5. Here, there are no observations of the v=1-0 transitions. However, there are two slit orientations presented of the 8 $v' > 1$ lines - close to the semi-major and semi-minor axis of the disk. Similar to all of the other epochs, the lines show an asymmetry in the flux. However, the spectro-astrometric signal for the orientation close to the semi-major axis shows a symmetric profile. The semi-minor axis orientation shows a potentially asymmetric profile.

To compare the observations, Figure 4.6 shows the flux calibrated spectrum from the two dates. Also included, is the model presented in (Brittain et al., 2009), fit to the 2002 data. The difference between the two dates is overplotted. An increase of $\sim$50% in the asymmetry is seen in the 2006 data, yet the higher vibrational levels do not show a change in flux.

Figure 4.7 shows a closer view of the excess seen in the P26 line. The excess itself is offset from the center of the line (4 ± 2 km s^{-1}), with a width larger than the 6 km s^{-1} instrument resolution of PHOENIX (excess width of 15 ± 2 km s^{-1}).

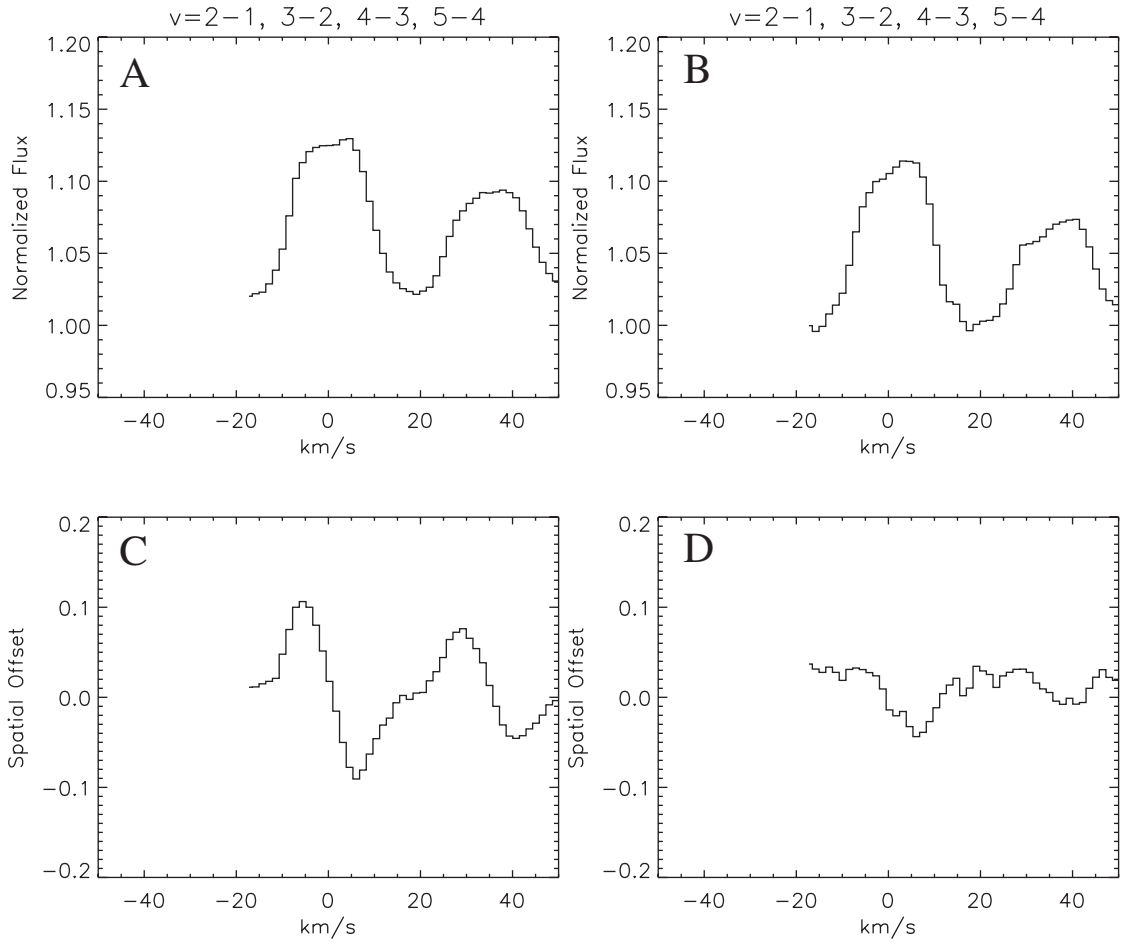

Figure 4.5 Line profile and spectro-astrometric signal of v >1 lines with slit nearly aligned along semi-major axis (127°; A and C) and semi-minor axis (37°; B and D). The line profiles still show a slight asymmetry that appears to be real. The spectro-astrometric signal of the lines observed near the semi-major axis is symmetric (C). The spectro-astrometric signal taken with the slit nearly aligned along the semi-minor axis may be asymmetric (D). Aligning the slit with an orientation off of the semi-minor axis is expected to produce a small spectro-astrometric signal, which is observed in the orientation along 37 deg (20 deg off the semi-minor axis at 57 deg).

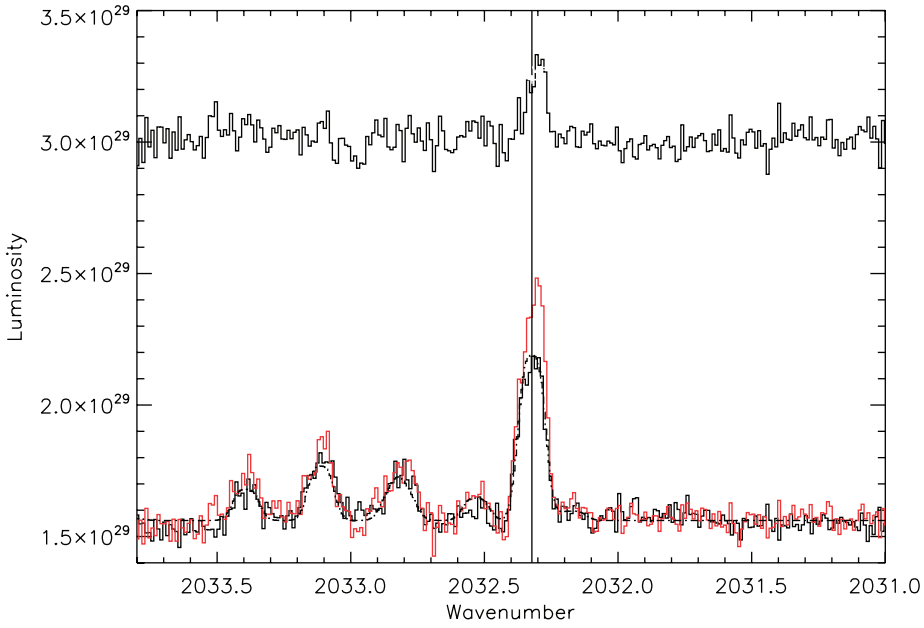

Figure 4.6 Flux calibrated spectrum from 2006 (red), 2002 (solid, black line), and the model for the 2002 data (dot-dashed, black line). Plotted above is the difference between the 2006 and 2002 observations. There is a peak in excess luminosity of 3.1×10^{28} erg s^{-1} with a width larger than 6 km s^{-1} (line width of PHOENIX).

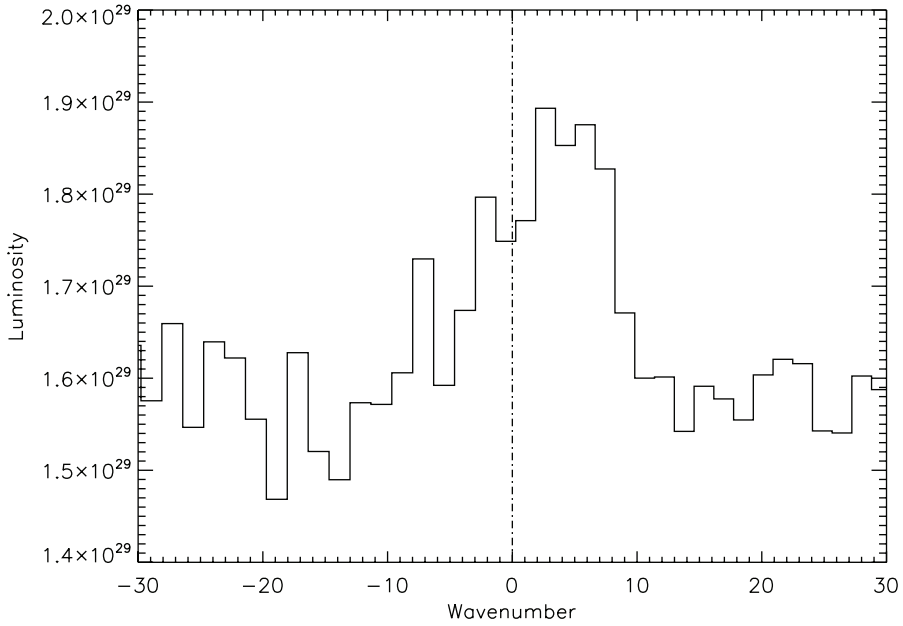

Figure 4.7 Residual of the P(26) line (2002 data subtracted off of 2006 data). The central velocity of this excess is 4 ± 2 km s^{-1}. The dot-dashed line is the center of the P(26) features. The residual itself is asymmetric.

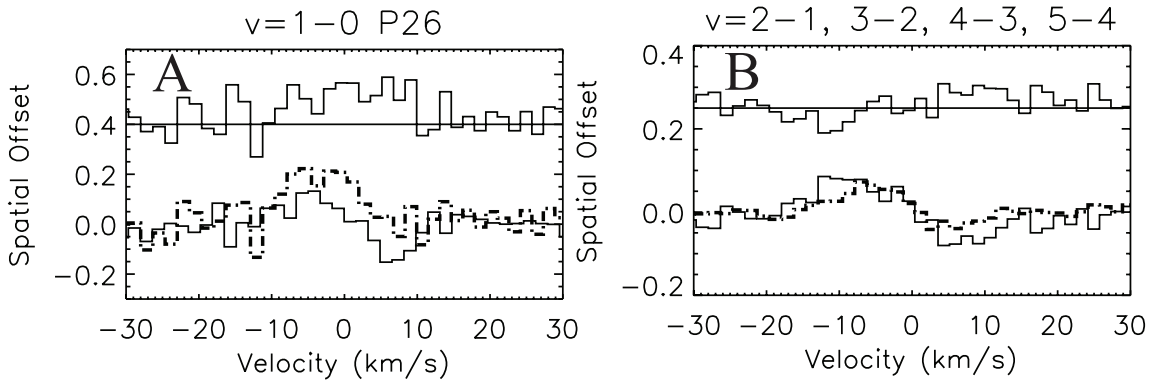

Figure 4.8 Comparison of spectro-astrometric signal from the v=1-0 P26 line between 2002 and 2006 (A). Comparison of spectro-astrometric signal from the v >1 lines between 2002 2006 (B). In both panels, the spectrum from 2002 is plotted with a solid line, the spectrum from 2006 is plotted with a dot-dashed line, and the difference is plotted offset above. The v=1-0 P26 line shows a difference in the spectro-astrometric signal, but the v >1 lines show no difference within the noise of the data.

To compare the spectro-astrometric signal, Figure 4.8 shows the signals from 2002 and 2006. Both the v=1-0 P26 line and the $v' > 1$ lines are shown from both dates. The residuals are also shown for both. The v=1-0 P26 line shows a change between the dates, while the $v' > 1$ signal does not show a change between 2002 and 2006.

To summarize, there appears to be an excess in flux for the v=1-0 P26 line that changes between 2002 and 2006, while the v' >1 lines do not show a change between the two dates. Similarly, the spectro-astrometric signal of the v=1-0 P26 line changes between the two dates, while the v' >1 does not appear to change.

4.5.1 Modeling the Flux and Spectro-astrometry

To fit the data, a model was used to fit the fluxes from the 2002 observations. The model is presented in Brittain et al. (2007a, 2009). The model used to fit to the flux was input into the spectro-astrometric model described in the Appendix to produce a synthetic spectro-astrometric signal. Figure 4.9 shows the modeled flux and spectro-astrometric signal compared to the data from both epochs. The flux can be well-reproduced from 2002, and

the spectro-astrometric signal is fit well with this model. However, the 2006 data does not fit well, both under-predicting the flux and the spectro-astrometric signal.

The observations from 2002 and 2006 and the comparison to the model is shown in Figure 4.10. The model reproduces the v′ >1 observations, both in flux and spectro-astrometric signal, in both epochs. The asymmetry hinted in the 2006 observations can be seen clearer in contrast to the symmetric model. Still, the degree of the asymmetry is extremely modest in comparison to the asymmetry seen in the v=1-0 spectro-astrometric signal.

Thus, a comprehensive model must reproduce an excess in flux of the v=1-0 lines but not the v′ >1 lines, changing over time. Additionally, the spectro-astrometric signal must change from a symmetric profile to an asymmetric profile.

4.5.2 Effect of a Spiral Arm

One such explanation may be that a spiral arm is induced in the disk. Grady et al. (2005a) find evidence for large-scale structure similar to a spiral arm, which may continue to the inner disk. To explore this possibility, the effect of a spiral arm on both the flux and spectro-astrometry is modeled.

For this case, a simple spiral arm model will be used. A single arm is introduced, described by $r = 7\theta$, with the starting point of the spiral being at one of the points on the semi-major axis. The spiral width is assumed to be expanding radially through the disk, with an extent of $0.1r$.

The disk with a spiral arm is shown in Figure 4.11, oriented along the semi-major axis. The unresolved signal that would come from the disk is shown in Figure 4.12. The flux still appears symmetric, and therefore would not be distinguishable. Thus, the flux from a disk with a spiral arm would appear as an axisymmetric disk when studying the flux alone.

However, despite the fact that a spiral arm is not distinguishable using the flux, the spectro-astrometric signal does show a difference. Figure 4.13 shows the spectro-astrometric signal when the slit is oriented along the semi-minor axis. In this orientation, an axisymmetric disk would show no signal, yet a disk with a spiral arm shows a unique signature.

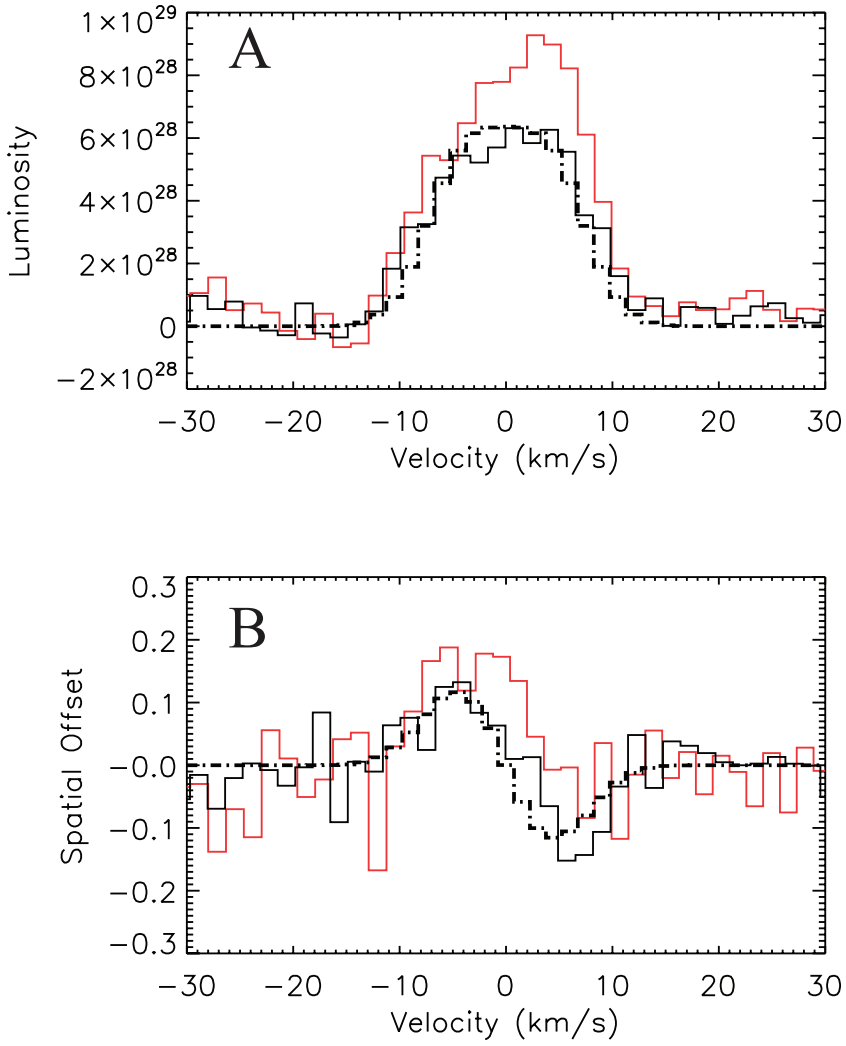

Figure 4.9 The luminosity from 2002 (solid black), 2006 (red) and the model (dot-dashed line) for 2002 (panel A). Panel B shows the spectro-astrometric signal with the same color scheme. Using the fluorescence model described in Brittain et al. (2007a, 2009), the luminosity (ergs s^{-1}) is used as input as a function of radius to produce a model of the spectro-astrometric signal (pixels) assuming the emission arises from an axisymmetric disk. The model reproduces the 2002 data in both the luminosity and spectro-astrometric signal. However, the model does not fit the 2006 data.

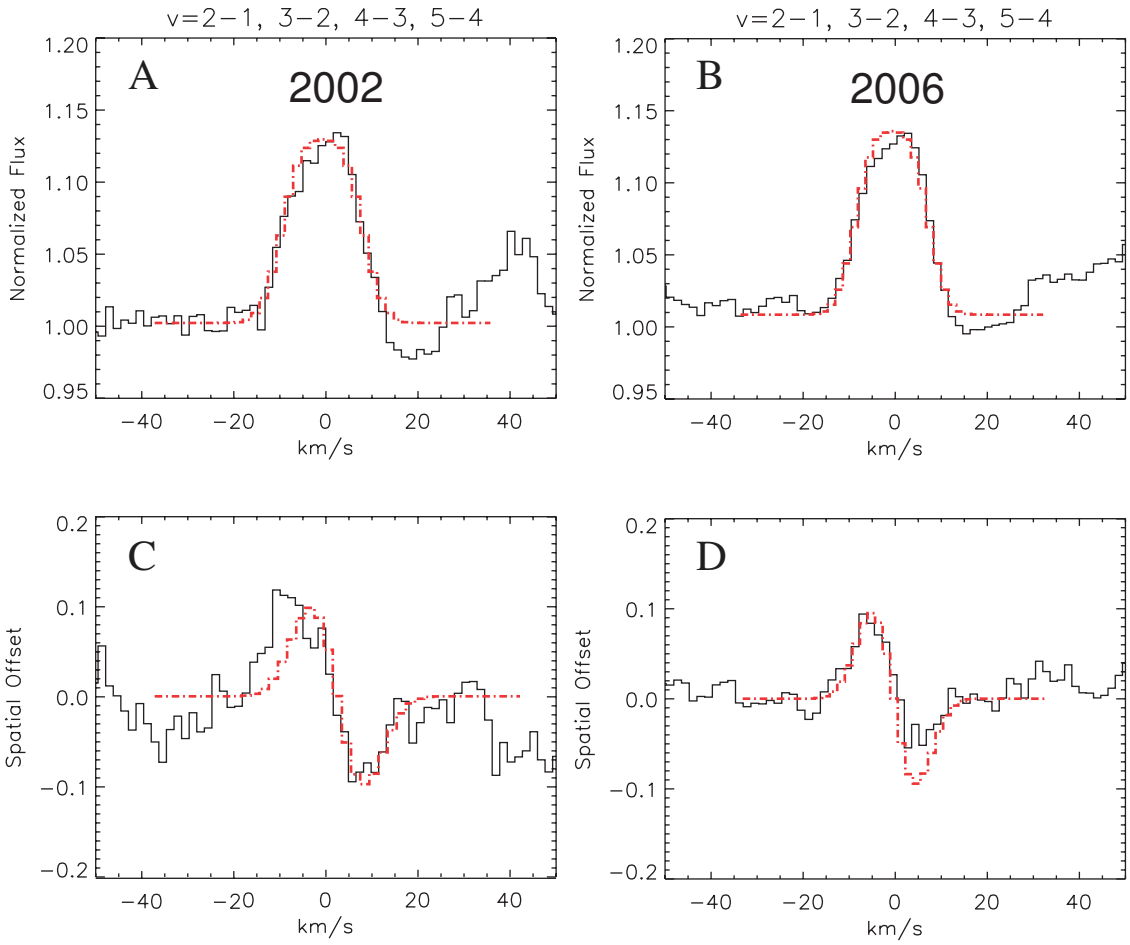

Figure 4.10 Normalized flux and spectro-astrometry (offset in units of pixels) of the 2002 v >1 observations (A and C), luminosity and spectro-astrometry of the 2006 v >1 observations (B and D). The model (red dot-dashed line) reproduces the luminosity and spectro-astrometry within the noise, suggesting that the excess is only seen in the v=1-0 lines.

To explore the effect further, Figure 4.14 shows the disk with a slit orientation along the semi-major axis. The flux from this disk would be the same as the orientation along the semi-minor axis (Figure 4.12). The spectro-astrometric signal is shown in Figure 4.15. The asymmetry is observed in this orientation as well, and would be detectable. Thus, a spiral arm can be detected through the spectro-astrometric signal, at even a non-optimal orientation of the slit with respect to the disk.

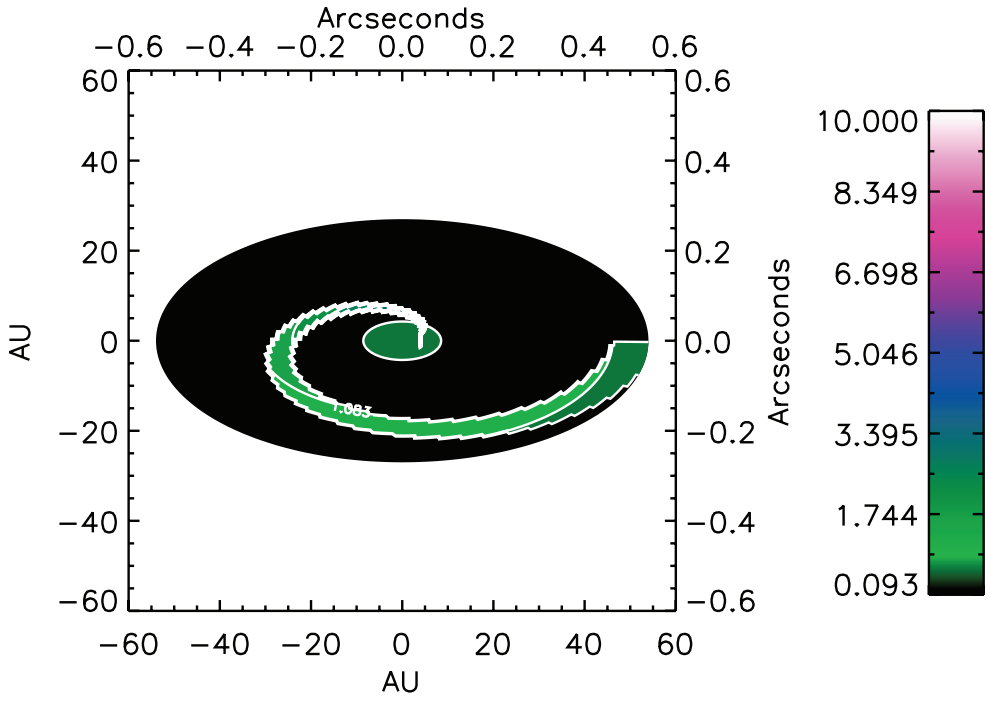

Figure 4.11 Image of the spiral arm in the disk. The flux within the spiral arm is ten times the flux at that radius outside the spiral arm. The spiral is described by $r = 7\theta$.

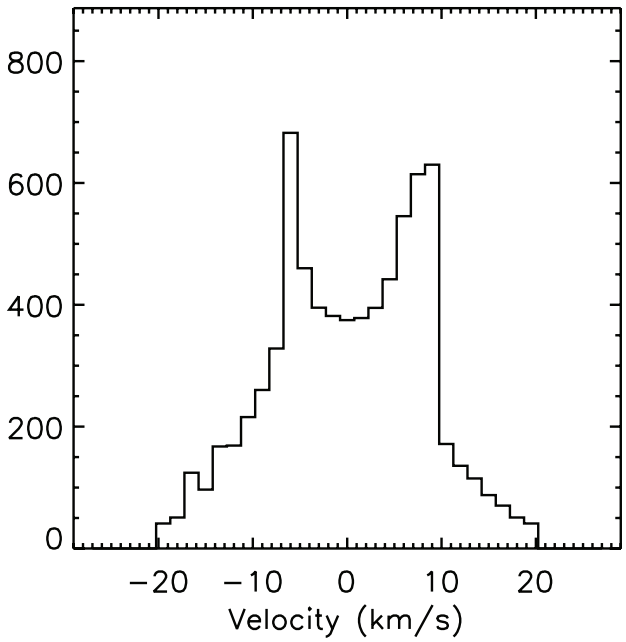

Figure 4.12 The unresolved flux signal from a disk with a spiral arm in arbitrary units. The signal is slightly asymmetric, yet when resolved into the instrument resolution of PHOENIX or NIRSPEC, would not be detectable. Thus, looking at disk flux alone may not determine a spiral arm within the disk.

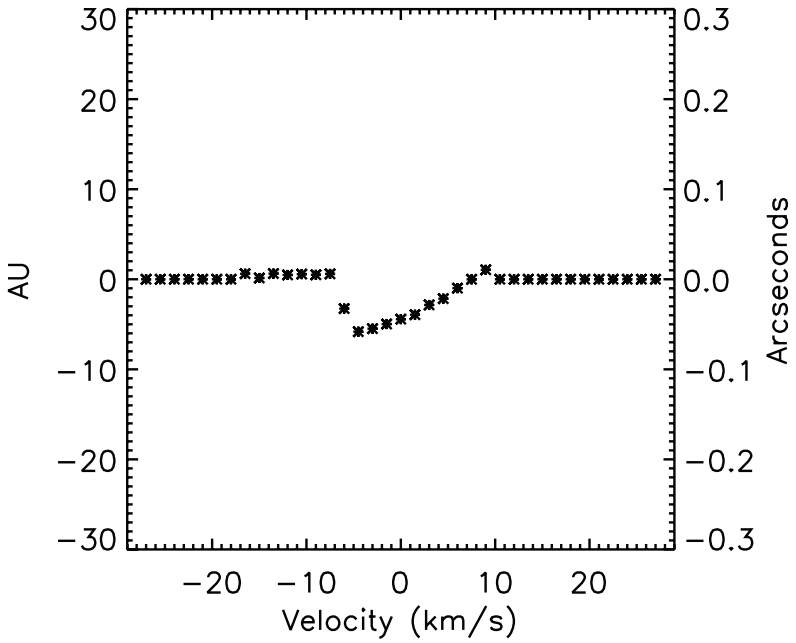

Figure 4.13 The spectro-astrometric signal of a disk with a spiral arm. As the orientation is along the semi-minor axis, the signal comes from the asymmetry of the spiral arm. Observing even at a non-optimal position angle produces a signal.

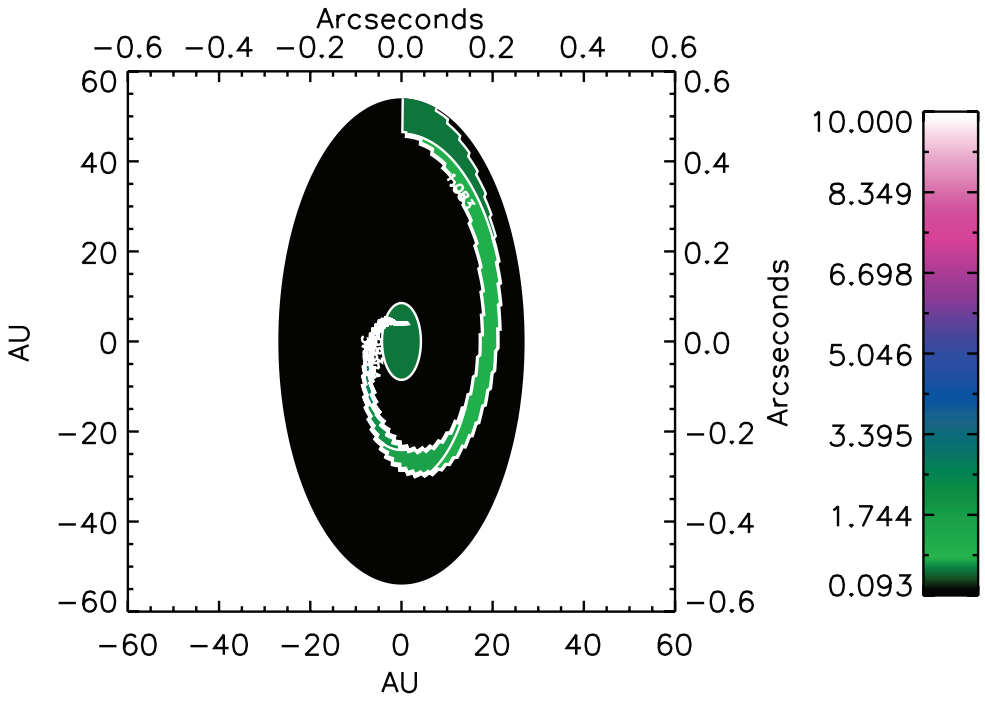

Figure 4.14 A view of the disk with the orientation of the slit along the semi-major axis of the disk.

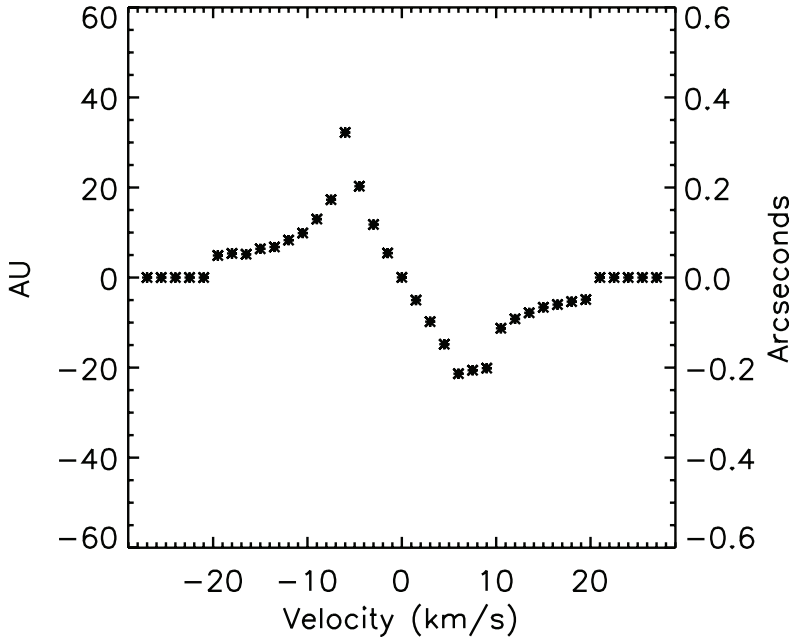

Figure 4.15 Spectro-astrometric signal of a disk with a spiral arm, observed along the semi-major axis. A distinct asymmetric signal is observed in this orientation, which is not expected if the disk was axisymmetric.

The signal produced from a spiral arm does not fit the data presented from HD 100546. Most notably, the flux is significantly asymmetric in HD 100546, while the prediction for a spiral arm is symmetric by comparison. Additionally, the spectro-astrometric signal predicted from a spiral arm for the different orientations do not match the signals from HD 100546. Thus, the unique signal from HD 100546 does not seem to come from a spiral arm.

4.5.3 Introducing a Planet

One other possibility to explain the asymmetry is a planetary companion in the system with a protoplanetary disk. A forming planet accretes material from the outer disk through a circumplanetary disk (Ayliffe & Bate, 2009a,b). Modeling of this material shows a density of 10^{14} cm^{-3} and temperature of 1500 K (the temperature of the CO observed around HD 100546). The CO circumplanetary disk will be in LTE and optically

thick, having a signature of excess emission in lower vibrational levels, but not in higher vibrational levels. Further, the radius of the circumplanetary disk around a Jupiter mass protoplanet 10 AU from a 2.4 $M_{\odot}$ star is 0.15 AU. Thus the luminosity of the collisionally excited CO emission from a circumplanetary disk should be comparable to the UV fluoresced CO emission from the outer disk. This is consistent with what was observed in HD 100546.

To predict the emission from a planet, an additional code was created to contribute to the spectro-astrometric model used earlier (code specifics described in Appendix). Initially, the excess is fit using a circumplanetary disk with a radius of 0.5 AU, a temperature of 1500 K, and orbiting 12 AU from the star. Figure 4.16 shows the effect the planet has on the emission and spectro-astrometric signal, compared to the data from 2002 and 2006, as well as the model without a planet fit to 2002. The planet model fits the flux from 2006 well, but the spectro-astrometric signal is not fit by the model.

However, another possibility is the disk around HD 100546 is elliptical, causing the central star to orbit around the center of mass Kley & Dirksen (2006). The eccentric disk causes a higher accretion rate onto a planet within the system, allowing the formation of more massive planets (>5 M_{Jup}). In HD 100546, evidence for an offset is observed. Grady et al. (2005a) find the reflected emission from the disk is centered 5 AU from the central star.

If the central star is providing the continuum emission and the lines are produced from the disk, then an offset of the disk with respect to the central star will provide a shift in the spectro-astrometric signal. The offset would not affect the continuum, but only the signal where the lines originate. This is observed in the 2006 data (see Figure 4.16). The offset of the spectro-astrometric signal from 2006 is $0''.01$, or 1 AU. Thus, it is possible that the disk is eccentric and is offset from the star. The excess flux can still be explained by a circumplanetary disk, only affecting part of the spectro-astrometric signal.

For completeness, the spectro-astrometric signal is fit assuming the disk is not elliptical, and the spectro-astrometric signal from 2006 is due to disk emission alone. Figure 4.17 shows a model that fits the spectro-astrometric signal from 2006 (ignoring the overall flux). A second object is included to fit the offset of the spectro-astrometric signal, which

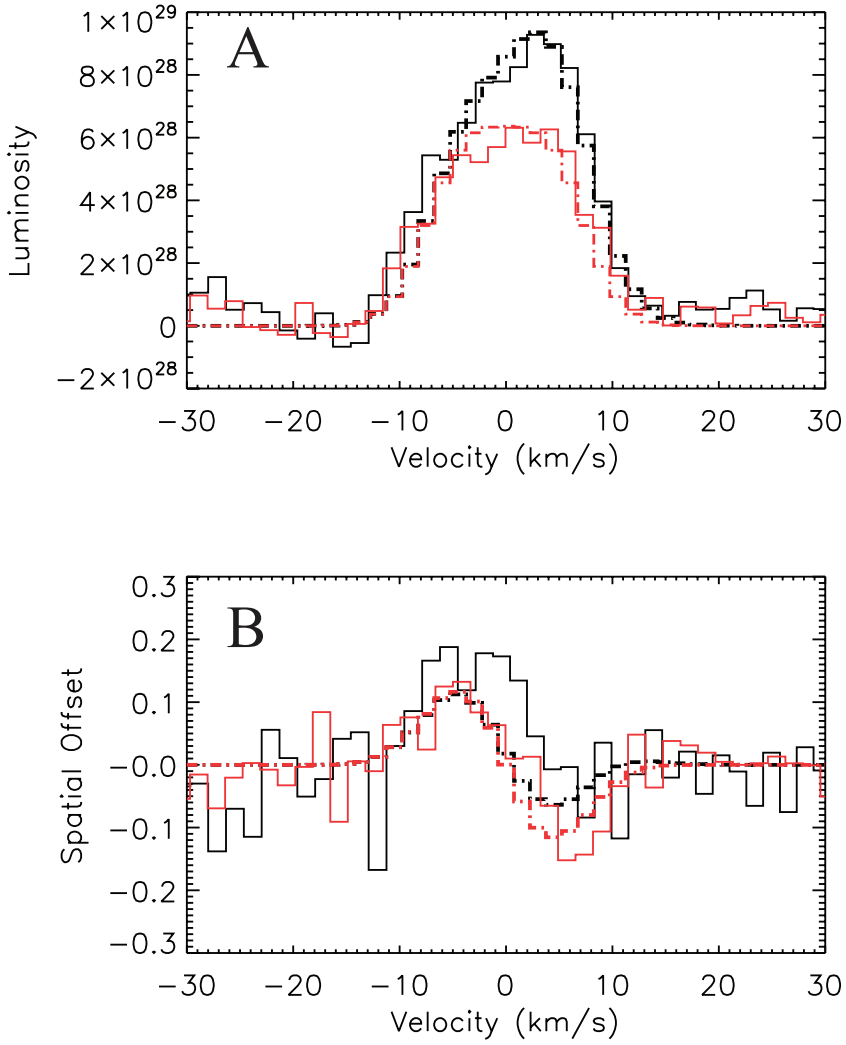

Figure 4.16 Luminosity of the data and models from 2002 (red lines) and 2006 (black lines) are shown in panel A. Spectro-astrometric signal of data and models from 2002 (red lines) and 2006 (black lines) are shown in panel B. The top panel is luminosity in erg s^{-1}, and the bottom is spatial offset in pixels. Shown is the v=1-0 P(26) lines again, but this time a model is shown (black, dot-dashed lines) in an attempt to reproduce the luminosity and spectro-astrometry observed in the 2006. To fit the excess, material was included with a projected velocity of 4 km s^{-1} at a distance of 12 AU from the central star. The emission had a FWHM ($\sim$8 km s^{-1}) larger than the intrinsic line width of PHOENIX (6 km s^{-1}) to spread the luminosity out over more velocity bins. We do not fit the more extended emission in the blue velocity channels.

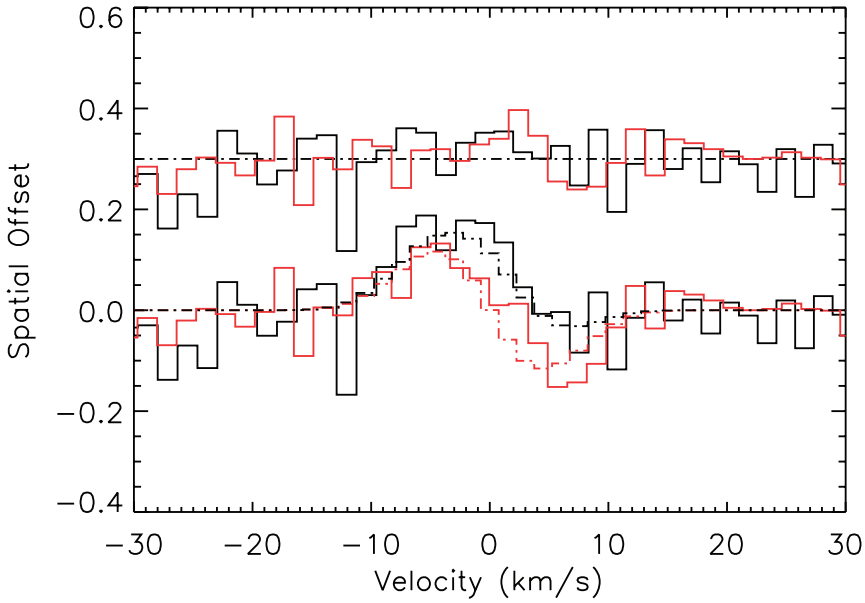

Figure 4.17 Spectro-astrometry from the v=1-0 P(26) line, with the spatial offset in pixels. This time, the data from 2002 (red) with the model (red, dot-dashed) plotted, as well as the difference between the data and model plotted above, offset by 0.3 pixels. Also plotted is the spectro-astrometric signal from 2006 (solid black) is plotted against another model (black, dot-dashed), with the difference plotted above. The model to fit the spectro-astrometric signal is different from Figure 4.10. In this case, the total luminosity is ignored, and the focus is on fitting the spectro-astrometric signal. In this case there are two excesses. The first is the one described in Fig. 10, and another excess is input with a projected distance of 20 AU with a positive offset, a central velocity of -1 km s^{-1}, and having a luminosity 8 times larger than the previous example.

is 8 times larger than the planet used in the previous example. In this case the signal is fit, but requires extremely large emission.

4.5.4 Summary

To summarize, HD 100546 was observed over three different dates. The luminosity of the v=1-0 lines increased by 50% between 2002 and 2006. The excess emission is not centered on the line, having an offset of 4±2 km s^{-1}. Conversely, the luminosity and spectral profile of lines originating from the vibrational levels $v' > 1$ show minimal variation.

The spectro-astrometric signal of the v=1-0 lines change from consistent with an axisymmetric disk with gas in Keplerian orbit to evidence of non-axisymmetric disk structure. However, the lines originating from higher vibrational levels are consistent with gas in a Keplerian orbit with axisymmetric structure during all three observing epochs. The origin of the non-axisymmetric structure is not clear. A spiral arm does not reproduce the observations. A source of excess emission in the inner disk appears to be necessary but not sufficient to fit the change in the spectro-astrometric profile of the line. A combination of a disk offset and a second object may be explain the observations.

CHAPTER 5

SUMMARY

5.1 Collisional Excitation

The main finding of the study of β Pictoris was that the observed CO is sub-thermally populated, which allowed the disk mass to be determined. The excitation of the gas is caused by atomic hydrogen colliding with CO. Integration of the hydrogen over the entire disk demonstrates that the mass is 0.17 $M_{\oplus}$. This mass is large enough to explain the braking of the gas explored by Fernández et al. (2006). Previously, it was assumed that the abundance of carbon would be enough to brake the gas. Another explanation is found, that of ion-neutral collisions, as the disk mass is larger than the threshold of 0.1 $M_{\oplus}$ needed for this scenario to become prevalent. We predict a mass for the hydrogen gas, which can be tested with future facilities, such as the Square-Kilometer Array.

The process of determining the density of collisional excited gas can be applied to other sources. It is not necessary that the gas be sub-thermally populated to determine the density of the material. The lower limit of the gas density can still provide key information about the system (e.g. Gibb et al., 2010).

5.2 Survey Data

The CO survey of HAeBe stars show the following: first, about 60% of the disks in the survey show a detection of CO. Emission is found from all accreting disks, unlike what is seen in T Tauri stars. We find no emission coming from the debris disks. The excitation of CO is observed to be from both thermal excitation as well as fluorescence. Additionally, we find that the Brγ luminosity correlates with the CO luminosity. However, the CO luminosity does not correlate with the PAH luminosity.

In transition disks (e.g. HD 100546), the inner edge of CO and dust are observed to be co-spatial. Despite the fact that grain growth is commonly claimed in disks, we do not see evidence for this scenario. Additionally, after approximately 10 Myr, the CO seems

to be mostly unobservable. Further study of some of the individual sources is necessary to understand these processes in greater detail.

5.3 Spectro-astrometry as a Technique

The main finding of this project is that observations support the presence of a companion in the HD 100546 system. The companion is compatible with a planet. The excess of flux in the lower vibrational levels are observed to change over time, and the spectro-astrometric profile of these lines also change. However, the higher vibrational levels do not change over time, as expected from an orbiting object with strong thermal emission coming from a protoplanetary disk. If true, this would be the first time a protoplanet has been discovered in formation.

In general, there is more information provided in the stellar continuum-subtracted spectrogram from a disk than what is produced in a typical spectro-astrometric plot shown this thesis. The best signal-to-noise is recovered when summing down from a three-dimensional data cube to a two-dimensional plot. This is useful to compare to modeling to determine if the large-scale structure of the disk is assumed to be correct. However, the spectrogram provides the flux at a specific velocity and spatial offset. Despite there being a degeneracy between the location in the disk and velocity, observing at multiple position angles can break this degeneracy. Currently, the model cannot directly produce what would be observed in a reduced spectrogram.

5.3.1 Other Tracers

While CO is a robust tracer of the circumstellar disk gas, other molecules may provide further study of the disk. For example, finding the distribution of H_2O in disks that are forming planets may determine whether water exists in the same region that the planet is forming, or whether water would need to be transported to an already formed planet.

There have been observations of H_2O and another abundant molecule, OH, using the Spitzer Space Telescope and Nirspec at Keck II (Salyk et al., 2008). Presently, there have been no spectro-astrometric observations of these molecules. I plan to use the model I

have created to produce synthetic observations to show the viability of using this technique on these molecules, and propose to observe some of the brightest sources from the sample presented in this work.

5.3.2 Asymmetries

Modeling of the asymmetry of the gas in the disk was only applied to the special case of HD 100546. However, it should be noted that some predictions can be made about other systems or other specific cases of a disk asymmetry. It was shown how a planet or a spiral arm affects the flux and spectro-astrometric signal, but other kinds of asymmetries have yet to be explored. For example, the case of an eccentric disk or a bulk asymmetry will produce a unique spectro-astrometric signal. It is unclear the specific signal an eccentric disk would produce, especially given the number of permutations that exist between the eccentricity or the position angle.

APPENDIX

Programs Written

Listed are the programs with short descriptions of the functions and routines used to aid in analysis for various parts of this dissertation.

Collision Excitation Analysis

The following set of programs were used in the analysis for debris disks (**?**). Figure A.1 shows how the programs are organized.

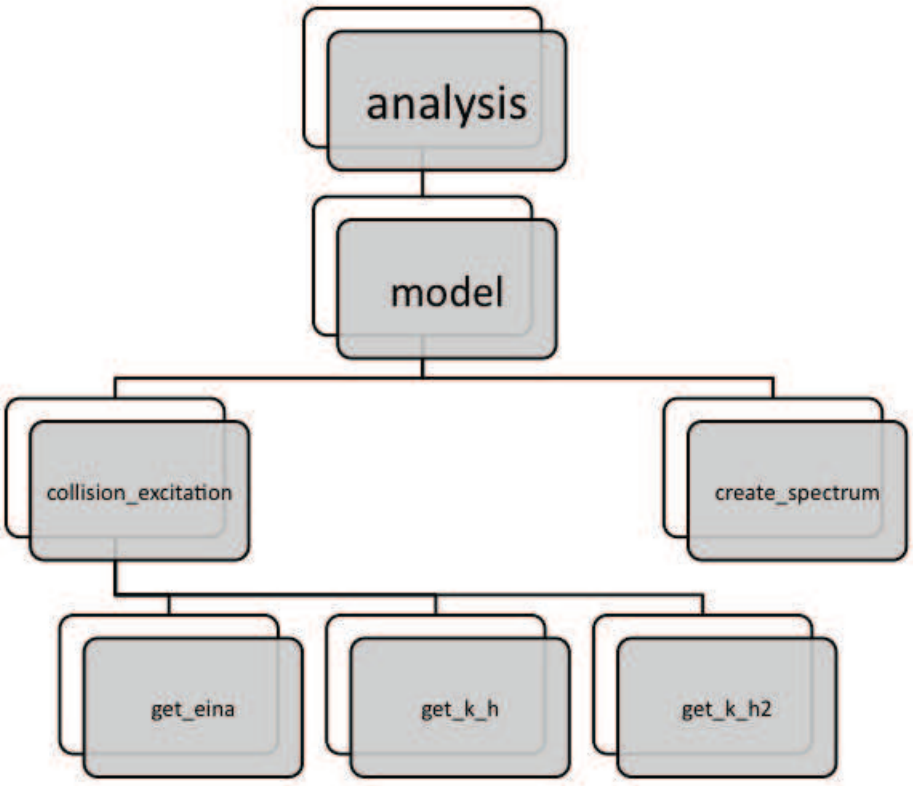

Figure A.1 A chart graphically describing the programs involved with spec_astro.pro.

analysis.pro

This is the over-arching program that compares a model spectrum created from a given temperature of colliding gas, hydrogen density and column density of CO. Depending on the necessary quantities, a for-loop is used to call *model.pro* and compare to actual data. A simple chi-squared minimization is used to determine the best fit to the data. It should be noted that as the density increases beyond what is required to thermalize the lines, the minimization may not be reached within a reasonable range for densities. It is recommended to look at a plot of the best fit as a function of density to see how it changes as the density increases.

model.pro

- Input:
  - Temperature
  - Hydrogen density
  - Column density of CO
- Output:
  - Interpolated model spectrum
- Description:
  This function takes in the input variables to compute a model spectrum. It is mostly a placeholder program for the observed data to keep it from the analysis program and separate from the other programs that should remain constant. In theory, one could change just this program to call the observed data to fit to the spectrum that will be produced in the following programs.

collision_excitation.pro

- Input:
  - Temperature
  - Hydrogen density
  - Number of levels (optional)
- Output:
  - Array of relative level populations
- Description:

This function takes in the disk variables and calculates the populations of the rotational CO levels. The population is calculated by creating a rate equation with the collisional excitation and de-excitation, stimulated and spontaneous (de-)excitation, and the radiation from the cosmic microwave background. The rate equation is put into a matrix, which is assumed to be in steady-state, and solved to produce the level populations.

get_eina.pro

- Input:
  - J level
- Output:
  - Einstein A coefficient
- Description:
  This program determines the einstein-A value for a specific level. This just recalls a database to save from having unnecessary variables in the program.

get_k_h.pro

- Input:
  - Temperature
  - J_{up}
  - J_{low}
- Output:
  - Collision rate
- Description:
  This program takes in a possible transition between two rotational levels to determine the collision constant for a hydrogen-CO collision. Multiplying this value with the density of atomic hydrogen is the collision rate that can be added to the rate equation. It reads in values given by Green & Thaddeus (1976) (which are only given for 5, 10, 20, 40, 60, 80, and 100 K), then interpolates the rate to the input temperature.

get_k_h2.pro

- Input:
  - Temperature
  - J_{up}
  - J_{low}

- Output:
  - Collision rate
- Description:
  This program takes in a possible transition between two rotational levels to determine the collision constant for a H_2-CO collision. Multiplying this value with the density of H_2 is the collision rate that can be added to the rate equation.

create_spectrum.pro

- Input:
  - Array of level populations (from *collision_excitation.pro*)
  - Column density of CO
- Output:
  - Structure with frequency array and model spectrum array
- Description:
  This program uses the level populations of CO with the column density to create a frequency array and model spectrum.

Spectro-astrometry Programs

The following codes were written to model the spectro-astrometric signal from a circumstellar disk. Included are two extra programs that add the effect of a planet or a spiral arm. Figure A.2 shows the organization of these programs.

spec_astro.pro

This is the overarching program that creates a simulated disk and spectro-astrometric signal. The disk parameters come from the fluorescence code described in Brittain et al. (2009) and Brittain et al. (2007a). The parameters already set include the distance, size, and line flux. Parameters that are set by the user are the inclination, position angle (with respect to the slit position angle), the slit size, and the spectral resolution. Figure A.3 shows what appears on the screen when running spec_astro.pro.

calc_flux_vel.pro

- Input:
  - Array of radial points

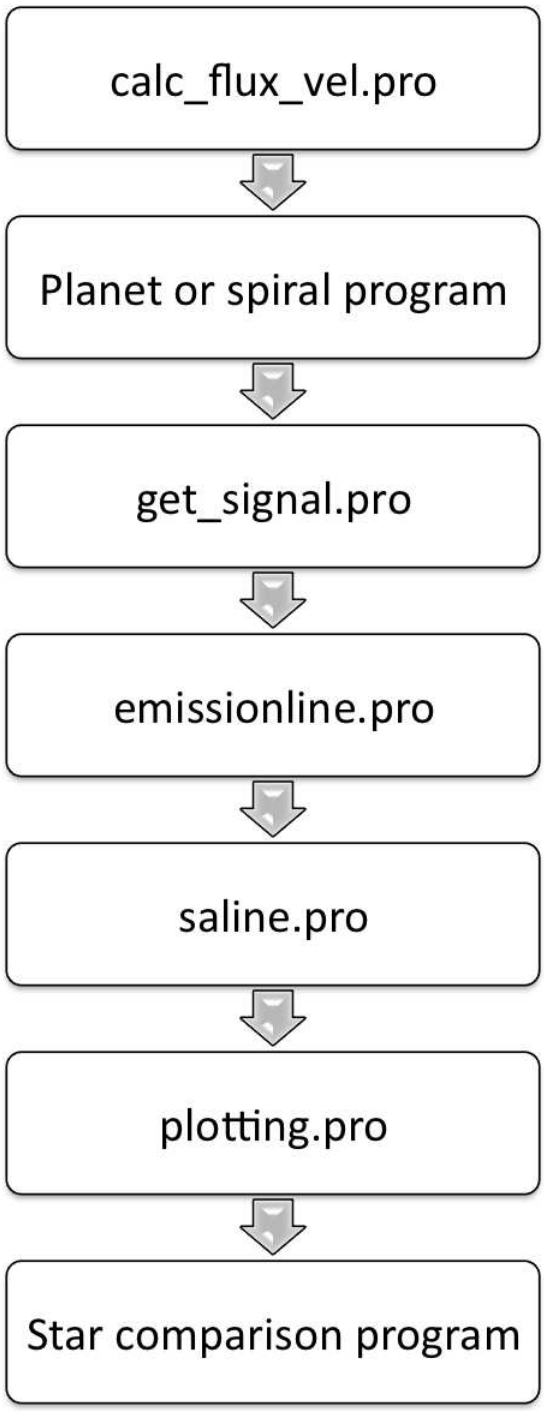

Figure A.2 A chart graphically describing the programs involved with spec_astro.pro.

  - Array of azimuthal points
  - Array of disk flux as a function of radius
  - Inclination of the disk
  - Position angle of disk with respect to the slit orientation
  - Stellar Mass
- Output:
  - fv_matrix
- Description:
  This program takes in the disk parameters and creates a matrix of data, fv_matrix. The program loops through the disk, de-projecting onto the sky the x and y coordinates of every point. It also determines the projected, line-of-sight velocity for that point. These data are then collected into a matrix, fv_matrix, which is then carried through the later programs in this code. Having a large matrix is advantageous because it can be added to later without affecting this part of the code. For example, if one wanted to add a planet or asymmetry, all one would need is to add a new code that would take in the fv_matrix, and output a larger matrix, with fv_matrix as a basis.

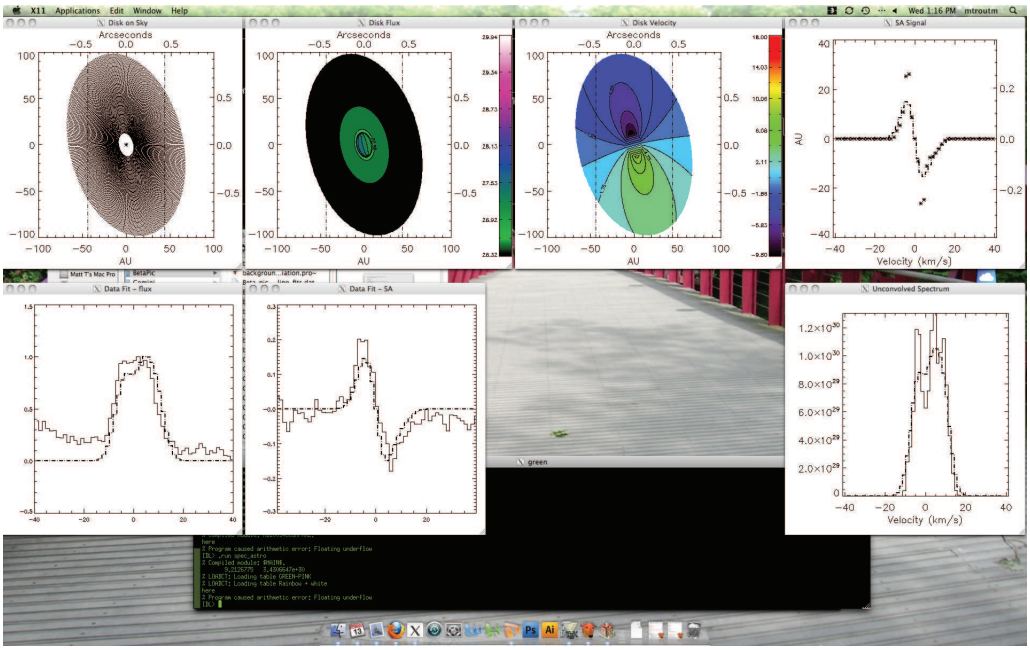

Figure A.3 Screenshot of the output when running spec_astro.pro.

Optional planet or spiral addition

- Input:
  - Planet or spiral parameters
- Output:
  - fv_matrix
- Description:
  This program can either add a planet or spiral arm. Since the fv_matrix is not ordered, any addition can be done afterward by the user, before the signals are determined in later programs.

get_signal.pro

- Input:
  - flux_vel
  - slitsize
  - spec_res
- Output:
  - signal
- Description:
  This program takes in the flux_vel matrix which contains the x position, y position, flux and velocity for every point in the model disk. It sums through the velocity bins to reproduce an unconvolved line flux spectrum. It also finds the center-of-light for every velocity bin to produce an unconvolved spectro-astrometric signal. The output is a matrix with velocity bin, flux, and spectro-astrometric signal.

emissionline.pro

- Input:
  - flux_vel
  - signal
- Output:
  - conv_spec
- Description:
  This program convolves the line flux signal obtained from the model with an instrument function of the users choosing. This produces a line flux as seen in an actual observation.

saline.pro

- Input:
  - flux_vel
  - signal
- Output:
  - conv_spec
- Description:
  This program convolves the spectro-astrometric signal obtained from the model with an instrument function of the users choosing. This produces a signal as seen in an actual observation.

plotting.pro

- Input:
  - flux_vel
  - conv_spec
- Output:
  - Plots of the disk model and resulting spectro-astrometric signal.
- Description:
  This program plots all of the data as acquired thus far. An example screenshot is shown in Figure A.3.

BIBLIOGRAPHY

Acke, B., & van den Ancker, M. E. 2006, A&A, 449, 267

Acke, B., & van den Ancker, M. E. 2006, A&A, 457, 171

Acke, B., van den Ancker, M. E., & Dullemond, C. P. 2005, A&A, 436, 209

Acke, B., & van den Ancker, M. E. 2004, A&A, 426, 151

Ardila, D. R., Golimowski, D. A., Krist, J. E., Clampin, M., Ford, H. C., & Illingworth, G. D. 2007, Astrophys. J., 665, 512

Armitage, P. J. 2007, Astrophys. J., 665, 1381

Armitage, P. J. 2003, Astrophys. J. Lett., 582, L47

Artymowicz, P., Burrows, C., & Paresce, F. 1989, Astrophys. J., 337, 494

Ayliffe, B. A., & Bate, M. R. 2009, MNRAS, 397, 657

Ayliffe, B. A., & Bate, M. R. 2009, MNRAS, 393, 49

Baines, D., et al. 2004, MNRAS, 353, 697

Barrado y Navascués, D., Stauffer, J. R., Song, I., & Caillault, J.-P. 1999, Astrophys. J. Lett., 520, L123

Bary, J. S., Weintraub, D. A., & Kastner, J. H. 2003, Astrophys. J., 586, 1136

Bertout, C., Robichon, N., & Arenou, F. 1999, A&A, 352, 574

Bitner, M. A., et al. 2008, Astrophys. J., 688, 1326

Bitner, M. A., Richter, M. J., Lacy, J. H., Greathouse, T. K., Jaffe, D. T., & Blake, G. A. 2007, Astrophys. J. Lett., 661, L69

Blake, G. A., & Boogert, A. C. A. 2004, Astrophys. J. Lett., 606, L73

Blondel, P. F. C., & Djie, H. R. E. T. A. 2006, A&A, 456, 1045

Boccaletti, A., Augereau, J.-C., Baudoz, P., Pantin, E., & Lagrange, A.-M. 2009, A&A, 495, 523

Boss, A. P. 1997, Science, 276, 1836

Bouwman, J., de Koter, A., Dominik, C., & Waters, L. B. F. M. 2003, A&A, 401, 577

Brandeker, A., Liseau, R., Olofsson, G., & Fridlund, M. 2004, A&A, 413, 681

Brittain, S. D., Najita, J. R., & Carr, J. S. 2009, Astrophys. J., 702, 85

Brittain, S. D., Simon, T., Najita, J. R., & Rettig, T. W. 2007, Astrophys. J., 659, 685

Brittain, S., Rettig, T. W., Simon, T., Balsara, D. S., Tilley, D., Gibb, E., & Hinkle, K. H. 2007, Astrophys. J. Lett., 670, L29

Brittain, S. D., Rettig, T. W., Simon, T., Kulesa, C., DiSanti, M. A., & Dello Russo, N. 2003, Astrophys. J., 588, 535

Brooke, T. Y., Tokunaga, A. T., & Strom, S. E. 1993, Astronomical J., 106, 656

Calvet, N., Muzerolle, J., Briceño, C., Hernández, J., Hartmann, L., Saucedo, J. L., & Gordon, K. D. 2004, Astronomical J., 128, 1294

Cameron, A. C., et al. 2010, MNRAS, 882

Carilli, C. L., & Rawlings, S. 2004, New Astronomy Review, 48, 979

Carmona, A., et al. 2008, A&A, 477, 839

Chin, G., & Weaver, H. A. 1984, Astrophys. J., 285, 858

Chen, C. H., et al. 2007, Astrophys. J., 666, 466

Chen, X. P., Henning, T., van Boekel, R., & Grady, C. A. 2006, A&A, 445, 331

Cieza, L., et al. 2007, Astrophys. J., 667, 308

Clarke, C. J., Gendrin, A., & Sotomayor, M. 2001, MNRAS, 328, 485

Corradi, W. J. B., Franco, G. A. P., & Knude, J. 1997, A&A, 326, 1215

Crifo, F., Vidal-Madjar, A., Lallement, R., Ferlet, R., & Gerbaldi, M. 1997, A&A, 320, L29

Currie, T., Kenyon, S. J., Balog, Z., Rieke, G., Bragg, A., & Bromley, B. 2008, Astrophys. J., 672, 558

D'Hendecourt, L. B., Allamandola, L. J., & Greenberg, J. M. 1985, A&A, 152, 130

De Sanctis, M. C., Capria, M. T., & Coradini, A. 2001, Astronomical J., 121, 2792

de Zeeuw, P. T., Hoogerwerf, R., de Bruijne, J. H. J., Brown, A. G. A., & Blaauw, A. 1999, Astronomical J., 117, 354

Dent, W. R. F., Greaves, J. S., & Coulson, I. M. 2005, MNRAS, 359, 663

Dewdney, P. E., Hall, P. J., Schilizzi, R. T., & Lazio, T. J. L. W. 2009, IEEE Proceedings, 97, 1482

Disanti, M. A., & Mumma, M. J. 2008, Space Science Reviews, 138, 127

Dominik, C., Dullemond, C. P., Waters, L. B. F. M., & Walch, S. 2003, A&A, 398, 607

Donehew, B., Brittain, S., 2010, *in prep.*

Doucet, C., Habart, E., Pantin, E., Dullemond, C., Lagage, P. O., Pinte, C., Duchêne, G., & Ménard, F. 2007, A&A, 470, 625

Dougherty, S. M., Taylor, A. R., & Clark, T. A. 1991, Astronomical J., 102, 1753

Dullemond, C. P., & Dominik, C. 2005, A&A, 434, 971w

Dullemond, C. P., Dominik, C., & Natta, A. 2001, Astrophys. J., 560, 957

Dunkin, S. K., Barlow, M. J., & Ryan, S. G. 1997, MNRAS, 286, 604

Fajardo-Acosta, S. B., Telesco, C. M., & Knacke, R. F. 1998, Astronomical J., 115, 2101

Ferlet, R., Vidal-Madjar, A., & Hobbs, L. M. 1987, A&A, 185, 267

Fernández, R., Brandeker, A., & Wu, Y. 2006, Astrophys. J., 643, 509

Finkenzeller, U., & Mundt, R. 1984, A&AS, 55, 109

Flower, D. R., & Launay, J. M. 1985, MNRAS, 214, 271

Freudling, W., Lagrange, A.-M., Vidal-Madjar, A., Ferlet, R., & Forveille, T. 1995, A&A, 301, 231

Furlan, E., et al. 2007, Astrophys. J., 664, 1176

Garcia Lopez, R., Natta, A., Testi, L., & Habart, E. 2006, A&A, 459, 837

Geers, V. C., van Dishoeck, E. F., Visser, R., Pontoppidan, K. M., Augereau, J.-C., Habart, E., & Lagrange, A. M. 2007, A&A, 476, 279

Geers, V. C., et al. 2006, A&A, 459, 545

Gibb, E. L., Brittain, S. D., Rettig, T. W., Troutman, M., Simon, T., & Kulesa, C. 2010, Astrophys. J., 715, 757

Glass, I. S., & Penston, M. V. 1974, MNRAS, 167, 237

Glassgold, A. E., Najita, J., & Igea, J. 2004, Astrophys. J., 615, 972

Golimowski, D. A., et al. 2006, Astronomical J., 131, 3109

Golimowski, D. A., Durrance, S. T., & Clampin, M. 1993, Astrophys. J. Lett., 411, L41

Goto, M., et al. 2007, Astrophys. J., 662, 389

Grady, C. A., et al. 2009, Astrophys. J., 699, 1822

Grady, C. A., et al. 2007, Astrophys. J., 665, 1391

Grady, C. A, Woodgate, B., Heap, S. R., Bowers, C., Nuth, J. A., Herczeg, G. J., Hill, H. G. M., 2005, Astrophys. J., 620, 470

Grady, C. A., et al. 2005, Astrophys. J., 630, 958

Grady, C. A., et al. 2001, Astronomical J., 122, 3396

Green, S. 1993, Astrophys. J., 412, 436

Green, S., & Thaddeus, P. 1976, Astrophys. J., 205, 766

Gullbring, E., Calvet, N., Muzerolle, J., & Hartmann, L. 2000, Astrophys. J., 544, 927

Habart, E., Testi, L., Natta, A., & Vanzi, L. 2003, A&A, 400, 575

Haisch, K. E., Jr., Lada, E. A., & Lada, C. J. 2001, Astronomical J., 121, 2065

Hamann, F. 1994, Astrophys. J. Suppl., 93, 485

Hartmann, L., Calvet, N., Gullbring, E., & D'Alessio, P. 1998, Astrophys. J., 495, 385

Hartmann, L., Kenyon, S. J., & Calvet, N. 1993, Astrophys. J., 407, 219

Heap, S. R., Lindler, D. J., Lanz, T. M., Cornett, R. H., Hubeny, I., Maran, S. P., & Woodgate, B. 2000, Astrophys. J., 539, 435

Herbig, G. H., & Bell, K. R. 1988, Lick Observatory Bulletin, Santa Cruz: Lick Observatory, —c1988

Herbig, G. H. 1960, Astrophys. J. Suppl., 4, 337

Herczeg, G. J., Linsky, J. L., Walter, F. M., Gahm, G. F., & Johns-Krull, C. M. 2006, Astrophys. J. Suppl., 165, 256

Hernández, J., et al. 2007, Astrophys. J., 662, 1067

Hernández, J., Calvet, N., Briceño, C., Hartmann, L., & Berlind, P. 2004, Astronomical J., 127, 1682

Hillenbrand, L. A., et al. 2008, Astrophys. J., 677, 630

Hillenbrand, L. A., Strom, S. E., Vrba, F. J., & Keene, J. 1992, Astrophys. J., 397, 613

Hinkle, K. H., et al. 2003, Proc. SPIE, 4834, 353

Hinkle, K. H., Joyce, R. R., Sharp, N., & Valenti, J. A. 2000, Proc. SPIE, 4008, 720

Hinkle, K. H., Cuberly, R. W., Gaughan, N. A., Heynssens, J. B., Joyce, R. R., Ridgway, S. T., Schmitt, P., & Simmons, J. E. 1998, Proc. SPIE, 3354, 810

Holland, W. S., et al. 1998, Nature, 392, 788

Hughes, A. M., Wilner, D. J., Qi, C., & Hogerheijde, M. R. 2008, Astrophys. J., 678, 1119

Ingleby, L., et al. 2009, Astrophys. J. Lett., 703, L137

Ireland, M. J., & Kraus, A. L. 2008, Astrophys. J. Lett., 678, L59

Jolly, A., et al. 1998, A&A, 329, 1028

Kalas, P., Graham, J. R., Beckwith, S. V. W., Jewitt, D. C., & Lloyd, J. P. 2002, Astrophys. J., 567, 999

Kalas, P., & Jewitt, D. 1995, Astronomical J., 110, 794

Kamp, I., Freudling, W., & Chengalur, J. N. 2007, Astrophys. J., 660, 469

Kamp, I., Dullemond, C. P., Hogerheijde, M., & Enriquez, J. E. 2005, Astrochemistry: Recent Successes and Current Challenges, 231, 377

Kamp, I., & Dullemond, C. P. 2004, Astrophys. J., 615, 991

Kamp, I., van Zadelhoff, G.-J., van Dishoeck, E. F., & Stark, R. 2003, A&A, 397, 1129

Kamp, I., & Bertoldi, F. 2000, A&A, 353, 276

Keller, L. D., et al. 2008, Astrophys. J., 684, 411

Kilkenny, D., Whittet, D. C. B., Davies, J. K., Evans, A., Bode, M. F., Robson, E. I., & Banfield, R. M. 1985, South African Astronomical Observatory Circular, 9, 55

Kley, W., & Dirksen, G. 2006, A&A, 447, 396

Kraus, S., Preibisch, T., & Ohnaka, K. 2008, Astrophys. J., 676, 490

Krotkov, R., Wang, D., & Scoville, N. Z. 1980, Astrophys. J., 240, 940

Kunde, V. R., & Maguire, W. C. 1974, Journal of Quantitative Spectroscopy and Radiative Transfer, 14, 803

Kurucz, R. L. 1993, IAU Colloq. 138: Peculiar versus Normal Phenomena in A-type and Related Stars, 44, 87

Lagage, P.-O., et al. 2006, Science, 314, 621

Lagrange, A.-M., et al. 2009, A&A, 493, L21

Lahuis, F., van Dishoeck, E. F., Blake, G. A., Evans, N. J., II, Kessler-Silacci, J. E., & Pontoppidan, K. M. 2007, Astrophys. J., 665, 492

Lecavelier des Etangs, A., et al. 2001, Nature, 412, 706

Liseau, R., Brandeker, A., Fridlund, M., Olofsson, G., Takeuchi, T., & Artymowicz, P. 2003, A&A, 402, 183

Lissauer, J. J. 1993, ARA&A, 31, 129

Lubow, S. H., & D'Angelo, G. 2006, Astrophys. J., 641, 526

Lubow, S. H., Seibert, M., & Artymowicz, P. 1999, Astrophys. J., 526, 1001

Malfait, K., Bogaert, E., & Waelkens, C. 1998, A&A, 331, 211

Mamajek, E. E., Meyer, M. R., Hinz, P. M., Hoffmann, W. F., Cohen, M., & Hora, J. L. 2004, Astrophys. J., 612, 496

Mannings, V., & Sargent, A. I. 1997, Astrophys. J., 490, 792

Matsuo, T., Shibai, H., Ootsubo, T., & Tamura, M. 2007, Astrophys. J., 662, 1282

Mayer, L., Lufkin, G., Quinn, T., & Wadsley, J. 2007, Astrophys. J. Lett., 661, L77

McKee, C. F., & Ostriker, E. C. 2007, ARA&A, 45, 565

McLean, I. S., et al. 1998, Proc. SPIE, 3354, 566

Meeus, G., Waters, L. B. F. M., Bouwman, J., van den Ancker, M. E., Waelkens, C., & Malfait, K. 2001, A&A, 365, 476

Mendoza, E. E. 1967, Boletin de los Observatorios Tonantzintla y Tacubaya, 4, 149

Meyer, M. R., et al. 2008, Astrophys. J. Lett., 673, L181

Mizuno, H., Nakazawa, K., & Hayashi, C. 1978, Progress of Theoretical Physics, 60, 699

Moór, A., Ábrahám, P., Derekas, A., Kiss, C., Kiss, L. L., Apai, D., Grady, C., & Henning, T. 2006, Astrophys. J., 644, 525

Mora, A., et al. 2001, A&A, 378, 116

Mouillet, D., Lagrange, A.-M., Beuzit, J.-L., & Renaud, N. 1997, A&A, 324, 1083

Mouillet, D., Larwood, J. D., Papaloizou, J. C. B., & Lagrange, A. M. 1997, MNRAS, 292, 896

Muzerolle, J., D'Alessio, P., Calvet, N., & Hartmann, L. 2004, Astrophys. J., 617, 406

Muzerolle, J., Calvet, N., & Hartmann, L. 2001, Astrophys. J., 550, 944

Muzerolle, J., Calvet, N., & Hartmann, L. 1998, Astrophys. J., 492, 743

Muzerolle, J., Hartmann, L., & Calvet, N. 1998, Astronomical J., 116, 2965

Najita, J. R., Strom, S. E., & Muzerolle, J. 2007, MNRAS, 378, 369

Najita, J. 2004, Star Formation in the Interstellar Medium: In Honor of David Hollenbach, 323, 271

Najita, J., Carr, J. S., & Mathieu, R. D. 2003, Astrophys. J., 589, 931

Najita, J. R., Edwards, S., Basri, G., & Carr, J. 2000, Protostars and Planets IV, 457

Öberg, K. I., Linnartz, H., Visser, R., & van Dishoeck, E. F. 2009, Astrophys. J., 693, 1209

Öberg, K. I., van Dishoeck, E. F., & Linnartz, H. 2009, A&A, 496, 281

Okamoto, Y. K., et al. 2004, Nature, 431, 660

Olofsson, G., Liseau, R., & Brandeker, A. 2001, Astrophys. J. Lett., 563, L77

Pantin, E., Lagage, P. O., & Artymowicz, P. 1997, A&A, 327, 1123

Perri, F., & Cameron, A. G. W. 1974, Icarus, 22, 416

Pérez, M. R., van den Ancker, M. E., de Winter, D., & Bopp, B. W. 2004, A&A, 416, 647

Perrin, M. D., Duchêne, G., Kalas, P., & Graham, J. R. 2006, Astrophys. J., 645, 1272

Perryman, M. A. C., et al. 1997, A&A, 323, L49

Pontoppidan, K. M., Blake, G. A., van Dishoeck, E. F., Smette, A., Ireland, M. J., & Brown, J. 2008, Astrophys. J., 684, 1323

Przygodda, F., van Boekel, R., Àbrahàm, P., Melnikov, S. Y., Waters, L. B. F. M., & Leinert, C. 2003, A&A, 412, L43

Rieke, G. H., et al. 2005, Astrophys. J., 620, 1010

Rettig, T., Brittain, S., Simon, T., Gibb, E., Balsara, D. S., Tilley, D. A., & Kulesa, C. 2006, Astrophys. J., 646, 342

Rettig, T. W., Haywood, J., Simon, T., Brittain, S. D., & Gibb, E. 2004, Astrophys. J. Lett., 616, L163

Roberge, A., & Weinberger, A. J. 2008, Astrophys. J., 676, 509

Roberge, A., Feldman, P. D., Weinberger, A. J., Deleuil, M., & Bouret, J.-C. 2006, Nature, 441, 724

Roberge, A., Feldman, P. D., Lagrange, A. M., Vidal-Madjar, A., Ferlet, R., Jolly, A., Lemaire, J. L., & Rostas, F. 2000, Astrophys. J., 538, 904

Rothman, L. S., et al. 2003, Journal of Quantitative Spectroscopy and Radiative Transfer, 82, 5

Rothman, L. S., et al. 1998, Journal of Quantitative Spectroscopy and Radiative Transfer, 60, 665

Salyk, C., Blake, G. A., Boogert, A. C. A., & Brown, J. M. 2009, Astrophys. J., 699, 330

Salyk, C., Pontoppidan, K. M., Blake, G. A., Lahuis, F., van Dishoeck, E. F., & Evans, N. J., II 2008, Astrophys. J. Lett., 676, L49

Saumon, D., Chabrier, G., & van Horn, H. M. 1995, Astrophys. J. Suppl., 99, 713

Sellgren, K., Luan, L., & Werner, M. W. 1990, Astrophys. J., 359, 384

Sicilia-Aguilar, A., Hartmann, L. W., Hernández, J., Briceño, C., & Calvet, N. 2005, Astronomical J., 130, 188

Skrutskie, M. F., Dutkevitch, D., Strom, S. E., Edwards, S., Strom, K. M., & Shure, M. A. 1990, Astronomical J., 99, 1187

Sloan, G. C., et al. 2005, Astrophys. J., 632, 956

Smith, B. A., & Terrile, R. J. 1984, Science, 226, 1421

Song, I., Caillault, J.-P., Barrado y Navascués, D., & Stauffer, J. R. 2001, Astrophys. J., 546, 352

Stauffer, J. R., Hartmann, L. W., & Barrado y Navascues, D. 1995, Astrophys. J., 454, 910

Strom, K. M., et al. 1990, Astrophys. J., 362, 168

Strom, K. M., Strom, S. E., Edwards, S., Cabrit, S., & Skrutskie, M. F. 1989, Astronomical J., 97, 1451

Strom, K. M., Strom, S. E., Breger, M., Brooke, A. L., Yost, J., Grasdalen, G., & Carrasco, L. 1972, Astrophys. J. Lett., 173, L65

Su, K. Y. L., et al. 2006, Astrophys. J., 653, 675

Sylvester, R. J., Skinner, C. J., Barlow, M. J., & Mannings, V. 1996, MNRAS, 279, 915

Thébault, P., & Augereau, J.-C. 2005, A&A, 437, 141

Tjin A Djie, H. R. E., Remijn, L., & The, P. S. 1984, A&A, 134, 273

Todorov, K., Luhman, K. L., & McLeod, K. K. 2010, Astrophys. J. Lett., 714, L84

Tokunaga, A. T., Toomey, D. W., Carr, J., Hall, D. N. B., & Epps, H. W. 1990, Proc. SPIE, 1235, 131

Troutman, M., Hinkle, K., Najita, J., Rettig, T., Brittain, S., 2010, in prep.

Troutman, M., Najita, J., Carr, J., Brittain, S., 2010, in prep.

Troutman, M., Najita, J., Donehew, B., Liskowski, J., Brittain, S., 2010, in prep.

van Boekel, R., Min, M., Waters, L. B. F. M., de Koter, A., Dominik, C., van den Ancker, M. E., & Bouwman, J. 2005, A&A, 437, 189

van Dishoeck, E. F. 2004, ARA&A, 42, 119

van Dishoeck, E. F., Black, J. H. 1986, Astrophys. J., 62, 109

van den Ancker, M. 1999, Ph.D. Thesis,

van den Ancker, M. E., de Winter, D., & Tjin A Djie, H. R. E. 1998, A&A, 330, 145

van den Ancker, M. E., et al. 1997, A&A, 324, L33

van der Plas, G., van den Ancker, M. E., Acke, B., Carmona, A., Dominik, C., Fedele, D., & Waters, L. B. F. M. 2009, A&A, 500, 1137

Vidal-Madjar, A., et al. 1994, A&A, 290, 245

Vieira, S. L. A., Corradi, W. J. B., Alencar, S. H. P., Mendes, L. T. S., Torres, C. A. O., Quast, G. R., Guimarães, M. M., & da Silva, L. 2003, Astronomical J., 126, 2971

Visser, R., Geers, V. C., Dullemond, C. P., Augereau, J.-C., Pontoppidan, K. M., & van Dishoeck, E. F. 2007, A&A, 466, 229

Vinković, D., Ivezić, Ž., Jurkić, T., & Elitzur, M. 2006, Astrophys. J., 636, 348

Wade, G. A., Bagnulo, S., Drouin, D., Landstreet, J. D., & Monin, D. 2007, MNRAS, 376, 1145

Wahhaj, Z., Koerner, D. W., & Sargent, A. I. 2007, Astrophys. J., 661, 368

Wahhaj, Z., Koerner, D. W., Backman, D. E., Werner, M. W., Serabyn, E., Ressler, M. E., & Lis, D. C. 2005, Astrophys. J., 618, 385

Wagner, R. M., Lutz, B. L., & Wyckoff, S. 1987, Astrophys. J., 322, 544

Walker, H. J., & Heinrichsen, I. 2000, Icarus, 143, 147

Walker, H. J., & Wolstencroft, R. D. 1988, PASP, 100, 1509

Wall, J. V., & Jenkins, C. R. 2003, Princeton Series in Astrophysics

Waters, L. B. F. M., & Waelkens, C. 1998, ARA&A, 36, 233

Warin, S., Benayoun, J. J., & Viala, Y. P. 1996, A&A, 308, 535

Whelan, E. T., Ray, T. P., & Davis, C. J. 2004, A&A, 417, 247

Whittet, D. C. B., Kirrane, T. M., Kilkenny, D., Oates, A. P., Watson, F. G., & King, D. J. 1987, MNRAS, 224, 497

Wilner, D. J., Holman, M. J., Kuchner, M. J., & Ho, P. T. P. 2002, Astrophys. J. Lett., 569, L115

Wisniewski, J. P., Bjorkman, K. S., Magalhães, A. M., Bjorkman, J. E., Meade, M. R., & Pereyra, A. 2007, Astrophys. J., 671, 2040

Wyatt, M. C. 2008, ARA&A, 46, 339

Wyatt, M. C., Smith, R., Su, K. Y. L., Rieke, G. H., Greaves, J. S., Beichman, C. A., & Bryden, G. 2007, Astrophys. J., 663, 365

Youdin, A. N., & Shu, F. H. 2002, Astrophys. J., 580, 494

Young, R. E. 2003, New Astronomy Review, 47,1

Zuckerman, B., & Song, I. 2004, ARA&A, 42, 685

Zuckerman, B., & Song, I. 2004, Astrophys. J., 603, 738

Zuckerman, B., Song, I., Bessell, M. S., & Webb, R. A. 2001, Astrophys. J. Lett., 562, L87

Zuckerman, B. 2001, ARA&A, 39, 549